Toward Bridging the Pressure Gap Between Real World Catalysis and Ideal Surface Science Conditions Using Ambient Pressure Photoelectron Spectroscopy and Molecular Beam Instrument

Thesis Submitted to
Academy of Scientific and Innovative Research
For the Award of the Degree of
Doctor of Philosophy in Chemical Sciences

by
Kanak Roy
Registration Number 10CC11J26047
Under the Guidance of
Dr. Chinnakonda S. Gopinath

Catalysis Division
CSIR- National Chemical Laboratory
Pune, India

Toward Bridging the Pressure Gap Between Real World Catalysis and Ideal Surface Science Conditions Using Ambient Pressure Photoelectron Spectroscopy and Molecular Beam Instrument

Thesis Submitted to
Academy of Scientific and Innovative Research
For the Award of the Degree of
Doctor of Philosophy in Chemical Sciences

by
Kanak Roy
Registration Number 10CC11J26047
Under the Guidance of
Dr. Chinnakonda S. Gopinath

Catalysis Division
CSIR- National Chemical Laboratory
Pune, India

CERTIFICATE

This is to certify that the work incorporated in this thesis entitled, "Toward Bridging the Pressure Gap between Real World Catalysis and Ideal Surface Science Conditions using Ambient Pressure Photoelectron Spectroscopy and Molecular Beam Instrument" submitted by Mr. Kanak Roy, for the degree of Doctor of Philosophy to Academy of Scientific and Innovative Research (AcSIR), was carried out by the candidate under my supervision in the Catalysis Division, CSIR - National Chemical Laboratory, Pune, India. Such document has not been submitted elsewhere for a degree. Any material that has been obtained from other sources has been duly acknowledged in the thesis.

Dr. Chinnakonda S. Gopinath
(Thesis Supervisor)
Senior Principal Scientist
Catalysis Division & Center of Excellence on Surface Science
CSIR - National Chemical Laboratory
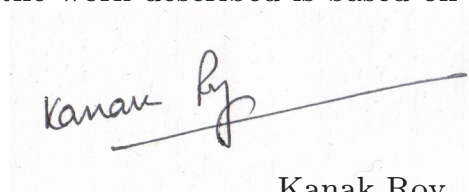Dr. Homi Bhabha Road, Pune 411 008, India

Kanak Roy

Catalysis Division
CSIR- National Chemical Laboratory
Pune 411 008
Email: kanak.chem@gmail.com

DECLARATION

I, Mr. Kanak Roy, hereby declare that the work incorporated in the thesis entitled "Toward Bridging the Pressure Gap between Real World Catalysis and Ideal Surface Science Conditions using Ambient Pressure Photoelectron Spectroscopy and Molecular Beam Instrument" submitted by me to Academy of Scientific and Innovative Research (AcSIR) for the degree of Doctor of Philosophy, is the result of investigations carried out by me in Catalysis Division, CSIR - National Chemical Laboratory, Pune under the supervision of Dr. Chinnakonda S. Gopinath and has not been submitted to this or any other Institution for the award of any other Degree or Diploma.

In keeping with the general practice of reporting scientific observations due acknowledgements have been made wherever the work described is based on the findings of other investigators.

Pune   Kanak Roy

To my Parents

Acknowledgements

Kanak Roy

Contents

List of Abbreviations

APPES	Ambient Pressure Photoelectron Spectroscopy
XPS	X-ray Photoelectron Spectroscopy
UHV	Ultra High Vacuum
EEA	Electron Energy Analyzer
ELR	Electrostatic Lens Regime
UVPES	Ultra violet Photoelectron Spectroscopy
FWHM	Full width at half maximum
QMS	Quadrupole Mass Spectrometer
OD	Outer Diameter
MBI	Molecular Beam Instrument
PES	Photoelectron Spectroscopy
KE	Kinetic Energy
BE	Binding Energy
RT	Room Temperature
NAP	Near Ambient Pressure
VB	Valence Band
TWC	Three way Catalytic Converter
SCR	Selective Catalytic Reduction
RDS	Rate determining step
SS	Steady state
TS	Transient state
TPD	Temperature Programmed Desorption

List of Symbols

K_n	Knudsen Number
s	Sticking Coefficient
k_B	Boltzman Constant
R_{max}	Reaction rate maximum
λ_{gas}	Mean free path of gas molecule
λ_e	Mean free path of electron
Θ_O	Surface oxygen coverage
$\Theta_{O\text{-}sub}$	Subsurface oxygen coverage
R_{NO}	Rate of NO adsorption
R_{O_2}	Rate of O_2 adsorption
R_{H_2O}	Rate of H_2O formation
R_{NH_3}	Rate of NH_3 formation
R_{N_2O}	Rate of N_2O formation
F	Gas Flux

List of Figures

pressure.

chemisorption and dissociation (orange solid circle) is hindered or at least minimized, which enhances NO dissociation and deNO$_x$ activity around ambient temperatures.

at 350 K on (g) SM-Pd, and on (h) clean Pd(111). (j) UVPES recorded at UHV and 350 K after the reaction shown in g and evacuation. In situ C 1s core level spectra is shown as inset; Gas phase CO_2 observed along with two CO_{ads} species.

Preface

Photoelectron spectroscopy (PES) is one of the best available surface science techniques for investigating surface electronic nature of materials. This technique is conventionally, an ultra-high vacuum technique, as photoelectrons cannot make it possible to reach the detector due to collision with the gas molecules or inelastic scattering. In fact, most of the surface science techniques operate under ultra-high vacuum. The practical catalytic reactions, which generally occur at ambient pressure conditions, therefore, cannot be investigated under in situ conditions or close to that using conventional PES. However, photoelectron spectroscopy has been tried to be used at elevated pressures. Recent development in this field is Ambient Pressure Photoelectron Spectroscopy (APPES), which can operate at near ambient pressure (up to few mbar). By using sophisticated electron energy analyzers and differentially pumped electron lenses, photoelectrons are detected. Thus APPES can bridge the "pressure gap" between real world practical catalysis and ideal/ conventional surface science studies. This thesis mainly focuses on different studies to bridge the pressure gap between the atmospheric real world conditions where the actual catalysis happens and ideal surface science conditions in which the catalytic characterizations are made. More studies about the elementary kinetics have been performed by using Molecular beam Instrument (MBI).

In chapter 1, a brief introduction about the role of surface science in understanding heterogeneous catalysis and basic working principles of the two important surface science tools, namely MBI and APPES have been given. Heterogeneous catalysis is a complex phenomenon as because a straightforward relation between structure and activity of a catalyst cannot be established. Many parameters play a significant role towards the reaction, which are apparently not possible to understand without operando studies. Therefore, many surface science techniques which are conventionally operational under UHV have been developed to operate under working conditions or near to that. APPES is one such state-of-the-art technique.

Development and design aspects of a laboratory based APPES has been described in Chapter 2. The spectrometer can successfully perform XPS up to 1 mbar with a 0.8 mm diameter aperture analyzer cone. A systematic in situ transformation of coinage metal foils (Au, Ag, and Cu) with oxygen up to 1 mbar pressure and 773

K has been shown to demonstrate the performance of the spectrometer.

In XPS, the changes in the core levels are investigated thoroughly. Valence band photoemission is again more surface sensitive than XPS, and explores more information regarding the bonding and hybridization on the surfaces. UVPES (Ultra-violet Photoemission Spectroscopy) is, therefore, also worth exploring. Nonetheless, UVPES at near ambient pressure conditions is more challenging than Ambient Pressure-XPS. The KE of ejected photoelectrons in UVPES is much lower than the KE of photoelectrons in XPS. We have achieved UVPES up to 0.3 mbar pressure. A mapping of changes in valence band during systematic oxidation of copper has been shown in Chapter 3. Chapter 2 and 3 thus, together, deal with the photoemission in core level and valence level at near ambient pressures up to 1 mbar and 0.3 mbar, respectively.

Chapter 4 shows the selective catalytic reduction (SCR) of NO with H_2 in presence of excess oxygen on Pd(111). SCR is a very popular and effective method of NO_x abatement, or De-NOx. H_2-SCR has been conceptualized to make a greener and technologically viable method of De-NO_x. Pd-based catalysts are found to be very promising for NO reduction under oxidizing environments as well as they are good for CO oxidation reactions also. This is the reason why Pd-based catalysts are popular for three-way catalytic converters in cars. MBI studies give details of kinetic aspects about the NO + H_2 + O_2 reaction on Pd(111). We have shown that Palladium surfaces that are modified with O atoms in the subsurface broaden the NO reduction temperature regime up to 325 K with O_2-rich NO +H_2 +O_2 compositions. Compared to virgin Pd surfaces, up to 150 % higher deNO$_x$ catalytic activity was observed with modified Pd surfaces at the reaction maximum.

Low temperature CO oxidation reaction on Pd(111) modified with O in the subsuraface has been shown in Chapter 5. The role of subsurface O in shifting the temperature of CO oxidation reaction on palladium has been observed. UV valence band spectral analysis of surface modification due to presence of O atoms in the subsurface and $CO+O_2$ reaction on modified Pd(111) surfaces under near ambient pressure conditions demonstrates the changes in electronic structure of surfaces with a change in surface potential and directly probes the CO_2 formation under reaction conditions. Chapter 4 and Chapter 5 give a clear indication that surface electronic nature modification by populating O atoms in the subsurface of palladium is one of the handle to tune catalytic activity of palladium. However,

more studies with many different techniques are required to understand the complex phenomenon of surface modification and its influence in catalysis.

List of Publications

[1]. Kanak Roy, C. P. Vinod, Chinnakonda S. Gopinath, Design and Performance Aspects of a Custom-Built Ambient Pressure Photoelectron Spectrometer toward Bridging the Pressure Gap: Oxidation of Cu, Ag, and Au Surfaces at 1 mbar O_2 Pressure, *J. Phys. Chem. C* **2013**, 117 (9), 4717–4726.

[2]. Kanak Roy, Chinnakonda S. Gopinath, UV Photoelectron Spectroscopy at Near Ambient Pressures: Mapping Valence Band Electronic Structure Changes from Cu to CuO, *Anal. Chem.* **2014**, 86(8), 3683–3687. (Letter).

[3]. Kanak Roy, Chinnakonda S. Gopinath, NO_x Reduction at Near Ambient Temperatures and Under Lean-Burn Conditions on Modified Pd Surfaces, Kanak Roy and Chinnakonda S. Gopinath, *ChemCatChem.* **2014**, 6(2), 531-537.

[4]. Kanak Roy, Ruchi Jain, Chinnakonda S. Gopinath, Sustainable and Near Ambient $DeNO_x$ Under Lean Burn Conditions: A Revisit to NO Reduction on Virgin and Modified Pd(111) Surfaces, *ACS Catal.* **2014**, 4 (6), 1801–1811.

[5]. Chinnakonda S. Gopinath, Kanak Roy, Sankaranarayanan, Can We Shift and/or Broaden the Catalysis Regime towards Ambient Temperature?, *ChemCatChem.* **2015**, 7(4), 588 - 594.

[6]. Arulraj Arulkashmir, Bhanprakash Jain, Jino C. John, Kanak Roy, Kothandam Krishnamoorthy, Chemically doped perylene diimide lamellae based field effect transistor with low operating voltage and high charge carrier mobility, *Chem. Commun.* **2014**, 50, 326-328.

[7]. Kumarsrinivasan Sivaranjani, Sivaraman RajaAmbal, Tanmay Das, Kanak Roy, Somnath Bhattacharyya and Chinnakonda S. Gopinath, Disordered Mesoporous $TiO_{2-x}N_x$ + Nano-Au: An Electronically Integrated Nanocomposite for Solar H_2 Generation, *ChemCatChem.* **2014**, 6, (2), 522-530.

[8]. Sourav Bag, Kanak Roy, Chinnakonda S. Gopinath, C. Retna Raj, Facile Single-Step Synthesis of Nitrogen-Doped Reduced Graphene Oxide-Mn_3O_4

Hybrid Functional Material for the Electrocatalytic Reduction of Oxygen, *ACS Appl. Mater. Interfaces* **2014**, 6 (4), 2692–2699.

[9]. Mrinal Sarkar, Supriti Paul, Kanak Roy, Sandipan Roychaudhuri, Avijit Sarkar, Aloke Kumar Ghosh, Debashis Ray, Pseudohalide supported mononuclear trans Ni^{II} complexes of cationic and neutral dinitrogen heterocycles, *Inorg. Chimica Acta* **2010**, 363(12), 3041-3047 (from M.Sc. project work).

[10]. Kanak Roy, Ruchi Jain, Manojkumar Ghosalya, Chinnakonda S. Gopinath, Surface Chemistry of Cu and Si in Reactive Gas Atmosphere: Near Ambient Pressure UV Photoelectron Spectroscopy (manuscript under preparation).

[11]. Kanak Roy, Ruchi Jain, Manojkumar Ghosalya, Kasala P. Reddy, Chinnakonda S. Gopinath, Near Ambient Temperature Environmental Catalysis Aspects on Modified Pd-Surfaces, manuscript under preparation for *Comptes Rendus de Chimie* (invited).

[12]. Anjani Dubey, Sadhu Kolekar, Edwin Gnanakumar, Kanak Roy, C. P. Vinod, Chinnakonda S. Gopinath, An attempt to bridge the material gap between ideal surface science and real-world heterogeneous catalysis, manuscript submitted.

Chapter 1

A Brief Overview: Surface Science Approach, Molecular Beam Instrument, and Ambient Pressure Photoelectron Spectroscopy

§ 1.1 Surface Science Approach

The wide ranging arsenal of experimental surface science has transformed our ability to understand surface processes over the years. Surface science grew during 1950 - 1960s mainly with the growth of space science and technology and semiconductor microelectronics [1] and with the course of time it has become an interdisciplinary field. Heterogeneous catalysis also is a surface and interface phenomenon. The contribution of surface science in understanding the mechanism of crucial heterogeneous catalytic processes is tremendous. The 2007 Nobel Prize in Chemistry has been awarded to a surface chemist Gerhard Ertl for his studies of chemical processes on solid surfaces. However, if we see surface science from the beginning of its journey, surface science was more or less synonymous to vacuum science, as the surface science techniques were functioning in ultra-high vacuum conditions (p $\backsim 10^{-6}$ mbar range). But the catalysis in general, is real world atmospheric phenomena. The real in the sense, that catalysis happens in pressure ranging to the atmospheric pressure and within thermodynamic regime. A fundamental question, therefore, always is associated with the surface science studies of heterogeneous catalysis. The question is: what are the complexities in heterogeneous catalysis; those make it difficult to understand in microscopic level and how far surface science has been capable to handle those complexities?

Catalysis, in particular heterogeneous catalysis, plays a pivotal role to global production of chemicals. 80% of all man made materials at some point in their manufacture use a catalyst [2] and the majority of these are heterogeneously catalyzed reactions. The catalytic effect was initially observed by Sir Humphrey Davy and Gottlieb Kirchhoff by 1812. Davy observed that platinum induced the oxidation of alcohol vapor in air [3] and Kirchhoff was the first to observe the liquid phase catalysis of acid degradation of starch [4]. The experimental catalysis research started in that way. Over the years, catalysis research grew with focus holding on many aspects. These aspects are broadly classified as experimental and theoretical. The experimental aspects have many categories like preparation techniques, activity-selectivity testing and kinetic and mechanistic elucidation. The theoretical aspects are based on electronic and mechanical bulk property predictions based on electronic wave function or electron density function calculations.

There has been integration of these aspects to many extents to explain

catalytic reactions and cycles. However, the complexity or more precisely complicacy is the dilemma of catalysis research. The grand challenge in catalysis research is the *a priori* design of a catalyst for a reaction [5]. That is, take the chemicals, deposit them onto the support and then on substrate, and put the substrate into the reactor and achieve a predicted result. This unique challenge has opened wide the window of catalysis research. It paves us to delve deep into the microscopic level of catalysis. For example, in figure 1.1 we can find the morphological complexity of an industrial ammonia synthesis catalyst.

Technical conditions
T ~ 400 °C, p ~ 300 bar
promoted iron catalyst

BASF S6-10 catalyst (at %)

	Fe	K	Al	Ca	O
Bulk Composition	40.5	0.35	2.0	1.7	53.2
Surface-Unreduced	8.6	36.2	10.7	4.7	40.0
Reduced	11.0	27.0	17.0	4.0	41.0
cat. active spot	30.1	29.0	6.7	1.0	33.2
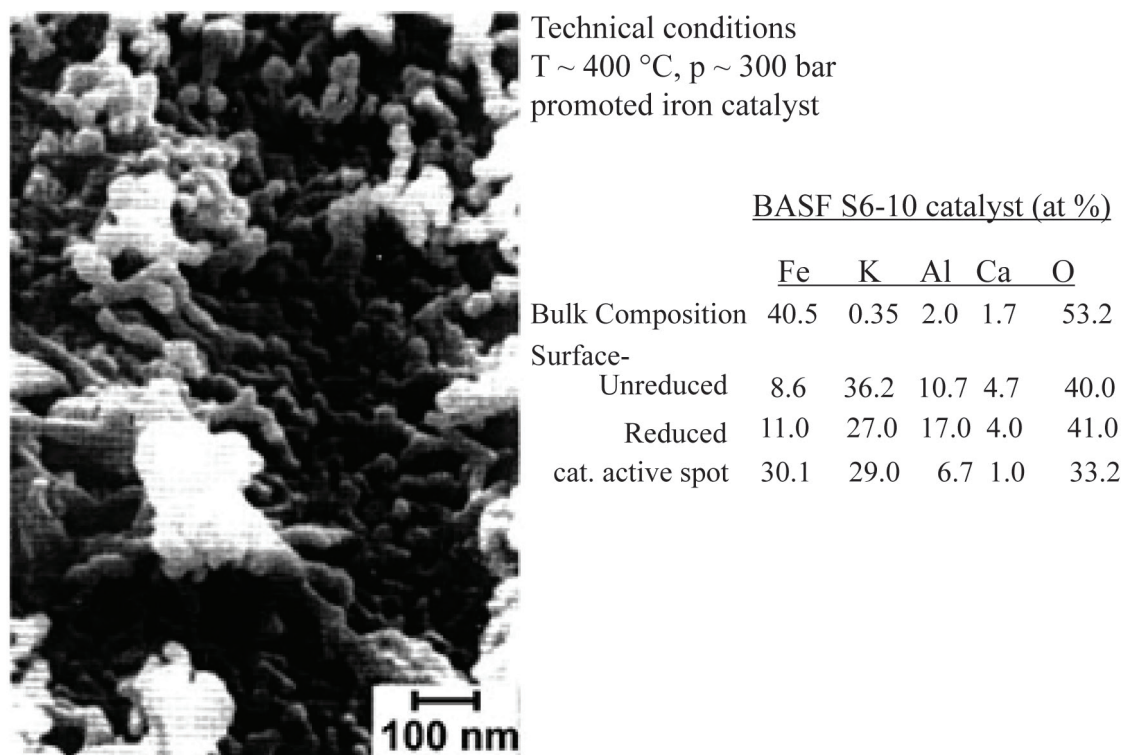
Figure 1.1 Surface topography and chemical composition of an industrial ammonia synthesis Mittasch catalyst Reproduced with permission from Ref [6].

Then how to handle the shear complicacy of catalysis world? There has been a historic approach to catalysis research to deal with the complexity of a practical reaction system by reducing to a level that can be adequately described. In the words of Langmuir [7]
"Most finely divided catalysts must have structures of great complexity. In order to simplify our theoretical consideration of reactions at surfaces, let us confine our attention to plane surfaces. If the principles in this case are well understood,

it should then be possible to extend the theory to the case of porous bodies. In general, we should look upon the surface consisting of a checkerboard".

This is the basic approach of surface science to attend the rather complex heterogeneous catalytic system. Since the 1960s surface science techniques have been used to study the surface chemistry of metal single crystals in relation to their properties as catalysts. This approach was very successful in explaining large number of heterogeneous catalytic systems, giving rise to the hope that someday entire processes may be understood. Extrapolations of experimental details from model investigations to the real world of an operating system were thought to be possible. Ammonia synthesis system is one of the best known examples of this strategy [8]. The years of research fructified a kinetic theory that enabled the precise prediction of the yield of ammonia under technical conditions using as parameters experimentally determined properties and a set of experimentally verified elementary reaction steps [9]. Unfortunately, many catalytic processes are still very less known from the molecular point of view. This is not because the failure of the strategy, rather the complicacy of the system.

The main hurdle in understanding structure-activity correlation is the complexity of the solid catalyst. Surface and bulk structure of active materials shows dynamic nature. This dynamics were recognized to be related to geometric structure, composition, and the local electronic state of the active center [8]. Thus analysis of catalytic activity should be associated with careful analysis of all the underlying components (active components, support, impurities, poisons, promotors) of a practical catalyst. The oversimplification in material structure by using definite single crystal surfaces in surface science is named as "material gap". To bridge the material gap between surface science and heterogeneous catalysis, model catalysts have been formulated. The idea is to simulate structures similar to the practical catalyst and yet capable of characterization by the surface science techniques. The material gap arises due to many aspects which have been summarized in the figure 1.2, and these aspects are not discussed in details here as it is beyond the context of this thesis.

The other important barrier between surface science and catalysis, which needs to be bridged, is the "pressure gap". Since only few surface science techniques can be applied under reaction conditions and even with modification in technical reaction conditions, surface science mostly goes with post-mortem analysis i.e. before the start of the reaction and after completion of the reaction it analyzes

the catalyst. As indicated by G. A. Somorjai, "it is like studying a life with access only to the prenatal and postmortem states" [11]. However, the dynamic restructuring which may play crucial role in actual catalytic process remains unexplored. Any species which evolve only during course of the reaction remains undetected. The maturity of surface science should be to bridge this pressure gap, to understand and explain practical catalytic processes. A realistic description of a surface science technique would be to investigate the catalyst under in situ conditions by following some physicochemical property as a function of relevant reaction conditions and simultaneous observation of the kinetic parameters. Only then is it ensured that the investigation or study is capable of exploring the active state of the catalyst and data is relevant for determining the reaction mechanism [12].
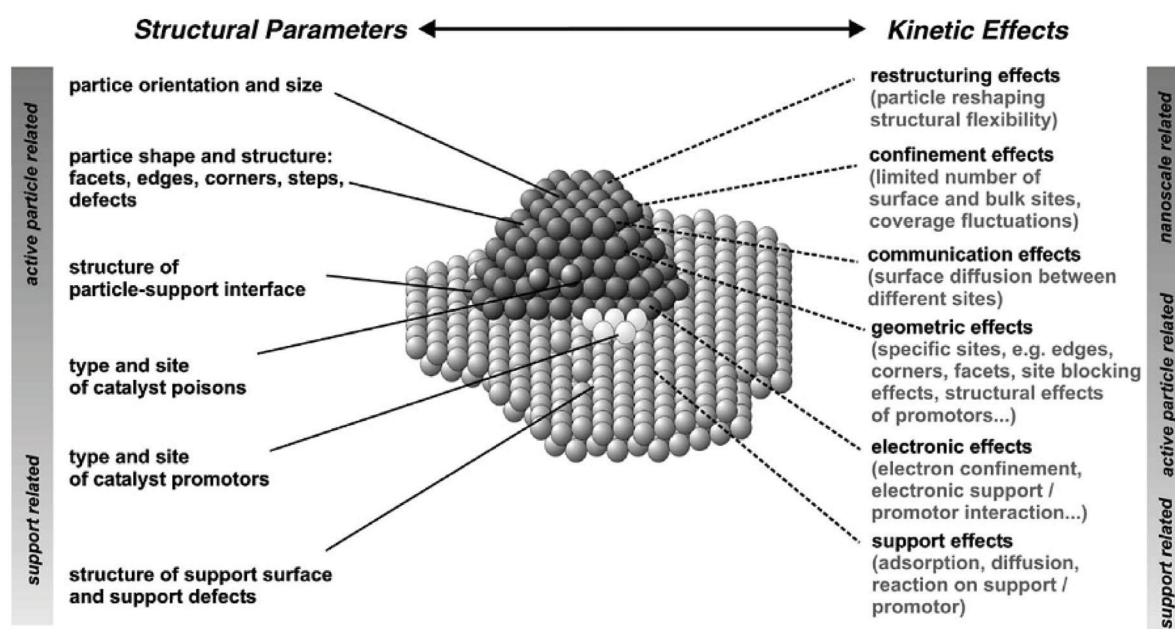
Figure 1.2 Structural parameters and kinetic effects on supported metal catalysts. Reproduced with permission from Ref [10].

Knowing the mechanism is crucial because it lays the foundation for catalyst optimization and development. As the mechanism is dependent on many sets of parameters whose quantitative correlation is unknown, extrapolation of surface science experiments to real operation conditions may lead to ambiguity. Quantitative understanding of these correlations therefore contributes lot to understand the complete process. Global activity and selectivity data do not allow firm conclusions regarding reaction mechanism; a broad speculation is always accompanied. The kinetics is determined by chemisorption processes (which is

actually only a part of the mechanism), and by the micro- and macro-texture of the catalyst. The limitations of mass and energy transport processes and consecutive non-catalytic reactions tend to obscure the correlation of mechanism and kinetics. A true microscopic understanding of the kinetics may require effects to be taken into account which are beyond the kinetic rate equation (KRE) approach typically used in microkinetic modeling [10].

Non *in situ* experiments deviates from four sets of parameters shown in Figure 1.3.
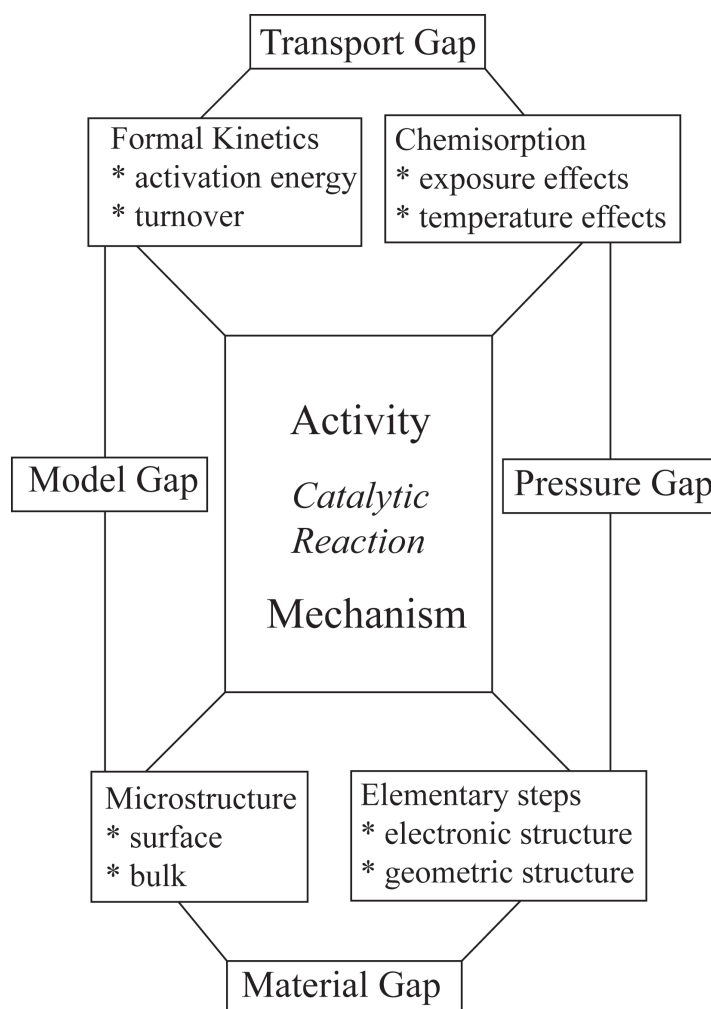
Figure 1.3 The gaps arisen due to oversimplification of different aspects of heterogeneous catalyst are illustrated. (Adapted from ref. 12).

These deviations are mainly reasons why surface science ceases to be accurately scrutinizing tool for practical industrial catalysis. One question obviously asked is whether we can use the kinetic data obtained in UHV condition

to describe the reaction occurring at ambient (atmospheric) pressures. The earlier studies [13-18] show that it is very different if we ignore the non-ideality of the reaction kinetics of the system. Incorporation of the non-ideal kinetic feature is also challenging because the adsorbate coverage which is obtained for UHV surface science studies does not corroborate with that of the ambient conditions.

Last four decades research has improved surface science toward bridging the two main gaps with real world catalysis: "material gap" by designing new model catalysts which can be ideally studied with the desired surface science techniques, and "pressure gap" by developing new surface techniques or design which can be applied in operando conditions. Figure 1.4 thus shows the evolution of surface science from UHV single crystal studies to contemporary nanoparticle research at near ambient pressure conditions.
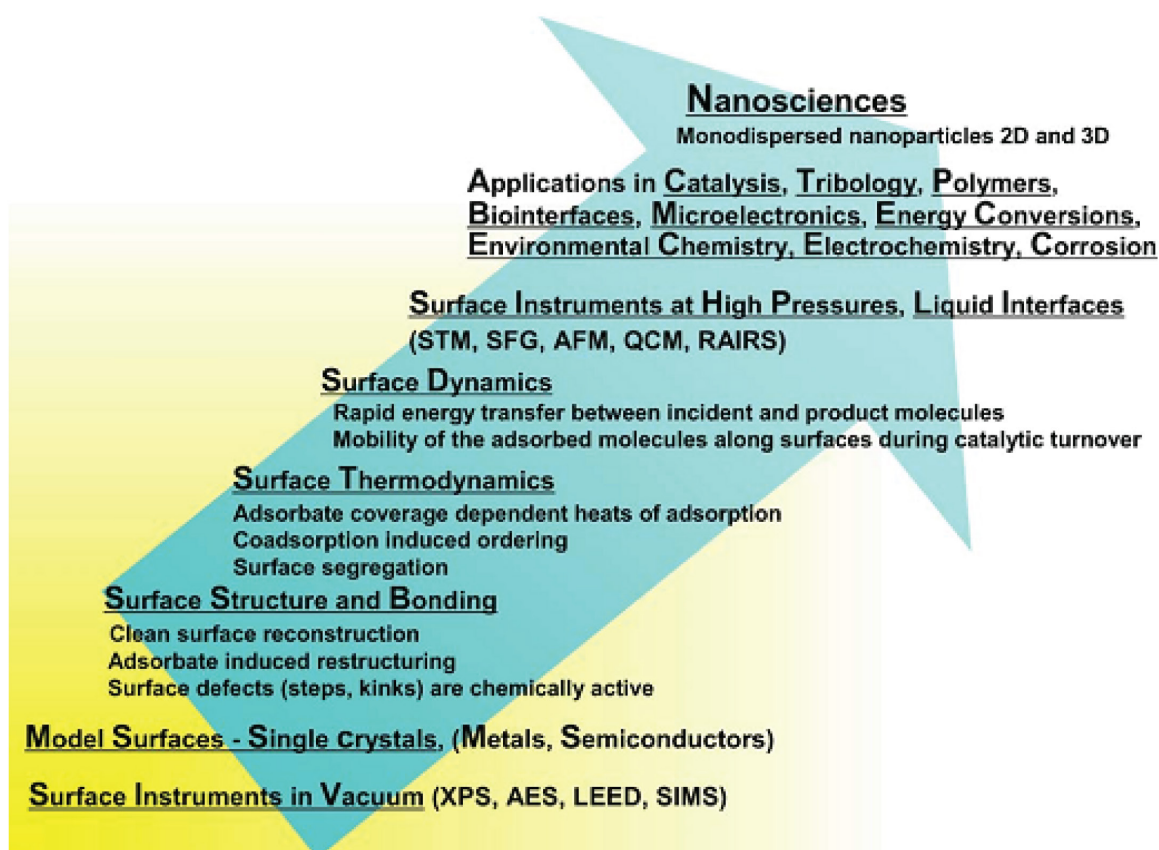
Figure 1.4 Evolution of surface science over the years. Reproduced with permission [19].

Surface science studies towards understanding the catalysis started with single crystal surfaces in vacuum. In vacuum, it is possible to detect the probes because of their high mean free paths, and thus one could able to detect the surface

composition with 1% monolayer sensitivity, electronic structure, oxidation state of surface atoms, structure of clean surfaces and adsorbate layer, bond distances and bond angles of adsorbed molecules [20]. Mostly single crystal surfaces were used as model catalysts and breakthrough findings were obtained in vacuum surface science [21-23]. With the advancement of the technological state-of-the-art techniques modern surface science evolved to be used under operating conditions or closer to that of the real world catalysis. In last few decades a number of surface-sensitive techniques have been developed which could be operated under elevated pressures, among them are infrared spectroscopy, sum-frequency generation (SFG), High pressure X-ray photoelectron spectroscopy, near edge X-ray absorption fine structure (NEXAFS), neutral-impact collision ion scattering spectroscopy (NICISS), meta-stable impact electron spectroscopy (MIES), scanning force microscopy, high pressure scanning tunneling microscopy (HP-STM) and scanning electron microscopy (environmental SEM). In the next sections two of the surface science techniques which are employed in the studies carried out here, are discussed in a brief manner: Molecular Beam Instrument which allows to bridge the pressure gap up to an intermediate level of 10^{-5} mbar with excellent information on elementary kinetics, and another being the HP-XPS or APPES (Ambient Pressure Photoelectron Spectroscopy) which can be operated up to mbar regime giving the electronic information of the surfaces. Both MBI and APPES allow to study gas-solid interaction at significantly high pressures enabling to understand the catalysis phenomenon to a better level.

§ 1.2 Molecular Beam Instrument

Molecular beam is a well-established technique, was introduced by Dunoyer in 1911 [24]. The application of molecular beam provides an excellent way of performing quantitative experiments on the kinetics and dynamics of surface processes. For the sake of this thesis we will be concentrating mainly on the kinetics aspect of molecular beam. For detailed studies on molecular beam and its application one may go through the books given in refs. 25 and 26.

A molecular beam is a well collimated, directed stream of gas. The probability of collision among the constituent atoms or molecules in a molecular beam is very low. The well-defined spatial distribution of molecular beams and the single collision condition makes it very useful for kinetics and dynamics studies on

the surfaces. The main feature of molecular beam approach in reaction kinetics study is that the molecular beam experiment is performed under single collision conditions, meaning that there is essentially a single interaction of the reactant molecules with the surface in a collision-free environment. As one can precisely measure the reactant flux of molecular beam, the measurement of absolute reaction probabilities as a function of the adsorbate coverage is possible. A fast beam switching which modulates the reactant flux, allows to obtain unique information on the transient kinetics. Generally molecular beam is generated from a beam source: an illustration of the basic setup of molecular beam is shown in figure 1.5. The first step is the expansion of gas from a well-defined state called stagnation state to the vacuum through an array of micro capillary called doser. For the dynamical studies, the distribution of energy over different external and internal degrees of freedom can be controlled precisely, and as there is collision free flow, this energy distribution is maintained till the beam collides with the surface or with another beam. For study of kinetics of a reaction with different reactants, the reactants can be introduced by combination of more than one molecular beams or through mixed beam.
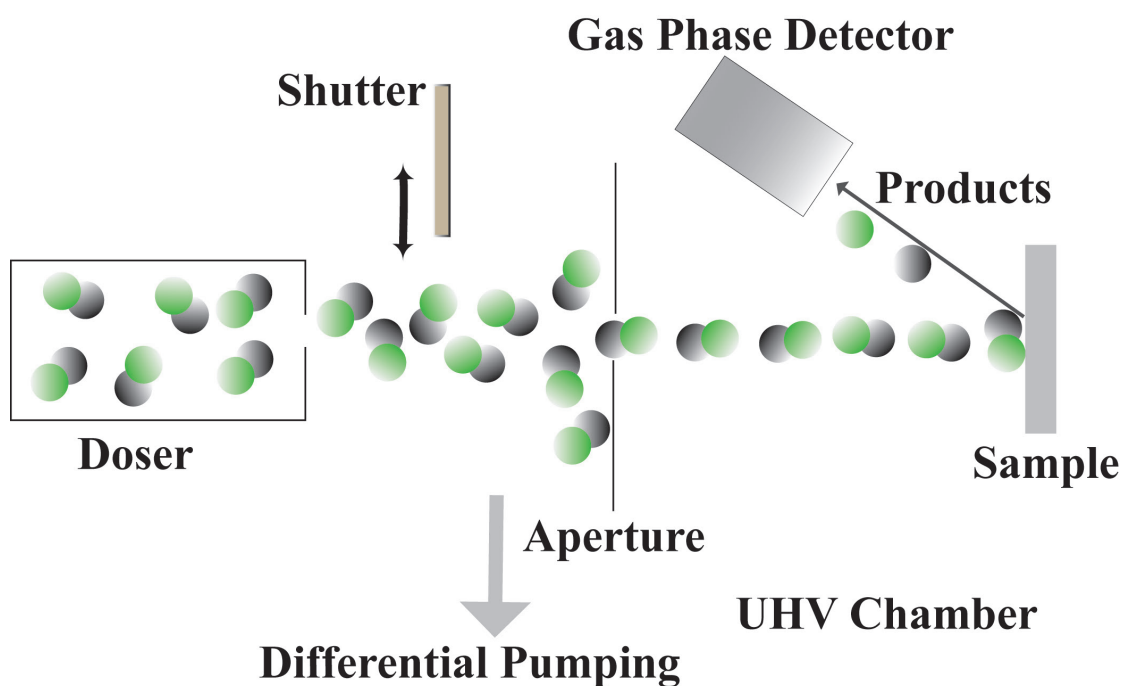
Figure 1.5 A basic setup of molecular beam generation.

The products or scattered reactant molecules are detected in the gas phase by two ways, one is angle integrated way, and the other is angle resolved way

by using quadrupole mass spectrometry (QMS), bolometry or laser spectroscopy. The angle resolved mode of detection gives the additional information about the spatial distribution of products. There are two types of molecular beams, effusive and supersonic beams. Beam type depends on the expansion conditions. The expansion conditions are identified by the Knudsen number $Kn = \lambda/d$ (λ is the mean free path of the gas molecules and d is the source aperture dimension). Supersonic sources operate at low Knudsen numbers. Starting from the stagnation state where Mach number is very lower than 1, which under extreme conditions reaches to sonic speed (Mach number, $M = 1$) and then acquires the supersonic speed ($M > 1$) upon further expansion from the nozzle. The main advantages of a supersonic beam source are: (a) narrow velocity distribution, (b) variable kinetic energy and (c) a large degree of control over the internal energy. Moreover, there are many methods available which can be deployed for the modification of the energy distribution or selection of specific excited states in flight. In studies of the gas–surface dynamics, of surface scattering and diffraction or of fast transient kinetics these unique features are important. The other kind of beam sources is effusive sources, which operate at large Knudsen numbers. There is very less intermolecular collision in the beam exiting the source in this type. Thus, the energy distribution in all degrees of freedom is determined by the temperature of the stagnation state, and specifically, by the velocity of the gas molecules, which follows a Maxwell–Boltzmann distribution. The unique advantages for effusive beam are a) high maximum intensity b) variable beam with very less changes in beam profile c) low stagnation state pressure which is helpful for beam generation of molecules with lower vapor pressure d) reduced gas consumption which helps to study the expensive isotopic species. However, the kinetic energy distribution is broad for effusive beams. Effusive beam is mostly helpful for studies of surface reaction kinetics, and the broad kinetic energy distribution does not play big interference. As only effusive beams are used in the present study, supersonic sources are not considered here. One or two stages of skimmer could be employed between the microcapillary doser and sample surface, to make the kinetic energy distribution to the narrow level. This would also reduce the molecular beam spot size significantly.

In the literature, different setup of molecular beam instrument has been described; they can be clubbed in two categories: one to study gas-surface dynamics [27-34]. This kind of setup basically require supersonic beam source with the

maximum of control over its dynamic parameters and optimized angular and time resolved detection of the scattered beam, and the other to study kinetics of the surface reactions [29, 32, 33, 35-43]. The main advantages of molecular beam technique can be summarized in the following:

1. Absolute reaction probabilities can be determined, from the known reactant flux sticking coefficient in case of adsorption and reactive sticking probabilities in surface reactions are determined. The experiments are performed by the fashion proposed by King and Well [44], therefore, this way of molecular beam approach is known as King and Well's method, in which determination of relative change in background pressure gives the sticking coefficient directly. Equation 1.1 gives the determination of sticking coefficient, s, by this method:

$$s(t) = \frac{1}{f} \frac{\Delta p(t)}{p_{eq}(t) - p_{base}(t)} \qquad (1.1)$$

Where f is the fraction of the beam intercepted by the sample surface, $\Delta p(t)$ is the difference between equilibrium partial pressure and transient partial pressure at time t, $P_{eq}(t)$ is the equilibrium partial pressure and $P_{base}(t)$ is the base pressure of the beam gas at time t. However, this method relies on fast response of the vacuum system, if the reactive gas interacts strongly with the chamber wall and if sticking coefficient is very low ($< 10^{-2}$) then this method cannot be directly applied.

2. Reactant flux can be modulated in a fast and flexible manner which helps in understanding the transient kinetics response.

3. The scattered and desorbed molecules can be detected in a collision-free manner. Though the local pressure on the sample surface can be anywhere between 10^{-2} to 10^{-6} mbar during the impingement of the beam to the sample, the background pressure remains several order lower [45]. This situation helps the detection of scattered or desorbed gas molecules to be collision-free even though the detector is situated far from the sample.

A simple effusive molecular beam setup was fabricated in our lab [46], mainly to study gas-surface reaction mechanism and kinetics. A brief overview of the setup and its doser assembly is described in the following:

An UHV chamber (12 liter) is equipped with an isothermal effusive molecular beam source. The chamber is pumped down to base pressure of 3×10^{-10} Torr by a

turbo molecular pump (Pfeiffer, TMU261, pumping capacity 210 L/s). The sample being a single crystal (diameter 8 mm, thickness 1 mm Pd(111)) or polycrystalline foil was mounted on a power-thermocouple feed through (Caburn, 30A DC and 5 kV) fitted at the end of an 3-axes manipulator with rotary platform. This feed through is connected to a liquid nitrogen well. Thus the crystal can be cooled up to 110 K. The sample is spot welded by a 0.5 mm tantalum wire and can be heated resistively up to 1373 K by a home-built temperature controller. A K-type thermocouple (chromel-alumel) is spot-welded at the periphery of the sample and thermocouple lead of the feed through to monitor the temperature. The chamber has one molecular beam doser assembly and a sputter ion gun (AG5000, VG Scientific) situated at 180° to each other and perpendicular to the above feed through, so that the sample can be faced towards the molecular beam during the reaction studies, and towards the sputter gun while cleaning. A stationary quadrupole mass spectrometer (Pfeiffer, Prisma QMS 200M3), which can detect gas phase species up to 300 amu, and a high vacuum gauge (Pfeiffer, IKR270) for measuring the chamber pressure are connected opposite to each other and away from the beam doser. The mass spectrometer is kept out of the line-of-sight of the sample to avoid any angular desorption effects. Both the QMS and ion gauge are kept within the equal distance from the TMP to minimize any disparity in the pressure readings by them. Figure 1.6 shows the schematics of the molecular beam setup. The doser consists of multichannel array of micro capillaries. The disk diameter is 13 mm, i.e. higher than the diameter of the sample. Low energy molecular beams can be generated by this array of micro capillary tubes [47]. The quality of the doser depends on its Enhancement factor (E). This is the ratio between the true gas flux on the sample surface due to the doser and the flux at pressure P. Equation 1.2 gives the enhancement factor:

$$E = 1 + \left[\frac{fS}{k_B T (1 - fS) v_c A} \right] \qquad (1.2)$$

where, v_c is the velocity of the gas molecules, , f is the fraction of beam intercepted by the sample, S is the pumping speed, k_B Boltzmann constant, T is the temperature, s is the sticking probability of the molecules, A is the surface area of the sample, and m is the mass of the gas molecule.

The beam profile depends on the aspect ratio, which is the ratio of length (L) and diameter (a) of a micro capillary. The beam profile does not change

much, except some change in conductance in a micro capillary with aspect ratio greater than 40. Zaera et al. [48] showed that the beam quality was good for a microcapillary with a $=$ 10 μm than that of a larger diameter (a$=$50 μm) with same lengths of capillary (L $=$ 2 mm). In our set up the aspect ratio is 100, which gives a uniform beam on the sample surface (diameter 8 mm). The molecular beam doser consists of a 13 mm disk multichannel array made up of microcapillary glass tubes of 1 mm in length and 10 μm in diameter each (Collimated Holes Inc.). The doser is attached through a threaded cap and head with teflon O-rings. The open portion of the above microcapillary is only 10 mm, due to the above design in holding the capillary. A quarter inch tube (OD) of 15 cm in length with baffles (shown in figure 1.7) is attached with the beam-doser head to avoid the gas taking the shape of the tube. In this way a minimum dead volume and a minimum gas load can be maintained. A laterally movable stainless steel shutter, which is
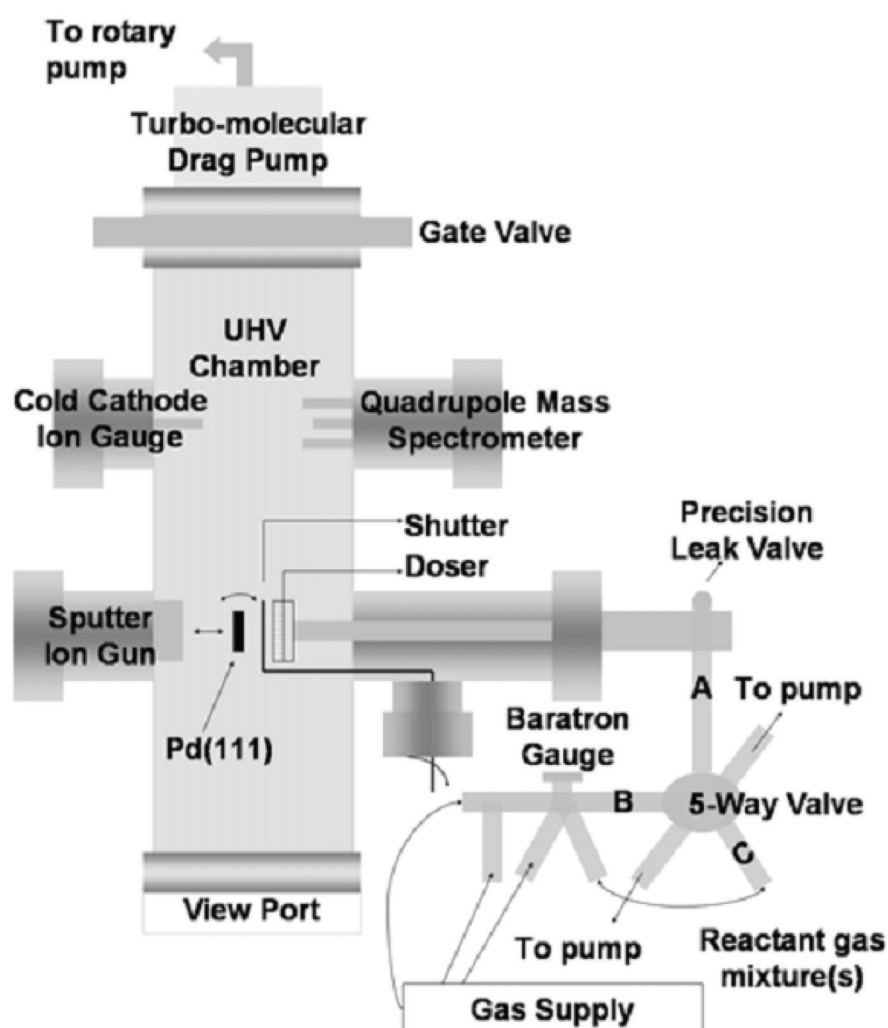
Figure 1.6 shows the schematics of the MBI.

manually operated, is placed between the microcapillary doser and the sample in order to interrupt the beam if desired (Fig. 1.7 inset). We could maintain a minimum of 5 mm doser to sample distance in our present setup, which gives an enhancement factor (E) of ∽12 [49] and ∽ 45 % fraction of the beam (f) impinges on the surface. The gas is flowed through the doser by a precision leak valve. The flux is calibrated by keeping the gas pressure same in the gas manifold and same leak rate through the leak valve. For reaction with two or three reactants gases are mixed in the gas manifold and used as a mixed molecular beam.

The molecular beam experiments give direct information about the kinetics and dynamics of the surface processes and reactions on the surfaces, sticking coefficient and coverages can be determined quantitatively which helps to design microkinetic modelling of reaction kinetics for the elementary steps of the reaction, nonetheless, the two main features of molecular beam experiments distinguish it from the real world catalysis. The one is molecular beam operates far from the thermodynamic regime, and the other is that molecular beam cannot provide
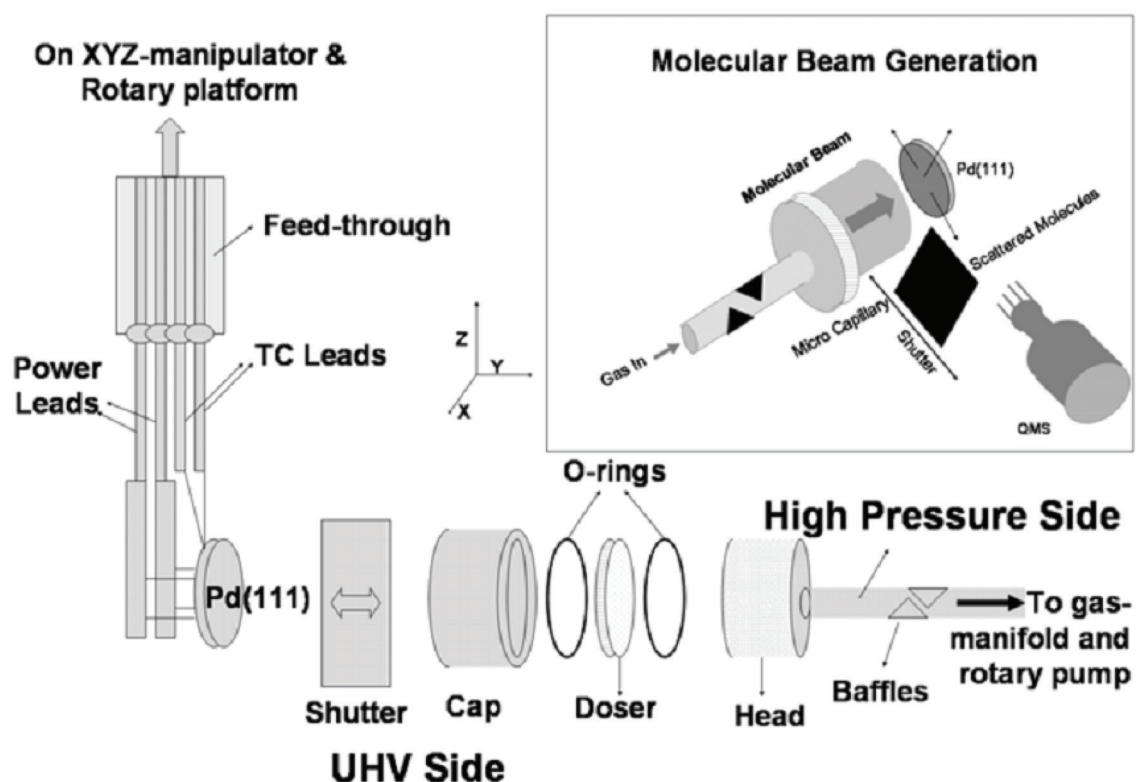
Figure 1.7 Schematics of the doser assembly and in the inset is shown the beam generation.

effective pressures at the crystal surface higher than 10^{-2} Torr/s or usually 10^{-4} - 10^{-5} Torr. In addition, their advantages generally apply to reactions with reasonably high probabilities [50, 51].

§ 1.3 Ambient Pressure Photoelectron Spectroscopy

Photoelectron spectroscopy (PES) is a very popular and widely used surface sensitive technique, very useful for surface composition and electronic structure information. The technique was successfully converted into a full-fledged equipment in Uppsala, Sweden by Kai Siegbahn. XPS has been available since the mid-1960s and has been an indispensable tool to chemists and physicists in unraveling the electronic structure of many compounds and materials of interest [52]. XPS works on the basic principle of photoelectric effect. By shining UV/X-ray photons on a solid surface, electrons are ejected from the valence and core levels. Energy conservation is governed by the fundamental equation (eq 1.3). The binding energy (BE) is the energy required to excite an electron from any occupied level to the Fermi level (E_F), the additional energy required to remove an electron from E_F into vacuum is the work function (φ) of the solid, and the remaining energy is associated with the ejected electron in the form of kinetic energy (KE), which depends on the photon energy (eq 1.3). Electrons that are ejected into the vacuum should reach the detector, without any inelastic collision with any other atoms/molecules within the solid surface layers or in vacuum; due to this stringent requirement, ultrahigh vacuum (UHV) ($\leq 10^{-9}$ mbar) is maintained in XPS spectrometers. The electrons have very short mean free path at higher gas pressures. For example, the mean free path of 400 eV electrons in 1 mbar O_2 is approximately 4 mm [53].

$$h\nu = BE + KE + \phi \hspace{4cm} (1.3)$$

The pressure difference between UHV measurement conditions in XPS and the actual working conditions of the materials was often considered as a reason for disconnect between the results obtained from XPS and exact reaction phenomena. The past decade has seen a real impetus in developing new tools for probing materials at realistic conditions or closer toward that [54].The demanding needs of environmental and catalysis science have driven the advancement of photoelectron spectroscopy to function at higher pressures. For instance, rational design of new functional materials, whose properties are solely dependent on surface or subsurface phenomena, needs to be understood at the molecular

level under in-situ conditions as well as in a time resolved manner. The time-resolved fast XPS results using synchrotron radiation were helpful to elucidate the reaction mechanisms of several industrially relevant catalytic problems [55]. The high brilliance of synchrotron radiation available worldwide has also aided in developing and creating facilities for doing photoelectron spectroscopy at near ambient pressure (up to few mbar). This state-of-the-art technique though has been available to few synchotron beamlines, laboratory based versions are also available, however, to a very limited number of research groups.It is named in many ways, such as High pressure X-ray Photoelectron Spectrsocopy (HP-XPS), or Ambient Pressure Photoelectron Spectroscopy (APPES or AP-XPS), Near Ambient Pressure XPS (NAP-XPS) or *in situ* XPS. It is worth mentioning that the new generation of APPES evolved due to the constant efforts by several groups around the globe who contributed to the development of APPES. In the late 1970s, M. W. Roberts, Cardiff University, attempted to bridge the above pressure gap, but with limited success. Nonetheless, it was successfully attempted by Robert Schlögl's group at Fritz-Haber Institute, Berlin, and Miquel Salmeron's group at the University of California, Berkeley, during the past decade. Of course, there are few other groups who also built their own Lab-APPES, and notably, H.-P. Steinrück, University of Erlangen-Nürnberg, is one among them. Indeed, the APPES measurements could be carried out with either laboratory X-ray sources or with synchrotron radiation. The popularity of this technique among the researchers is evident from the commissioning of Lab-APPES by a few other groups [56, 57]. Several aspects which are very important in APPPES, are briefly described here.

1.3.1 Electron - Gas Interactions:

The main problem of PES at high pressure is the scattering of electrons by gas molecules. The attenuation of the photoelectron signal follows Beer's law $I = I_0 e^{(-z\sigma(KE)p/kT)}$, I being the intensity at pressure p; I_0 the signal in UHV; $\sigma(KE)$ the electron scattering cross section (which depends on the electron KE and type of gas); and z the distance traveled by electrons in the gas at pressure p and temperature T. The ballistic collision with gas molecules can cause elastic scattering of the electrons, which causes attenuation due to electrons scattered out of the acceptance angle of the spectrometer cone. If the aperture diameter of cone, attached to the bottom of the electrostatic lens column, is smaller than the X-ray

spot size, then elastic scattering will be small. Some electrons will be scattered out of the spectrometer acceptance angle, and some will be scattered in. And if the X-ray spot size is smaller than the aperture diameter, inelastic scattering can be due to excitation of atomic or molecular rotational vibrational or electronic states or due to ionization of the atoms/molecules. Inelastic scattering depends on the type of gas, and is generally strongest at a KE of about 100 eV. Figure 1.8 shows the scattering cross section distribution of electrons in water vapor with incresing kinetic energy[58]. The inelastic scattering is at maximum for electrons of KE 100 eV. The inelastic scattering shows the pattern similar to that of inelastic
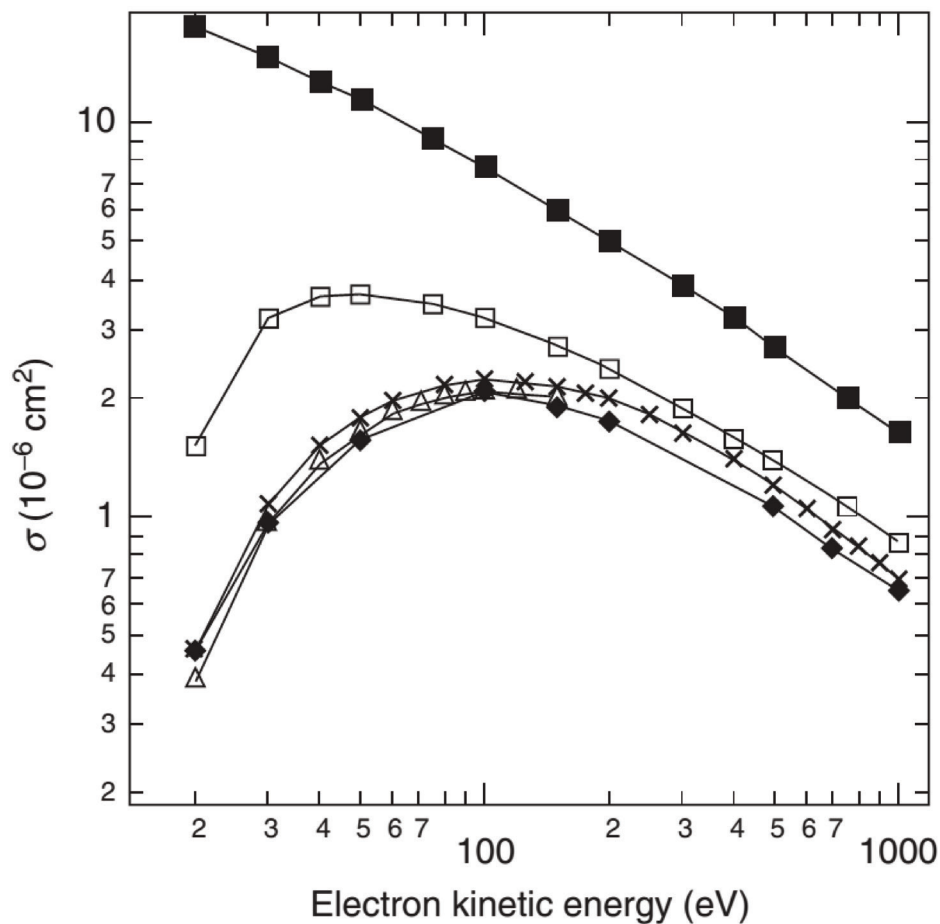
Figure 1.8 Inelastic electron scattering cross section of water as a function of electron kinetic energy. (The data are taken from Schutten et al. (♦), Ref. [59]; Djuric et al. (△), Ref. [60]; Straub et al. (×), Ref. [61]; and Munoz et al. (□), Ref. [62]. The total electron scattering cross section from Munoz et al. (■) is also shown. It contains the contributions of the inelastic, elastic, and rotational scattering cross sections. Reused with permission from Ref [63].

mean free path of electrons in solid. The experimental data for attenuation of electrons in presence of water vapor is presented in Figure 1.9. It is to be noted that attenuation of 700 eV KE electrons are lower than 100 eV KE electrons by a factor 30. The data were obtained by recording the C 1s peak area (I) of
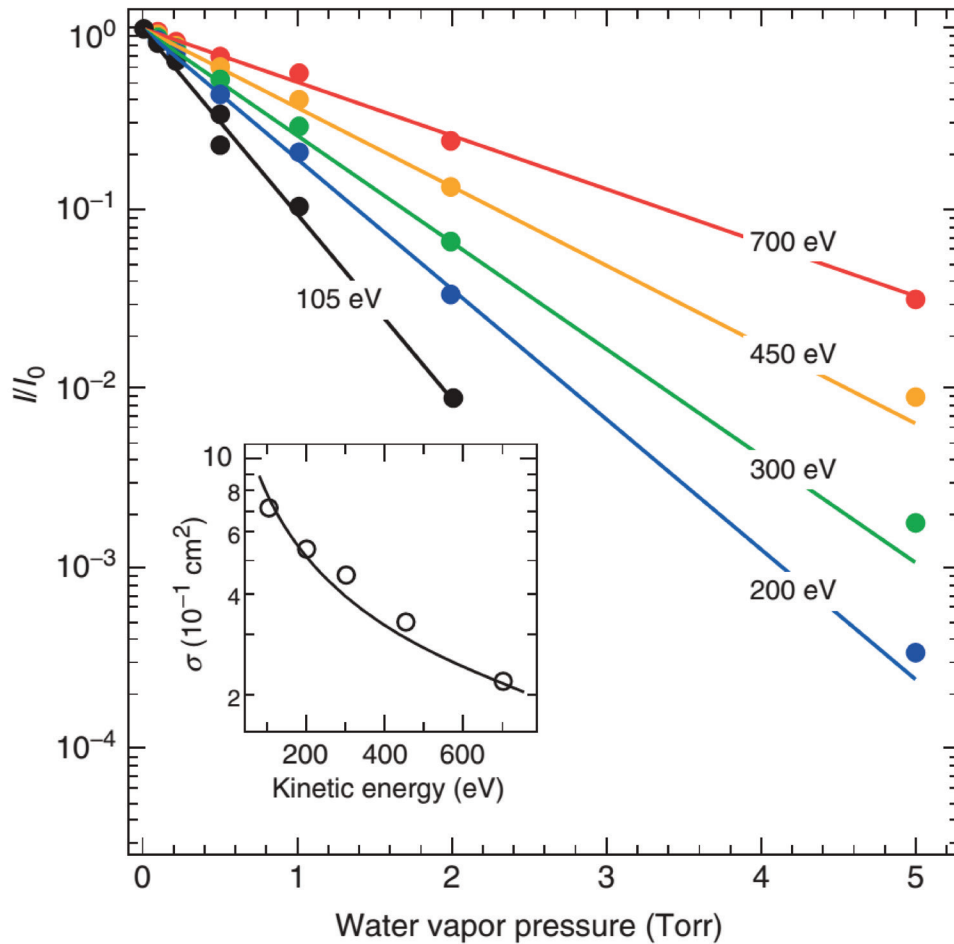
Figure 1.9 Attenuation of the photoelectron signal as a function of water vapor pressure and electron kinetic energy. The inset shows a comparison of the experimental data (o) with the data from Ref. [62](Reproduced with permission from Ref. [63].)

a graphite sample that was placed 0.9 mm distance from the 0.3 mm diameter entrance aperture of the differential pumping stage. The data are normalized to the peak intensity under vacuum conditions (I_0). The data points are fitted to the lines. From the slope of the fits, the total electron scattering cross sections can be determined.

The density of gas phase at 1 Torr is about 10^6 times lower compared to

the solid. The inelastic mean free path of electrons in solid being of the order of nm, will be around mm in gas (1 Torr). However, electron has to travel much (1m) to reach the detector. This implies to use efficient and several differential pumping stages in the analyzer. The sample is kept within a short distance from the analyzer cone to minimize the high pressure zone travel of the photoelectrons. By reducing the aperture diameter of the analyzer cone, the differential pumping can be improved. However, reducing the cone aperture size reduces the electron counts. One feasible solution could be to increase X-ray photon flux in a very small spot size. This is the reason that most of the APPES systems use synchrotron sources. This again invites technological constraints as well as possibility of sample damage.

One way to achieve better electron transmission without increasing aperture size or photon flux is to use focusing lens for each differential pumping stages. This was the technological improvement for the second generation of APPES systems (schematically shown in Figure 1.10).
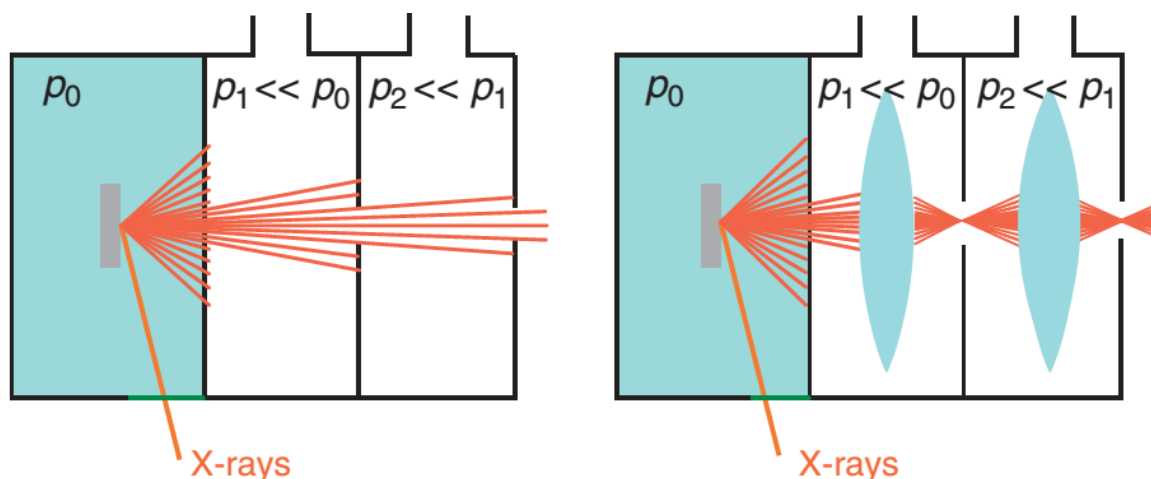
Figure 1.10 Illustration of the evolution of electron analyzer design.

1.3.2 X-ray Photon-Gas Interactions

The photon-gas interaction is much weaker than electron-gas interaction. The electron-gas scattering cross section is higher than the photon –gas scattering cross section. However, attenuation of photon with gas molecules is a secondary phenomenon in APPES experiments. Generally, the APPES high resolution analyzers are able to detect the pure gas-phase signals as well. Depending on the surface work function and surface potential, shift in the gas phase spectrum can be

observed, which indirectly helps to determine the work function of a surface in situ. The absorption of X-ray photons by gas molecules helps in charge compensation of the samples/ insulators during APPES experiments. This is fortunate as low energy electron or ion gun which are used for charge compensation for insulating samples in conventional XPS, cannot be feasibly used in APPES setup.

1.3.3 Gas Flow and Differential Pumping

The mean free path of electrons λ_e depend on the energy of the electrons and gas pressure, P. So, as the pressure is increased the λ_e decreases, as a result the sample need to be placed closer to the analyzer cone aperture. However, the distance (d) between the sample surface and the cone should be decreased to an optimum distance, as pressure inhomogeneity develops near the region of the cone aperture. Gas dynamic calculation shows that at a distance of aperture diameter $(d = D_0)$, the local pressure is 95 % of the actual pressure. Generally, the distance between sample surface and the aperture is kept $>D_0$ to avoid any pressure inhomogeneity and surface perturbation due to analyzer cone. As the APPES system maintains from very high vacuum to high pressure (say, 1 mbar), different gas flow regimes can be observed within the APPES experimental conditions. Gas flow regimes are generally described by Knudsen number (K_n), being the ratio of mean free path of the gas molecule (λ_{gas}) and the diameter of the aperture (D_0). In low pressure conditions, the flow can be described by molecular flow as in UHV systems. At the limits of working pressures of APPES (1 to few mbar), the $\lambda_e \backsim D_0$ the Kn varies from 1 to 10, and the gas flow can be described by molecular flow. However, in high pressure the analytical description of flow regime is critical.

1.3.4 Sample Contamination

The great challenge in APPES experiments is sample contamination. In conventional UHV surface techniques unwanted surface contamination can be avoided very easily; however, in APPES which works in few orders of magnitude higher pressure this is a matter of concern. Contamination can be from gas source or from the adsorbed moieties on the chamber walls. Therefore, purity of reactant gases and frequent bake out of the system is preferred. During the experiments, care should be given to analyze probable contaminating species, like hydrocarbon.

§ 1.4 References

[1]. C. B. Duke, *Progress Nat. Ac. Sc.* **2003**, 100, 3858-3864.

[2]. Z. Ma, F. Zaera, Heterogeneous Catalysis by Metals in Encyclopedia of Inorganic Chemistry, John Wiley, **2006**.

[3]. The Collected Works of Sir Humphry Davy, ed. J. Davy, Smith, Elder, and Co., Cornhill, London, **1840**.

[4]. L. Gmelin, Hand-book of Chemistry, Harrison and Sons, London, **1862**.

[5]. Nora M. McLaughlin, Marco J. Castaldi, *Catalysis* **2009**, 21, 191–218.

[6]. (a) Gerhard Ertl, *Angew. Chem. Int. Ed.* **2008**, 47, 3524 – 3535. (b) G. Ertl, D. Prigge,R. Schlögl, D. Weiss, *J. Catal.* **1983**, 79, 359.

[7]. I. Langmuir, *Trans. Faraday Soc.* **1922**, 607.

[8]. (a) G. Ertl, *Angew. Chem.* **1990**, 102, 1258; (b) G. Ertl, *Angew. Chem. Int. Ed.* **1990**, 29, 1219.

[9]. P. Stoltze, *Phys. Scr.* **1987**, 36, 824.

[10]. J. Libuda, H.-J. Freund, *Surface Science Reports* **2005**, 57, 157–298.

[11]. M. Jacoby, *Chemical and Engineering News* **1998**, 41.

[12]. R. Schlögl, *Angew. Chem. Int. Ed.* **1993**, 33, 381-383.

[13]. P. Stoltze, J. K. Norskov, *Phys. Rev. Lett.* **1985**, 2502.

[14]. V. P. Zhdanov, V. I. Sobolev, V. A. Sobyanin, *Surf. Sci.* **1986**, 175, L747.

[15]. V.P. Zhdanov, B. Kasemo, *Appl. Surf. Sci.* **1994**, 74, 147.

[16]. C. V. Ovesen, B.S. Clausen, J. Schiotz, P. Stoltze, H. Topsoe, J. K. Norskov, *J. Catal.* **1997**, 168, 133.

[17]. V. P. Zhdanov, B. Kasemo, *Surf. Sci. Rep.* **1997**, 31.

[18]. P. Stoltze, *Progr. Surf. Sci.* **2000**, 65.

[19]. G. A. Somorjai, J. Y. Park, *J. Chem. Phys.* **2008**, 128, 182504.

[20]. G. A. Somorjai, Introduction to Surface Chemistry and Catalysis, (Wiley, New York, **1994**).

[21]. C. T. Campbell, *Surf. Sci. Rep.* **1997**, 27, 1.

[22]. M. Valden, X. Lai, and D. W. Goodman, *Science* **1998**, 281, 1647.

[23]. C. B. Duke, *Chem. Rev.* **1996**, 96, 1237.

[24]. G. Comsa, *Surf. Sci.* **1994**, 300, 77–91.

[25]. R. Campargue, Atomic and Molecular beams: The state of the art 2000, Springer Verlag, Berlin and Heidelberg, **2001**.

[26]. G. Scoles, D. Bassi, U. Buck and D. Lainé, Atomic and Molecular Beams Methods I, Oxford University Press, Oxford, **1988**.

[27]. J.A. Barker, D.J. Auerbach, *Surf. Sci. Rep.* **1985**, 4, 1.

[28]. C.T. Rettner, D.J. Auerbach, J.C. Tully, A.W. Kleyn, *J. Phys. Chem.* **1996**, 100, 13021.

[29]. S.T. Ceyer, W.J. Siekhaus, G.A. Somorjai, *J. Vac. Sci. Technol.* **1981**, 19, 726.

[30]. M. E. M. Spruit, E.W. Kuipers, M.G. Tenner, J. Kimman, A.W. Kleyn, *J. Vac. Sci. Technol.* **1987**, A 5, 496.

[31]. M.G. Tenner, E.W. Kuipers, W.Y. Langhout, A.W. Kleyn, G. Nicolasen, S. Stolte, *Surf. Sci.* **1990**, 236, 151.

[32]. K.D. Gibson, S.J. Sibener, *J. Chem. Phys.* **1988**, 88, 791.

[33]. L.S. Brown, S.J. Sibener, *J. Chem. Phys.* **1988**, 89, 1163.

[34]. J. Häger, H. Walther, *Annu. Rev. Mater. Sci.* **1989**, 19, 265.

[35]. C. Duriez, C.R. Henry, C. Chapon, *Surf. Sci.* **1991,** 253, 190.

[36]. B.N. Eldridge, M.L. Yu, *Rev. Sci. Instrum.* **1987**,58, 1014.

[37]. M. Balooch, W.J. Siekhaus, D.R. Olander, *J. Phys. Chem.* **1984**,88, 3521.

[38]. J. Liu, M. Xu, T. Nordmeyer, F. Zaera, *J. Phys. Chem.* **1995**, 99, 6167.

[39]. S.M. Wetterer, D.J. Lavrich, T. Cummings, S.L. Bernasek, G. Scoles, *J. Phys. Chem. B* **1998**, 102, 9266.

[40]. K. Hayek, M. Fuchs, B. Klötzer, W. Reichl, G. Rupprechter, *Top. Catal.* **2000**, 13, 55.

[41]. I. Stara, V. Matolin, *Surf. Sci.* **1994**, 313, 99.

[42]. R. Denecke, M. Kinne, C.M. Whelan, H.-P. Steinrück, *Surf. Rev. Lett.*

2002, 9, 797.

[43]. J. Libuda, I. Meusel, J. Hartmann, H.-J. Freund, *Rev. Sci. Instrum.* **2001**,71, 4395.

[44]. D.A. King, M.G. Wells, *Surf. Sci.* **1972**, 29, 454.

[45]. K. Nakao, S. Ito, K. Tomishige, K. Kunimori, *J. Phys. Chem. B* **2005**, 109, 17579.

[46]. Kandasamy Thirunavukkarasu, Chinnakonda S. Gopinath, *Catal Lett* **2007**, 119, 50.

[47]. Pauly, H., Scoles, G. (Ed.) , Atomic and Molecular Beam Methods, 1 (Oxford University Press) **1988**, 99.

[48]. J. M. Guevremont, S. Sheldon, F. Zaera, *Rev. Sci. Instrum.* **2000**, 71, 3869.

[49]. C. T. Campbell, S. M. Valone, *J. Vac. Sci. Technol. A* **1985**, 3, 408.

[50]. M. J. Cardillo, M.J. *Ann. Rev. Phys. Chem.* **1981**, 32, 331 and references therein.

[51]. G. Prada-Silver, K. Kester,D. Loftier, G. L. Hailer, J. B. Fenn, *Rev. Sci. lnstrum.* **1977**, 48, 897.

[52]. K. Siegbahn, C. J. Allan, Electron Spectroscopy for Chemical Analysis. MTP Int. Rev. Sci.: Anal. Chem. **1973**, 12, Part 1.

[53]. M. Salmeron, R. Schlögl, *Surf. Sci. Rep.* **2008**, 63, 169.

[54]. M. Hünger, J. Weitkamp, *Angew. Chem. Int. Ed.* **2001**, 40, 2954.

[55]. (a) P. Sören, P. Jiang, F. Borondics, S. Wendt, Z. Liu, H. Bluhm, F. Besenbacher, M. Salmeron, *Angew. Chem. Int. Ed.* **2011**, 50, 2266 - 2269. (b) D. J. Miller, H. Öberg, S. Kaya, H. S. Casalongue, D. Friebel, T. Anniyev, H. Ogasawara, H. Bluhm, L. G. M. Pettersson, A. Nilsson, *Phys. Rev. Lett.* **2011**, 107, 195502. (c) J. R. Renzas, W. Huang, Y. Zhang, M. E. Grass, D. T. Hoang, S. Alayoglu, D. R. Butcher, F. Tao, Z. Liu, G. A. Somorjai, *Phys. Chem. Chem. Phys.* **2011**, 13, 2556 -2562. (d) J. L. Hueso, D. Martínez-Martínez, A. Caballero, A. R. Gonzalez-Elipe, B. S. Mun, M. Salmeron, *Catal. Commun.* **2009**, 10, 1898 - 902.

[56]. D. E. Starr, Z. Liu, M. Hävecker, A. Knop-Gericke, H. Bluhm, *Chem. Soc. Rev.* **2013**, 42, 5833-5857.

[57]. S. K. Eriksson, M. Hahlin, J. M. Kahk, I. J. Villar-Garcia, M. J. Webb, H. Grennberg, R. Yakimova, H. Rensmo, K. Edstroem, A. Hagfeldt, H. Siegbahn, M. O. M. Edwards, P. G. Karlsson, K. Backlund, J. Åhlund, D. J. Payne, *Rev. Sci. Instrum.* **2014**, 85, 075119/075111-075119/075111, and references there in.

[58]. A. Shavorskiy, H. Bluhm, in Heterogeneous Catalysts for Clean Technology, Wiley-VCH Verlag GmbH & Co. KGaA, **2013**, pp. 437-468, and references there in.

[59]. J. Schutten, F. J. deHeer, H. R. Moustafa, A. J. H. Boerboom, J. Kistemaker, *J. Chem. Phys.* **1996**, 44, 3924.

[60]. N. L. Djuric, I. M. Cadez, M. V. Kurepa, *Int. J. Mass Spectrom. Ion Processes* **1988**, 83, R7.

[61]. H. C. Straub, B. G. Lindsay, K. A. Smith, R. F. Stebbings, *J. Chem. Phys.* **1998**, 108, 109.

[62]. A. Muñoz, J. C. Oller, F. Blanco, J. D. Gorfinkiel, P. Limão-Vieira, G. Garćıa, *Phys. Rev. A* **2007**, 76, 052707.

[63]. H. Bluhm, *J. Electron Spectrosc. Relat. Phenom.* **2010**, 177, 71-84.

Chapter 2

Design and Performance Aspects of a Custom-Built Ambient Pressure Photoelectron Spectrometer
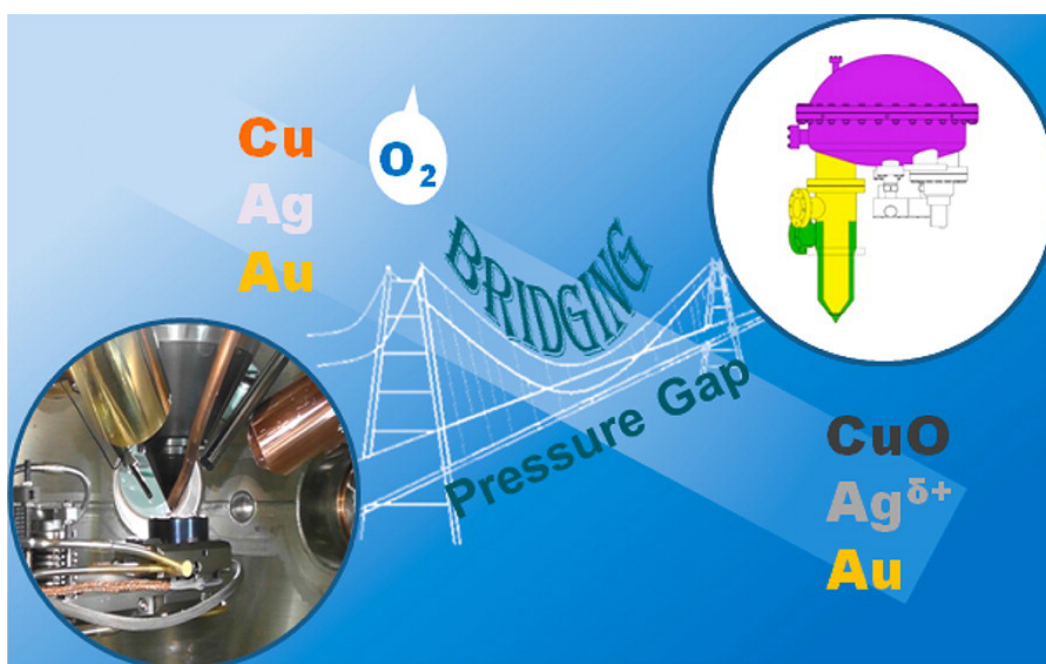
The critical features of a custom-built laboratory version ambient pressure photoelectron spectrometer (Lab-APPES) are presented. A double front cone differential pumping arrangement and an aperture free design employed in the electrostatic lens regime improve the data collection and data quality. In contrast to the conventional X-ray photoelectron spectrometers (XPS) operating at ultrahigh vacuum (UHV), it is possible to explore the electronic structure of solid surfaces under working conditions or closer to working conditions with Lab-APPES. Especially surface-dependent phenomena can be explored up to 1 mbar pressure and up to 873 K by conventional heating methods and at least up to 1273 K by a laser heating method. Simultaneous XPS and reaction kinetic measurements on solid surfaces make the Lab-APPES an important tool to measure the dynamic electronic structure changes on material surfaces under reaction conditions. The interaction of O_2 with polycrystalline foils of Cu, Ag, and Au from UHV to 1 mbar and up to 773 K has been studied.

§ 2.1 Introduction

APPES has been used to investigate variety of samples under different reaction conditions (e.g., temperature, pressure, gas composition, UV irradiation, electrical bias). The specific research findings are not reviewed here in this chapter. One may refer the literature for interest [1]. In fact, there is an increased interest in this area which reflects from the increase in number of research publications around the globe. Nonetheless, this facility was limited to few synchrotron end stations; development in analyzer design and improvement in differential pumping system as well as characteristic X-ray generation, it is now accessible to few research labs. Recently, a custom-built Lab-APPES unit was commissioned at CSIR-National Chemical Laboratory (NCL), Pune (Figure 2.1). Basic design features were provided by NCL, Pune, and the system was supplied by Prevac, Poland. XPS measurements can be made up to 1 mbar pressure and up to 1273 K on the solid surfaces in the above Lab-APPES system. A systematic study which shows the transformation of coinage metal surfaces has been chosen to demonstrate the capabilities of the system.
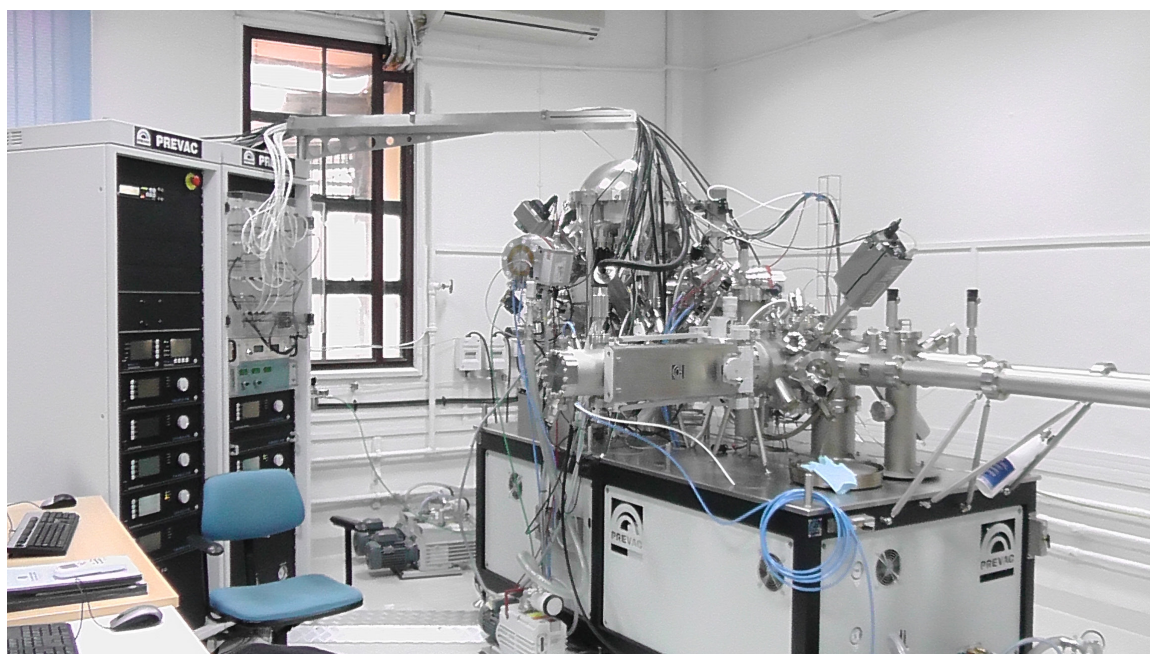
Figure 2.1 Photograph of the Lab-APPES at CSIR-NCL, Pune installed in May 2012.

§ 2.2 Experimental Section

General features that are common for APPES are already discussed and available in literature [2], and they are not mentioned in this section. Those aspects that are relevant and special to our APPES system are described in detail. Following major advancements in the instrumentation, particularly, contributed to the development of APPES around the world. Over the past decade, an advanced electrostatic lens regime (ELR) with effective electrostatic focusing has been developed. In the conventional (UHV) XPS units, electrons that are collected from the sample surface into the ELR undergo divergence, and hence the number of electrons decreases when they pass through each aperture. However, in APPES this cannot be affordable, since the number of electrons collected into the ELR at high pressure is significantly lower. This is simply due to more inelastic collisions that occur at high pressures, say 1 mbar. Hence, to retain the electrons that are collected into the ELR, three important parameters are adapted in the analyzer (VG Scienta R3000HP) of the Lab-APPES at NCL, Pune.

First, the sample surface is kept very close to the tip of the cone attached to the ELR (effective differential pumping starts here), mainly to minimize the loss of electrons due to inelastic collisions at 1 mbar. The above distance is typically 1-2 mm in our Lab-APPES system, and depends on the cone aperture (0.8 or 1.2 mm) employed. Electrons with a KE of 400 eV in 1 mbar O_2 atmosphere can survive up to 4 mm, before they undergo inelastic collisions [2]. It underscores the necessity of decreasing the distance between the sample surface and the tip of the ELR. Once electrons enter into the ELR, two main factors contribute to obtain high quality spectral data, namely, effective differential pumping and the converging of electrons in the ELR. Effective differential pumping creates a better vacuum in the ELR. At 1 mbar N_2 pressure on the sample surface, a vacuum of 5×10^{-4}, 10^{-6}, and $10^{-7} - 10^{-8}$ mbar is maintained in the first and second differential pumping sections in the ELR and in the third differential pumping in the electron energy analyzer (EEA), respectively. First, second, and third differential pumping regimes are pumped down by a combination of 400, 300, and 400 L/s turbo molecular pumps, backed by rotary pumps. The area pumped increases gradually from first to second ELR to EEA. Further, a special design of a double front cone pumping arrangement (Figure 2.2) is available in the ELR. Both cone regions are shown in different colors. The main advantage with this design is a fast decrease in pressure

with a steep pressure gradient from the bottom of the cone (which is very close to the sample surface) to the EEA. This helps to minimize inelastic scattering in the ELR. Another critical factor that minimizes the loss of electrons in the ELR is the utilization of the advanced concept of electron converging in the ELR. In contrast to the conventional ELR, electrostatic voltages in the R3000HP model analyzer are applied in such a way that they converge all the electrons. Further, unlike other high pressure electron analyzers, R3000HP employs an aperture free ELR (Figure 2.2b). This design enables the study of angle-resolved XPS and fast data acquisition under 1 mbar conditions. Fundamentally, an electrostatic lens in the APPES unit refocuses the electron trajectory in such a way that electrons are converged due to the applied potential.
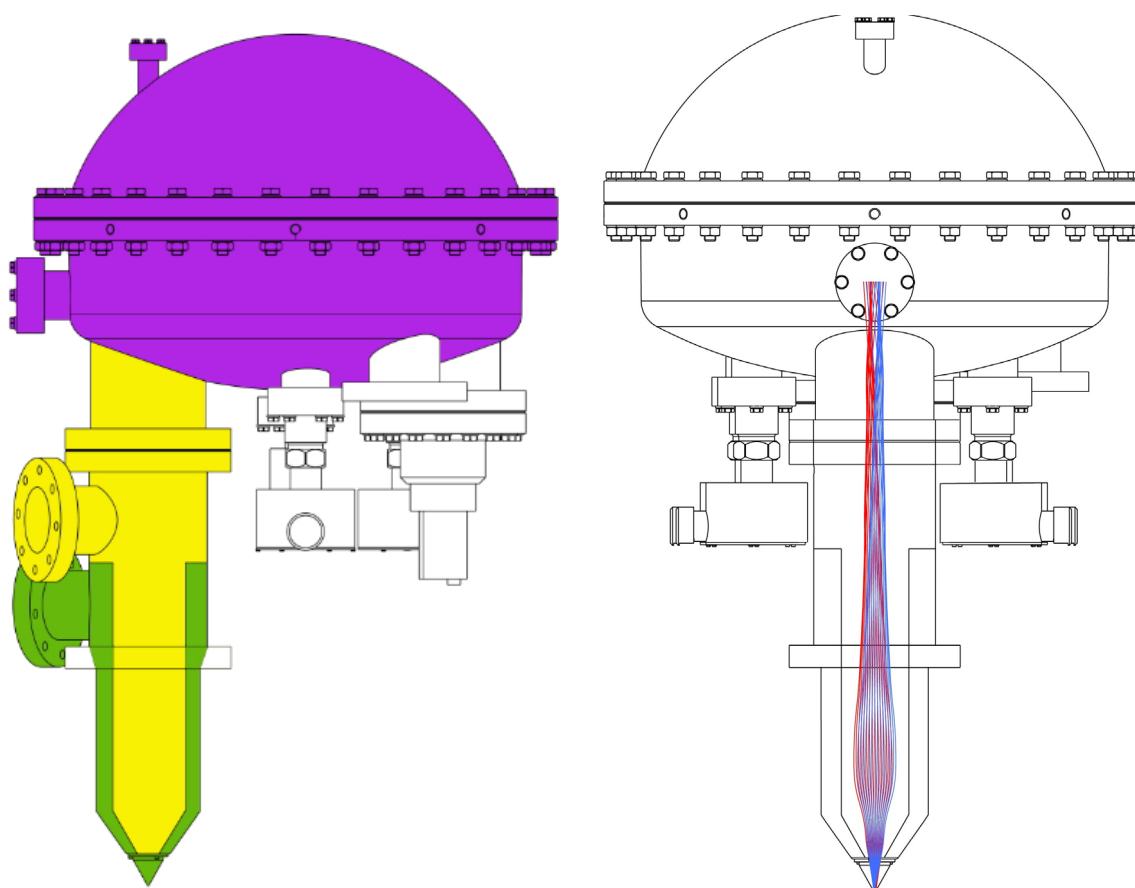
Figure 2.2 (left) A double front cone pumping arrangement effectively improves the differential pumping to minimize inelastic scattering in electrostatic lens regime (ELR) as well as to decrease the data collection time under high-pressure conditions. The electron energy analyzer region is shown in purple. (right) A schematic of the aperture free ELR and the electron trajectory for faster data acquisition.

Apart from the above advancement in the ELR, a few other critical design aspects are also incorporated. (a) An exchangeable cone with different apertures ($0.3 - 5$ mm) can be fitted to the tip of the ELR. A 0.8 mm aperture was fitted in the APPES system for high-pressure XPS measurements, and the data reported in this chapter are obtained with the above aperture and at a distance of 1.2 mm. Indeed, this cone separates the ELR and EEA regions through effective differential pumping to maintain increasingly better vacuum from the high-pressure region on the sample surface in the analysis chamber. (b) The highest resolution achieved is 0.42 ± 0.02 eV with 50 eV pass energy at a (analyzer entrance) slit width of 0.2 mm, and it is in good agreement with that reported for the R3000HP by Mangolini et al. [3]; however, the resolution measured is 0.6 ± 0.02 eV with the maximum slit width of 3.0 mm of the analyzer. Apart from the R3000HP analyzer, our Lab-APPES system has several distinctive features for analysis and experimentation. These are discussed in the following sections. A simplified pumping diagram of the analysis chamber is shown in figure 2.3.
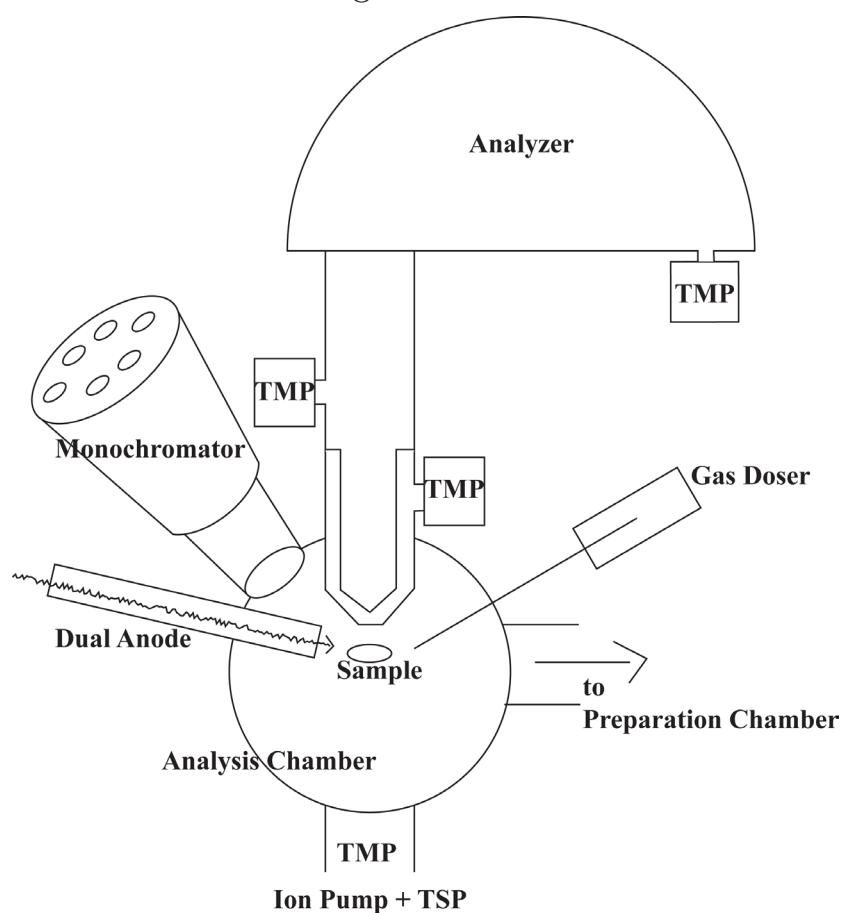
Figure 2.3 Simplified Illustration of the Analysis Chamber (UV discharge lamp is not shown).

The instrument carries two excitation sources for carrying out XPS. One is a conventional dual anode (Al Kα and Mg Kα) which can work up to a maximum power of 600 and 400 W, respectively. The other excitation source is an Al Kα monochromator MX 650 from VG Scienta. The X-rays work with an acceleration voltage of a maximum of 15 kV with a maximum output power of 650 W. The X-ray monochromator is isolated from the analysis chamber by a thin aluminum window (5 μm) mounted in a ring and inserted into the port separating analysis chamber and monochromator through a 150 CF axis port. The aluminum window efficiently seals the monochromator region, and hence the analysis chamber could be held at 1 mbar during high-pressure experiments with a stable monochromatic X-ray generation by the MX650. Easily a vacuum level of 10^{-6} mbar is maintained in the X-ray monochromator regime, when the analysis chamber pressure is at 1 mbar. This effectively minimizes X-ray absorption by gas phase molecules to a negligible level in the monochromator regime. Apart from Al and Si_3N_4, graphene oxide has been reported recently to be effective for X-ray transmission under high-pressure conditions [4] The analysis chamber is also equipped with a UV source which can give stable He I and He II UV radiation for doing valence band photoelectron spectroscopy (UVPES). The water-cooled UV source is mounted on a CF40 flange which can give an emission current up to 100 mA for He I and 200 mA for He II. Data obtained from XPS and UVPES at high pressure would be complementary, since valence band features from different elements can be identified. An electron flood source operating between 0 and 500 eV for charge compensation during XPS operation is attached to the analysis chamber. This is not only useful for analyzing insulating or semiconducting materials with XPS but also under 1 mbar conditions. A major advancement in our Lab-APPES setup is the ability for carrying out photoemission at 1 mbar pressure. The gas manifold is equipped with three mass flow controllers and useful to mix three different gases to a required composition to generate gas mixtures to simulate catalysis reactions. The gas manifold is connected to the gas doser via a z-axis manipulator in the analysis chamber. The capillary of the gas doser inside the analysis chamber can be extended very close to the sample holder. Further, this gas doser can be heated up to 873 K, mainly to heat the input gas for the experiments that are to be carried out at high temperatures. High temperature on the sample surface can be maintained better, when the input gas is also heated to that temperature. This is especially critical at high pressure, where the heat dissipation is expected

to be more due to convection as well as conduction. One of the critical aspects of any high-pressure experiment is the accurate measurement of the pressure near the reaction zone, which is the sample surface. This is achieved using a CTR gauge connected to the analysis chamber through a CF35 flange and extending all the way close to the sample surface (Figure 2.4).This arrangement makes sure that the pressure achieved and reported in our in-situ studies are accurate. Lab-APPES measurements can be complemented by quadrupole mass spectral (QMS) measurements. This is achieved by interconnecting the analysis chamber to the QMS placed in the preparation chamber through a bellow and a leak valve kept close to the QMS. This arrangement allows simultaneous spectral and kinetic measurements, and there is no time lag between them. A similar arrangement is available between the QMS and the first differential pumping of the analyzer stage. This is similar to the previously reported APPES design by Somorjai and co-workers [5] Since the cone of the analyzer is held very close to the sample surface (0.5 mm), the arrangement like this makes sure that the gas analysis is from the outcome of the reactions from the sample surface and not from the residual reactivity from other parts of the chamber. Thus, the setup acts like a sniffer assembly for studying the reactivity of surfaces. Another fine leak capillary, which is connected directly from the analysis chamber to the QMS, can also be used for product analysis and also to compare the results obtained from the first differential pumping stage mass spectral data.

Special sample holders, which can be heated resistively and also using electron bombardment, can withstand the sample temperature up to 2273 K in UHV. Often heating the samples under high-pressure reactive gases (1 mbar) is not practical because of the issues related with the stability of the heating filaments. To overcome this problem, laser heating is employed where the sample surface can be heated up to 1273 K using a near IR laser ($h\nu$ = 920 nm) with 120 W power. The whole assembly is mounted outside on a special optical window where the laser power can be controlled and collimated and allowed to fall on the sample thereby achieving precise heating.

High-resolution Pd 3d core level spectra measured under different O_2 partial pressures at ambient temperature are shown in Figure 2.5a. The same spectra, recorded in fixed or fast data acquisition mode in 1 s, are shown in Figure 2.5b. Only a marginal change in intensity and count rate is observed for high-resolution
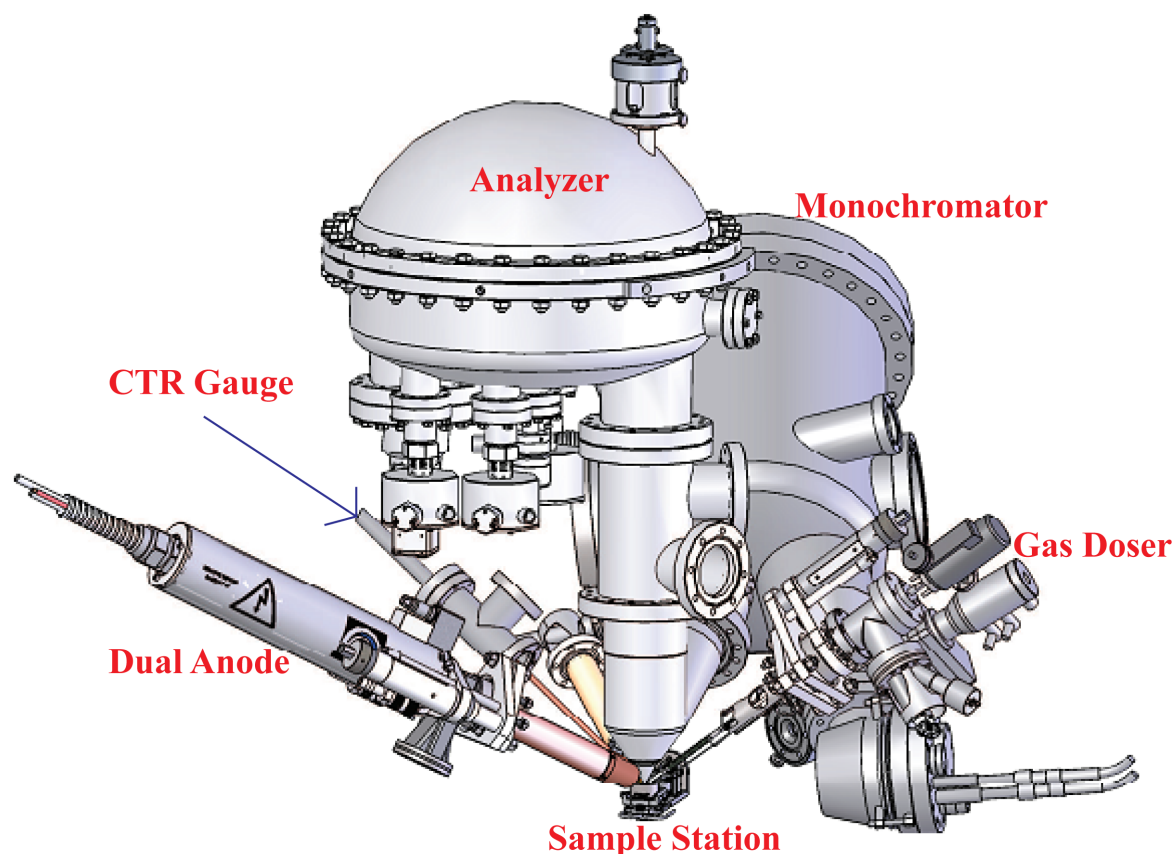
Figure 2.4 A view of the analysis chamber (UV source is not shown).

spectra between UHV and 10^{-2} mbar. However, at 1 mbar the count rate decreases to about 45% of that of UHV conditions. We attribute the above quality results to effective differential pumping in the ELR regime, which minimizes the inelastic scattering. Hardly any change in BE (335 eV for Pd $3d_{5/2}$) is observed, indicating that the Pd remains in the metallic state [6]. Figure 2.5b gives an idea of the quality of data collection possible in 1 s by fixed mode. This is similar to a snapshot recorded for fast movement by high resolution cameras. It is to be noted that the same basic features, such as BE and fwhm, as those at high resolution are very well observed in the 1 s spectra. Although the signal/noise (S/N) is around 6 for a spectrum recorded at 1 mbar, it is higher for the spectrum recorded at lower pressure. This feature demonstrates the possibility of following the reaction dynamics for some of the reactions.
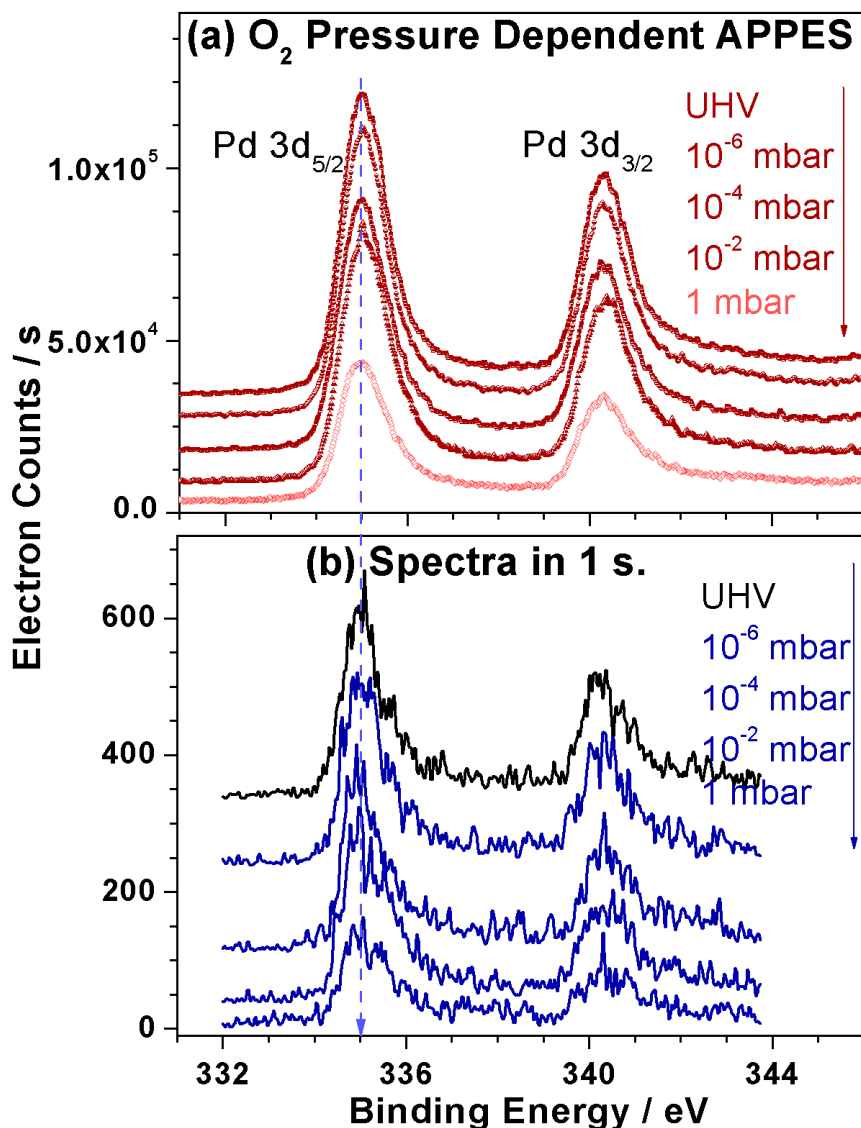
Figure 2.5 Lab-APPES measurements recorded for Pd-foil at ambient temperature for Pd 3d core levels at (a) different O_2 partial pressure and (b) spectra acquired in 1 s at different O_2 partial pressure. The dashed line is a guide to the eye. The 1 s spectra acquired indicate the possibility of measuring transient kinetic aspects and reaction dynamics on catalysts under 1 mbar conditions.

§ 2.3 Results and Discussion

The first set of experiments has been carried out on the interaction of oxygen with polycrystalline coinage metal (group 11) surfaces using APPES and explained in the following section. The knowledge accumulated over the years from studies on clean solid surfaces had great impact on our understanding in areas like corrosion,

catalysis, semiconductor technology, and biomedical sciences [7, 8]. Interaction of oxygen with transition metal surfaces and catalytic oxidation reactions has been an area intensely pursued by surface scientists due to technological and industrial importance. From the perspective of catalysis, the interaction of oxygen with late transition metals, especially Cu, Ag, and Au, has been studied by several surface science techniques for its applications related to methanol synthesis and its oxidation, steam reforming of alcohols, epoxide formation, CO oxidation, and several other industrially important reactions [9]. Systematic surface science studies, here XPS and UPS were employed for studying these three surfaces, were reported by Evans and co-workers as early as 1974 [10]. Thus, initial stages of the oxidation of these metal surfaces, the dynamic evolution of oxide phases on the metal, and the subsurface diffusion of the oxygen and its consequences on surface electronic modification have had a huge impact on the understanding of catalysis phenomena [11]. The recent developments in the APPES have led to revisiting some of the fundamental surface science problems like oxidation of metal surfaces under near ambient conditions. Especially Pd surfaces have been employed, and the results are reported in detail [12].

Many other metal surfaces are yet to be studied by APPES, including Cu, Ag, and Au. In this regard we have carried out the in-situ studies up to 850 K and 1 mbar on the interaction of oxygen with polycrystalline foils of Cu, Ag, and Au using APPES in our laboratory. Specifically, polycrystalline surfaces have been employed, as the surface characteristics are similar to that of catalytically active metal surfaces in supported metal catalysts. Further, this would also bridge the material gap to a significant extent. Au, Ag, and Cu metal foils, obtained from MaTeck GmbH, Germany, were cleaned in the preparation chamber by repeated cycles of Ar^+ sputtering and annealing. The cleanliness was checked by XP spectra. The O_2 gas (99.99%) controlled by flow controller was introduced up to 1 mbar by a variable leak valve. We confirmed that there are no detectable gas impurities by mass spectrometry. XP spectra were measured using monochromatic Al Kα (1486.6 eV) unless otherwise stated. Curve fitting was performed by the software CasaXPS, using asymmetric Lorentzian -Gaussian sum-type line shapes, preceded by a subtraction of the Shirley background. Gas-phase peaks from O_2 under ambient-pressure conditions were observed at 538 eV, and they do not overlap with the peaks from the sample surface. As for the XPS

intensity, it is noted that the intensities taken under different conditions cannot be directly compared because the presence of the ambient pressure gas affects the photoelectron intensity, and therefore the intensity was normalized.

2.3.1 O_2 at 1 mbar on Au Surfaces.

Surface science studies on the adsorption of oxygen on bulk gold surfaces are rarely attempted largely due to the low heat of adsorption of O_2 on Au surfaces [13, 14] One of the earlier works by Madix and coworkers demonstrated this by showing no adsorption under vacuum conditions (10^{-4} Torr) [13]. The adsorption was in turn induced by generating atomic oxygen through a hot platinum filament. The enormous interest that nanogold has generated for various oxidation reactions [15-17] prompted us to reinvestigate the metal surface under APPES. The O 1s and Au 4f core level spectra recorded at 1 mbar and at various temperatures are shown in Figure 2.6. It is very clear from the O 1s spectrum that from room temperature to 600 K and at 1 mbar O_2 the surface showed no evidence for oxygen adsorption. Interestingly, a weak and broad feature started to develop above 600 K which transforms into a solid peak centered around 529.9 eV (arrow in Figure 2.6a). Earlier literature related to XPS studies on the Au oxidation and oxides of gold shows that the O 1s in Au(III) oxide exhibits a BE feature at 530 eV [18-21]. Presumably these features could possibly originate from the oxidation of the under coordinated Au atoms present on the polycrystalline gold foil. O 1s features from gas phase molecular oxygen appear between 538 and 540 eV. Au 4f core level spectra recorded from RT to 850 K in 1 mbar O_2 hardly show any change. The Au $4f_{7/2}$ core level appears at 84.1 eV, a typical BE reported for metallic Au. Indeed, it reiterates the highly inert nature of bulk gold, in spite of surface defects on polycrystalline gold.

2.3.2. O_2 at 1 mbar on Ag Surfaces.

Figure 2.7 shows the Ag 3d core level data collected from Lab-APPES at 1 mbar O_2 at different temperatures on a Ag foil. Indeed, complementary experiments from UHV to 1 mbar at different temperatures have been measured; since the changes observed are from significant to maximum level at 1 mbar, we restrict
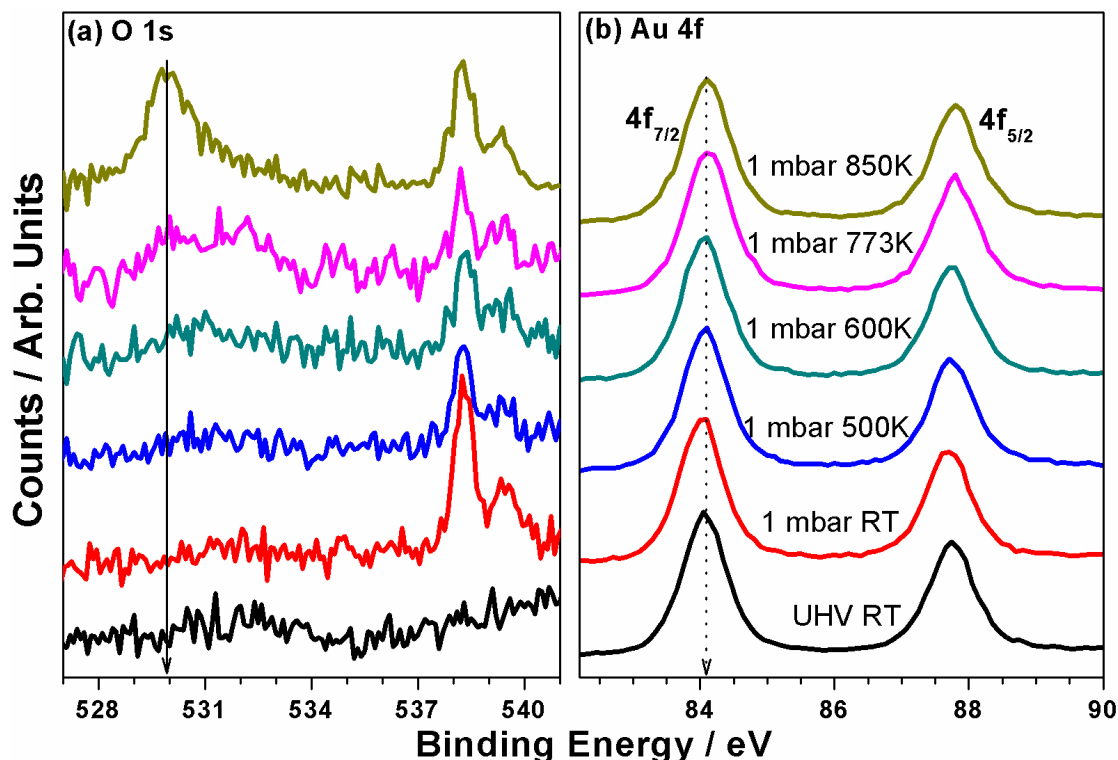
Figure 2.6. Core level spectra measured while exposing 1 mbar of O_2 on a polycrystalline Au foil at various temperatures. (a) O 1s and (b) Au 4f $_{7/2}$. O 1s features from gas phase molecular oxygen appear between 538 and 540 eV. Arrows are a guide to the eye.

our discussion to the same. A sputter-cleaned Ag metal surface under UHV conditions at RT shows the Ag $3d_{5/2}$ peak at 368.0 eV (dashed arrow), which is in agreement with the literature values.[11]. No feature due to common impurities like C, O, or Si was observed, indicating the atomically clean surface nature. After the above measurements, O_2 was allowed in the analysis chamber, and the O_2 partial pressure was increased gradually to 1 mbar. Once the pressure stabilizes at 1 mbar, XPS measurements were carried out at RT and higher temperatures. There are no significant changes observed, either in terms of shift in BE or fwhm of the Ag 3d features at RT. In fact, no O 1s feature was observed as well. The above observations underscore the inert nature of the Ag surface, similar to gold, to O_2 at ambient temperatures. The Ag $3d_{5/2}$ spectrum obtained at various temperatures at 1 mbar O_2 pressure showed an increased broadening and asymmetry on the lower BE side. It is to be noted that the Ag $3d_{5/2}$ peak maximum occurs at the same BE irrespective of 1 mbar oxygen treatment at different temperatures up to 600 K.
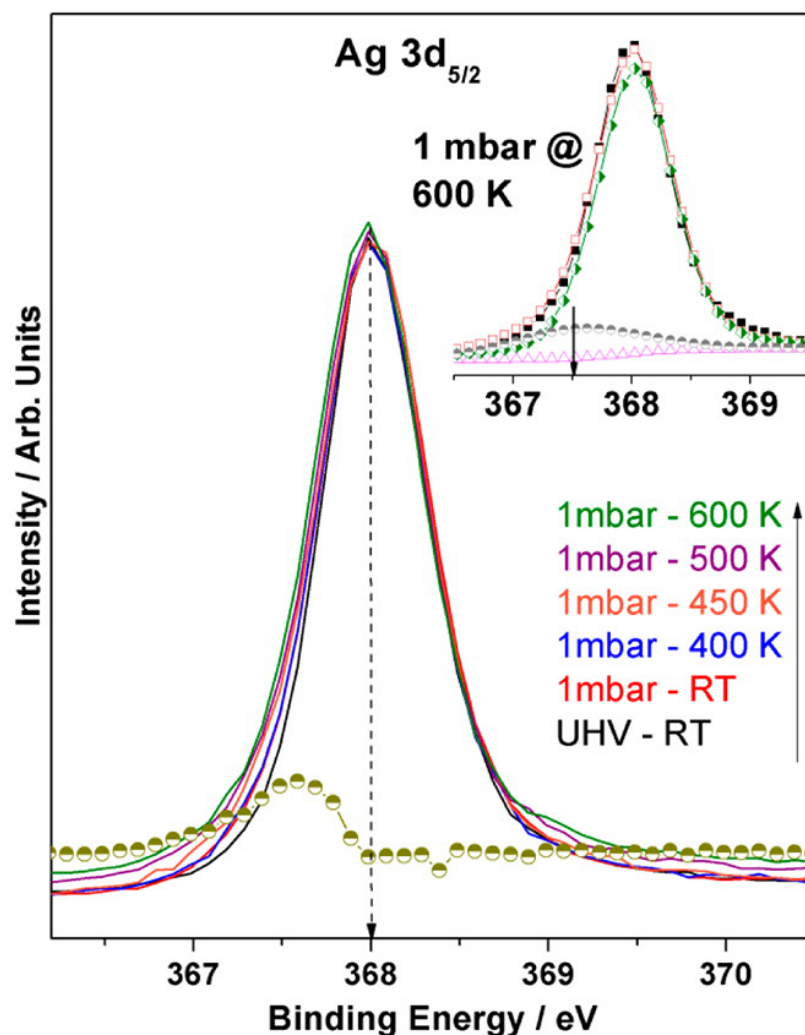
Figure 2.7 Ag $3d_{5/2}$ spectra at 1 mbar O_2 pressure collected at different temperatures. Intensity is normalized to the UHV-RT spectrum. Difference spectra obtained by subtracting UHV-RT from 1 mbar - 600 K is given at the bottom in yellow color demonstrate the presence of the Ag_2O-like feature. Inset shows the deconvolution of Ag $3d_{5/2}$ spectrum measured at 1 mbar O_2 pressure and 600 K. Black and red color are for experimental and sum of the fitted peaks, respectively. Green and gray colors are for metallic Ag and precursor to Ag_2O peaks, respectively. Background subtraction trace is given in pink.

Broadening of the Ag $3d_{5/2}$ peak observed at low BE is due to gradually increasing interaction between the Ag surface and O atoms. Indeed, the difference spectra obtained between 1 mbar - 600 K and UHV-RT spectra show the feature at 367.5 eV due to Ag_2O-like feature. The inset in Figure 2.7 shows the deconvolution of the Ag $3d_{5/2}$ core level recorded at 1 mbar O_2 pressure and at 600 K. The

feature at 367.5 eV is similar to that of Ag_2O. However, the predominant Ag-feature suggests that either the interaction with oxygen is weak or there might be other processes, like migration of atomic oxygen to subsurface layers and/or bulk. Figure 2.8 shows the O 1s spectrum measured at different temperatures and at 1 mbar O_2 pressure on Ag surfaces.
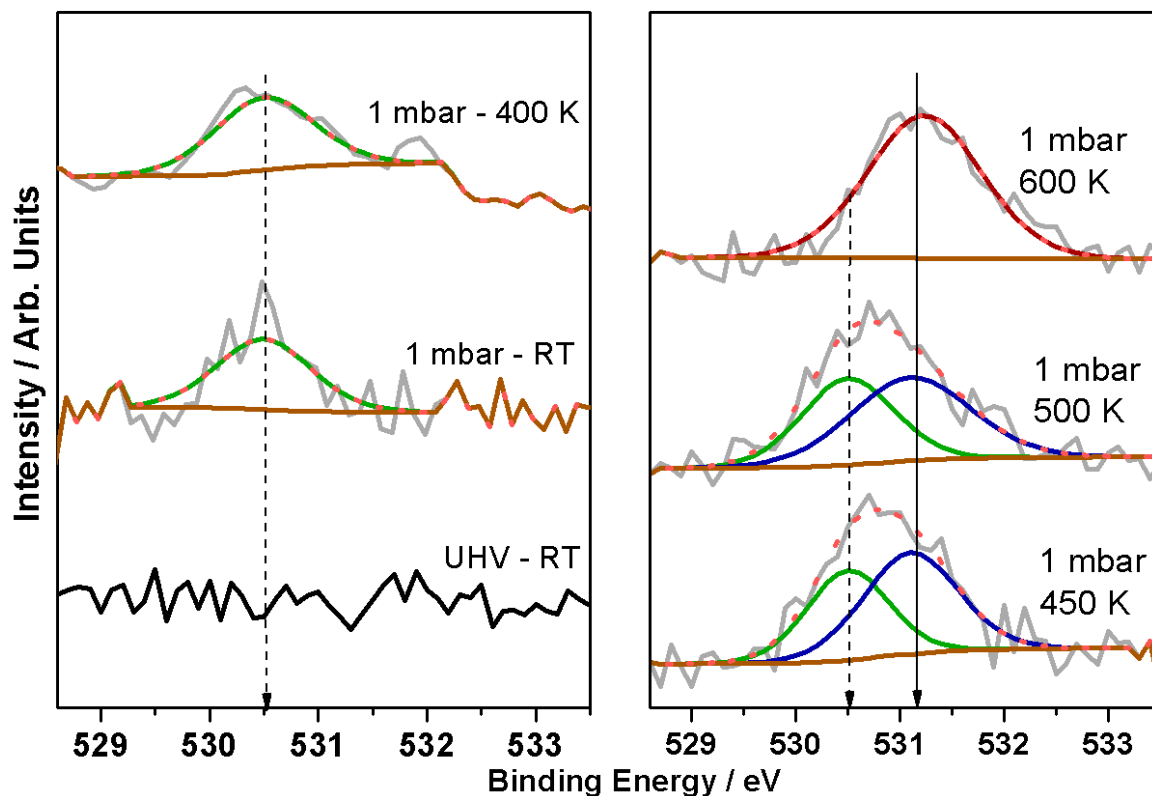
Figure 2.8 O 1s spectra at 1 mbar O_2 pressure collected at different temperatures on Ag foil.

Unlike gold surfaces, silver interacts with oxygen, and it is evident from the results given below. It can be clearly seen that adsorption of O_2 at 1 mbar at 300 K results in the formation of a feature at 530.5 eV (dashed arrow) in the O 1s core level spectrum. The intensity of the 530.5 eV peak increases as the temperature increases to 400 K. An increase in the S/N ratio underscores the oxygen interaction with Ag at increasing temperature. The spectrum recorded at 500 K and 1 mbar O_2 is considerably broader and shifted toward higher BE, indicating the presence of multiple peaks. This spectrum is deconvoluted with two different peaks at BE values of 531.2 eV (solid arrow) and 530.5 eV. Interestingly, the area under the 530.5 eV peak is lower compared to the spectrum obtained

at 400 K, suggesting that the higher BE peak is possibly growing at the expense of this peak. The O 1s spectrum obtained at 600 K is considerably sharper and exhibits only the presence of the feature at 531.2 eV peak. Rocha et al. recently reported a detailed APPES work on the O −Ag system [11], and the feature at 530.5 eV is attributed to O$_\alpha$ species which represents atomic oxygen adsorbed on the Ag surface. The atomic oxygen transforms to oxidic oxygen at 531.2 eV (O$_\beta$) at temperatures above 400 K. This has been assigned by Rocha and co-workers as oxygen in an octahedral site below the Ag surface [11]. A detailed look at the literature suggests that the formation of a more stable oxide on the Ag surface is demonstrated by the appearance of an O 1s peak at 529.6 eV. It is understandable that we did not observe such a stable oxide feature in the present study as the feature, which is denoted in the literature as O$_\gamma$ [22, 23], starts to appear at higher temperatures (773 K). Interestingly, we observe the formation of atomic oxygen on the surface and its transformation to subsurface oxygen, which is considered a precursor to the formation of the bulk oxide. The presence of a considerable amount of defects on the polycrystalline foil also facilitates the diffusion of oxygen into the subsurface in the present case. In spite of the heat treatment at 600 K in 1 mbar O$_2$, polycrystalline Ag seems to be resistive to stable oxide formation, and Ag metal features are dominantly observed. Indeed, this could be the reason for the less significant changes in the Ag 3d feature; however, the low BE feature is attributed to the Ag atoms interacting with the above-mentioned subsurface oxygen which is identified to be the precursor for stable oxides.

It is also to be mentioned here that the electron escape depth is few nanometers in the present analysis, since Al Kα can penetrate deeper at normal incidence angle due to high photon energy (1486.6 eV). However, the KE involved with Ag 3d (~1115 eV) and O 1s (~955 eV) are not too different, and hence the depth of surface layers analyzed can be assumed to be approximately the same in the present communication. Nonetheless, core level analysis using incident photon energy around 410 and 575 eV (in any synchrotron radiation center) for Ag 3d and O 1s, respectively, and/or angle-resolved spectral measurements would give more information on the surface sensitivity aspects. This is especially required if oxidation is limited to top surface layer. A simple calculation [24] mainly based on the KE of Ag 3d and O 1s core levels shows an electron escape depth of about 2.4 nm, suggesting the diffusion of oxygen atoms, at least to that depth.

2.3.3. O$_2$ at 1 mbar on Cu Surfaces.

The surface chemistry of oxygen with Cu is richer compared to Ag and Au because of the much higher reactivity of Cu compared to the other two. Indeed, 3d transition metals are known to be pyrophoric and easily get oxidized even at ambient temperature. The Cu 2p and Cu LMM Auger spectra obtained in the presence 1 mbar of O$_2$ from RT to 675 K are shown in Figures 2.9a and 2.9b, respectively.

The Cu 2p spectrum from a clean Cu surface obtained under UHV conditions and at RT immediately after Ar$^+$ sputtering and annealing is shown for reference (Figure 2.9a). The Cu 2p$_{3/2}$ core level spectrum centered at 932.8 eV (gray solid arrow) which is characteristic of metallic Cu remains unchanged until 425 K, indicating that the metallic nature of Cu surface is retained until this temperature. The spectrum obtained at 500 K is clearly distinct from the one at 425 K by the shift in the peak maximum toward the lower BE side. The peak maximum in this case is at 932.4 eV (dashed arrow), which is characteristic of Cu(I) in the XPS literature [25, 26]. However, it is to be noted that only from the core level shift in BE it is difficult to ascertain the change in oxidation state, and Auger spectral measurements are also necessary to confirm the change in oxidation state, especially on Cu-based materials. This aspect will be discussed later. The characteristics of the peak at 932.4 eV remain the same until 600 K, indicating the stability of the Cu(I) species on the surface. Onset of oxidation of Cu$_2$O to CuO occurs between 500 and 600 K, and it is fully oxidized to CuO >600 K; it is evident from the observation of the following new features: (a) The high BE feature at 933.5 eV (dotted arrow) suggests typical Cu^{2+} species and indicates the coexistence of Cu$^+$ and Cu^{2+} species at 600 K. Deconvolution of the Cu 2p$_{3/2}$ feature demonstrates the coexistence of Cu(I) and Cu(II) species at 600 K. (b) Evidence for the presence of CuO also comes from the well-developed Cu^{2+} satellite between 939 and 945 eV, corresponding to the Cu 2p^{5}3d^9 final state configuration [26] from 600 K and above. (c) Cu 2p spectra at 625 and 675 K are broad (fwhm = 3.6 eV), exhibiting the presence of exclusive bulk CuO.
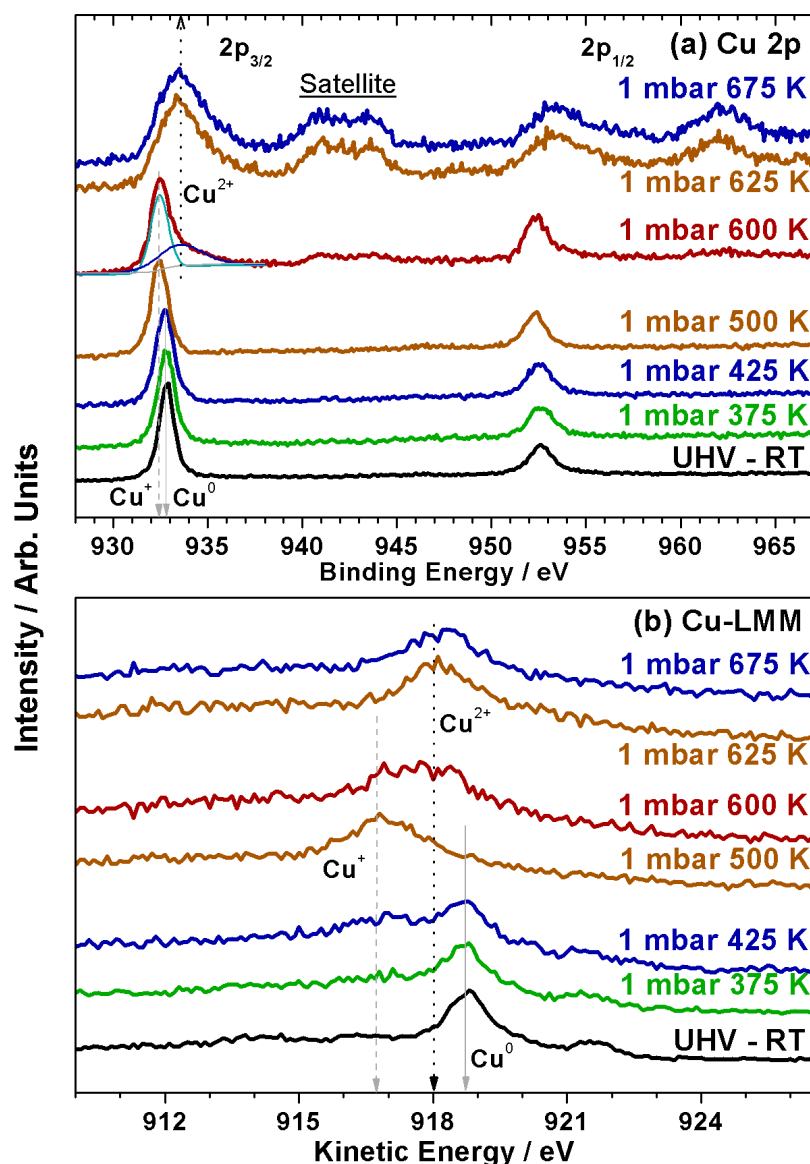
Figure 2.9 Core level spectra measured while exposing a polycrystalline Cu foil to 1 mbar of O_2 at various temperatures: (a) Cu 2p and (b) Cu LMM.

No feature due to Cu_2O or Cu was observed at higher temperatures demonstrating the onset of bulk oxidation of Cu to CuO. (d) Charge transfer (Δ) from the oxygen ligand to Cu^{2+} occurs, leading to a Cu $3d^{10}$ - O $2p^5$ configuration in the initial (ground) state [26, 27]. Indeed, this configuration is at higher energy due to charge transfer, compared to the Cu $3d^9$ - O $2p^6$ initial state. However, on photoelectron emission from the Cu 2p core level, energy reversal occurs in the final state due to better shielding of core hole in Cu $2p^5 3d^{10}$ compared to Cu $2p^5 3d^9$, and this leads to the main line at 934 eV and satellites between 939 and 945 eV, respectively [27, 28].

Above energy reversal occurs due to attractive energy between Cu 2p core hole and valence electron in 3d, and the same is denoted as Q. Indeed, the satellite feature is unique for the $3d^9$ configuration and observed easily. Energies associated with different configurations in the ground state and final states are shown schematically in Figure 2.10 for illustration.
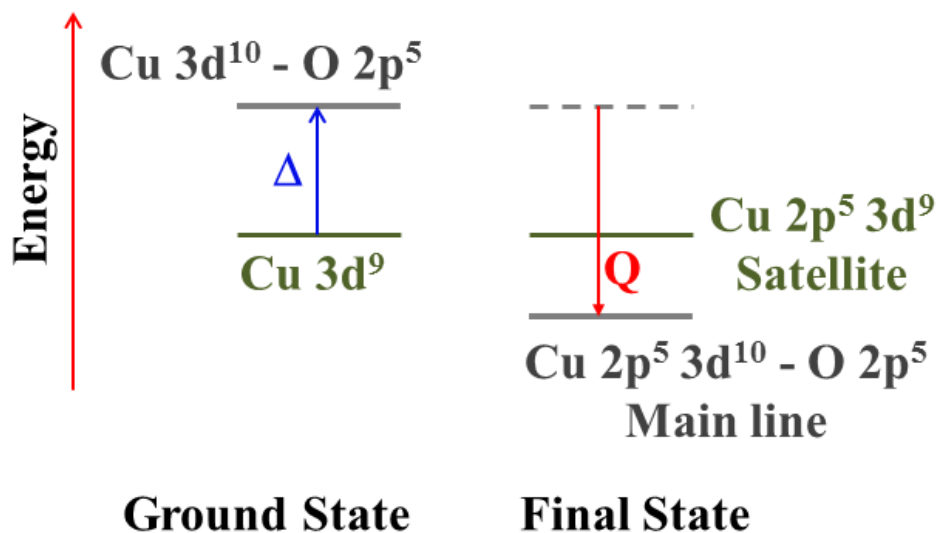
Figure 2.10 Schematic energy level to show charge transfer (Δ) in the ground state and energy reversal in the final state configuration (due to Q), corresponding to main line. Energy of satellite feature due to Cu $3d^9$ configuration is relatively unaffected due to photoelectron emission.

It is well-known that the different oxide phases of Cu are better discernible in the LMM Auger spectrum of Cu. The X-ray initiated Auger spectrum obtained at different temperatures at 1 mbar oxygen pressure is shown in Figure 2.9b. The UHV RT spectrum shows the characteristic Cu LMM Auger peak at 918.9 eV for clean Cu metal (gray arrow). In addition to the above metallic Cu feature, a new peak starts to emerge at 916.1 eV from 375 K onward, indicating the growth of the Cu(I) phase (dashed arrow) on the surface. Upon increasing the temperature up to 500 K, the Cu(I) oxide phase at 916.7 eV increases at the expense of metallic Cu. On further increasing the temperature to 500 K, the fully developed Cu_2O feature is observed at 916.8 eV at the expense of the metallic Cu feature. This indicates the complete surface oxidation of Cu to Cu_2O at 500 K and 1 mbar of O_2.

In fact, the above complete oxidation to Cu_2O was observed better with Auger spectral changes than with Cu 2p core level changes. On increasing the temperature to 600 K, the spectrum becomes broad, indicating the formation of a third type of species, Cu^{2+}, on the surface. The Cu^{2+} LMM Auger peak at 918.1 eV (dotted arrow) obtained in the present case is in agreement with several literature reports [25-28]. The growth of Cu^{2+} is much more evident in the 625 and 675 K spectra where the peak maximum is centered around 918 eV. Oxidation of Cu_2O to CuO is equally evident from Cu 2p core level and Auger spectral changes, and they are in agreement with each other. Indeed, different KEs observed for different oxidation states lead to different Auger parameter values, and this reiterates the changes in oxidation state [28].

O 1s spectra acquired at different temperatures and at 1 mbar pressure are shown in Figure 2.11. An increase in temperature to 375 K at 1 mbar O_2 pressure is accompanied by a broad peak centered at 530.4 eV (dotted arrow). The feature at 530.4 eV in the O 1s spectrum is attributed to oxygen in Cu_2O [29]. Along with the predominant 530.4 eV feature, the presence of a 532 eV species is observed in both the 375 and the 425 K spectra. The O 1s feature at 532 eV has been attributed to OH species in the past, but it could also be attributed to oxygen bound to residual impurities on the Cu surface [30]. The O 1s feature at 530.4 eV grows in intensity, and other features disappear on increasing the temperature from 375 to 500 K. The O 1s spectrum at 500 K is mostly dominated by oxygen from Cu_2O species with the emergence of a new feature at 529.6 eV (dashed arrow). This feature is characteristic of CuO surfaces. Nonetheless, the spectrum measured at 600 K is dominated by 529.6 eV species, at the expense of Cu_2O, and demonstrates the oxidation of the Cu(I) to the Cu(II) state on the surface. Interestingly, we could find the presence of another species at around 531.3 eV, which is attributed to the suboxide species [30, 32]. The suboxide species is only stable under oxygen pressure and decomposes once the high-pressure regime is reverted to UHV. Oxygen from Cu_2O at 530.4 eV completely disappears >600 K, indicating the complete oxidation of the surface layers to CuO.
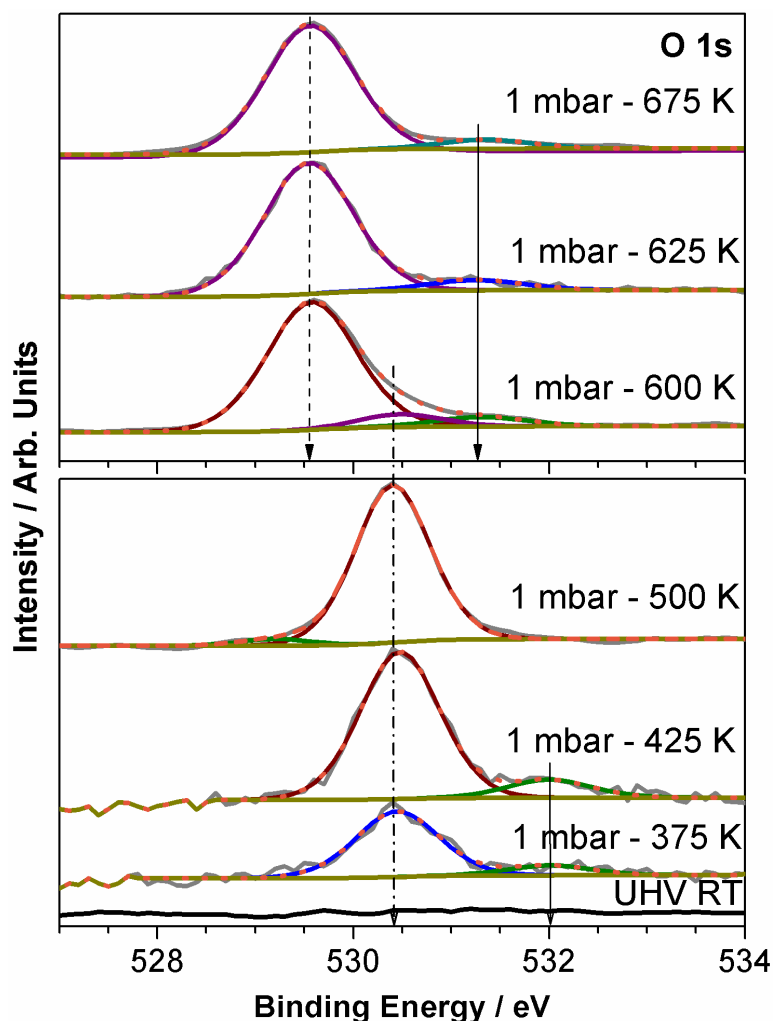
Figure 2.11 O 1s core level spectra measured while exposing a Cu foil to 1 mbar O_2 at various temperatures. O 1s spectra were deconvoluted to show the systematic changes from Cu metal to CuO through Cu_2O.

Changes observed in the core level XPS reflect very well in the valence band (VB) spectra of Cu surfaces (Figure 2.12) at 1 mbar O_2 pressure at different temperatures. UHV-RT spectra show the $3d^{10}$ feature of Cu-metal surfaces. Onset of a new feature at 1.4 eV (dashed arrow) is observed on O_2 treatment at 375 K. This particular feature grows in intensity up to 500 K, and then it decreases. This feature is attributed to the Cu_2O formation on the surface. A characteristic narrowing of the 3d band at 3.2 eV occurs at 500 K, compared to the spectra recorded at lower temperatures; it is attributed to the complete oxidation of Cu^0 to Cu_2O [26]. By utilizing the photoionization cross-section values, it is easy to identify the origin of peaks from the regions of O 2p or Cu 3d by spectral weight. The photoionization cross section (σ) of O 2p and Cu 3d is 2.4 × 10^{-4} and 1.2 ×

10^{-2} Mb, respectively, at $h\nu = 1486.6$ eV [33] Indeed, the Cu 3d spectral weight is primarily observed in the VB for both Cu_2O and CuO, and it is fully supported by the larger σ of Cu 3d, by 1.5 orders of magnitude. A weak and broad feature observed between 5 and 8 eV is due to O 2p derived spectral features, and it is observed at 500 K. This underscores the ~3.5 eV energy gap between the peak maximum of Cu 3d and O 2p derived features for Cu_2O due to weak hybridization between fully filled Cu $3d^{10}$ and O $2p^6$ orbitals. Indeed, our results are in excellent agreement with those reported by Ghijsen et al. [27].
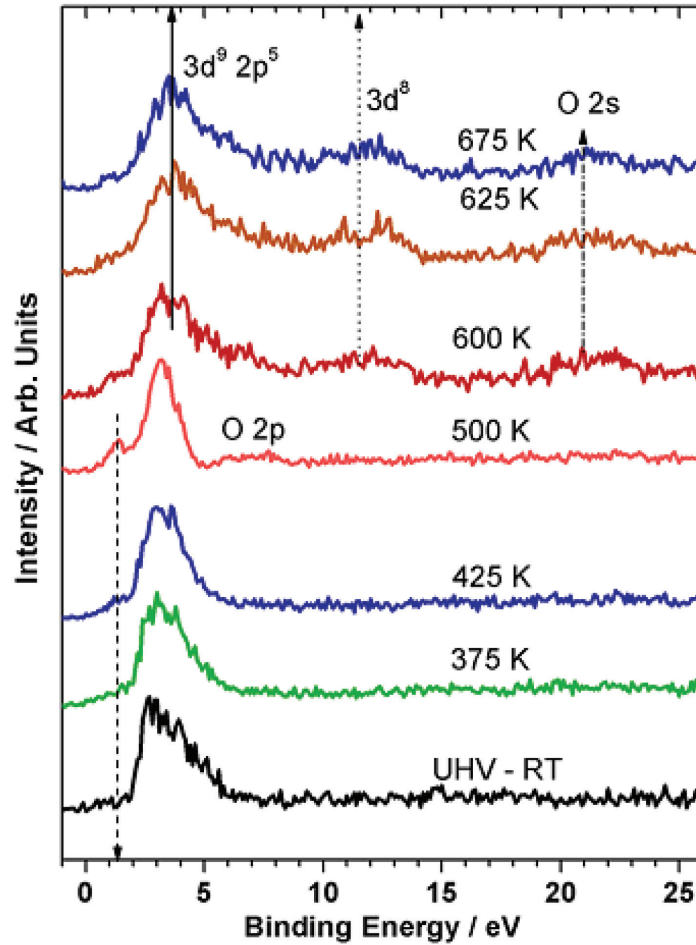
Figure 2.12 High-pressure valence band spectra recorded at 1 mbar of O_2 and at different temperatures. Systematic conversion of Cu metal at UHV-RT to Cu_2O (at 500 K) and CuO above 500 K is observed in 1 mbar of O_2.

A major change occurs in the VB spectrum on further increasing the temperature to 600 K; the VB broadens between 1 and 13.5 eV, and the same features are observed at higher temperatures up to 675 K. The typical feature for Cu_2O at 1.4 eV decreases in intensity ≥600 K. Further, a broad feature is observed

between 8 and 12.5 eV (dotted arrow). Indeed, this feature is characteristic for CuO and attributed to a satellite due to the $3d^8$ final state configuration. Photoionization of the $3d^9$ ground state configuration leads to the above satellite. This feature is very similar to the high BE satellite observed for CuO in core level XPS. A high BE shoulder is observed between 4 and 8 eV with the main VB peak at 3.5 eV (solid arrow) at 600 K and above. The above broad feature is attributed to the strong hybridization of Cu and O in CuO, which is typical for cuprates [34] In comparison to the energy gap (∼3.5 eV) observed between O 2p and Cu 3d derived spectral weights in the VB spectra recorded between 375 and 500 K, the overlapping shoulder with the main VB at ≥600 K demonstrates the formation of CuO due to strong hybridization. A feature observed at 21 eV (dash-dotted arrow) is attributed to the O 2s shallow core level.

§ 2.4 Conclusions

Special features available with Lab-APPES have been described in detail. Especially, a better vacuum is maintained in the electrostatic lens column under 1 mbar pressure conditions in the analysis chamber, and the aperture free lens regime provides better quality data collection with simple laboratory X-ray sources. Using Lab-APPES at 1 mbar oxygen pressure, various stages of silver, copper, and gold oxidation have been probed. With Lab-APPES available at NCL, Pune, it is possible to simulate the catalysis reaction conditions on solid surfaces, in terms of pressure up to 1 mbar and temperatures, at least, up to 1273 K.

§ 2.5 References

[1]. (a) H. Bluhm, *J. Electron Spectrosc. Relat. Phenom.* **2010**, *177*, 71-84. (b) D. E. Starr, Z. Liu, M. Haevecker, A. Knop-Gericke, H. Bluhm, *Chem. Soc. Rev.* **2013**, *42*, 5833-5857. (c) A. Shavorskiy, H. Bluhm, in *Heterogeneous Catalysts for Clean Technology*, Wiley-VCH Verlag GmbH & Co. KGaA, **2013**, pp. 437-468.

[2]. M. Salmeron, R. Schlögl, *Surf. Sci. Rep.* **2008**, 63, 169 −199 and references therein.

[3]. F. Mangolini, J. Åhlund, G. E. Wabiszewski, V. P. Adiga, P. Egberts, F. Streller, K. Backlund, P. G. Karlsson, B. Wannberg, R. W. Carpick, *Rev. Sci. Instrum.* **2012**, 83, 093112.

[4]. A. Kolmakov, D. A. Dikin, L. J. Cote, J. Huang, M. K. Abyaneh, M. Amati, L. Gregoratti, S. Guenther, M. Kiskinova, *Nat. Nanotechnol.* **2011**, *6*, 651-657.

[5]. F. Tao, S. Dag, L.-W. Wang, Z. Liu, D. R. Butcher, H. Bluhm, M. Salmeron, G. A. Somorjai, *Science* **2010**, *327*, 850-853.

[6]. (a) N. Maity, P. R. Rajamohanan, S. Ganapathy, C. S. Gopinath, S. Bhaduri, G. K. Lahiri, *J. Phys. Chem. C* **2008**, *112*, 9428-9433. (b) C. Murali, M. S. Shashidhar, C. S. Gopinath, *Tetrahedron* **2007**, *63*, 4149-4155.

[7]. (a) J. G. Ekerdt, Y. M. Sun, A. Szabo, G. J. Szulczewski, J. M. White, *Chem. Rev.* **1996**, *96*, 1499-1517 (b) J. H. Sinfelt, *Surf. Sci.* **2002**, *500*, 923-946. (c) F. Zaera, C. S. Gopinath, *J. Mol. Catal. A: Chem.* **2001**, *167*, 23-31.

[8]. (a) P. D'Orazio, *Clin.* Chim. *Acta* **2003**, *334*, 41-69. (b) V. Bustos, C. S. Gopinath, R. Unac, F. Zaera, G. Zgrablich, *J. Chem. Phys.* **2001**, *114*, 10927-10931.

[9]. (a) J. M. C. Soares, P. Morrall, A. Crossley, P. Harris, M. Bowker, *J. Catal.* **2003**, *219*, 17-24. (b) M. Bowker, R. A. Bennett, S. Poulston, P. Stone, *Catal. Lett.* **1998**, *56*, 77-83. (c) K. C. Waugh, *Catal. Today* **1992**, *15*, 51-75. (d) M. Bowker, *Top. Catal.* **1996**, *3*, 461-468. (e) A. Klust, R. J. Madix, *Surf. Sci.* **2006**, *600*, 5025-5040. (f) C. Ruggiero, P. Hollins, *J. Chem. Soc., Faraday Trans.* **1996**, *92*, 4829-4834. (g) K. Thirunavukkarasu, K. Thirumoorthy, J. Libuda, C. S. Gopinath, *J. Phys. Chem. B* **2005**, *109*, 13283-13290. (h) T. Mathew, K. Sivaranjani, E. S. Gnanakumar, Y. Yamada, T. Kobayashi, C. S. Gopinath, *J. Mater. Chem.* **2012**, *22*, 13484-13493.

[10]. S. Evans, E. L. Evans, D. E. Parry, M. J. Tricker, M. J. Walters, J. M. Thomas, *Faraday Discuss. Chem. Soc.* **1974**, 58, 97 -105.

[11]. T. C. R. Rocha, A. Oestereich, D. V. Demidov, M. Haevecker, S. Zafeiratos, G. Weinberg, V. I. Bukhtiyarov, A. Knop-Gericke, R. Schloegl, *Phys. Chem. Chem. Phys.* **2012**, *14*, 4554-4564.

[12]. R. Toyoshima, M. Yoshida, Y. Monya, Y. Kousa, K. Suzuki, H. Abe, B.

S. Mun, K. Mase, K. Amemiya, H. Kondoh, *J. Phys. Chem. C* **2012**, *116*, 18691-18697.

[13]. N. D. S. Canning, D. Outka, R. J. Madix, *Surf. Sci.* **1984**, *141*, 240-254.

[14]. C. P. Vinod, J. W. Niemantsverdriet, B. E. Nieuwenhuys, *Appl. Catal., A* **2005**, *291*, 93-97.

[15]. (a) M. Haruta, *CATTECH* 2002, *6*, 102-115. (b) A. S. K. Hashmi, G. J. Hutchings, *Angewandte Chemie International Edition* **2006**, *45*, 7896-7936.

[16]. A. C. Sunil Sekhar, K. Sivaranjani, C. S. Gopinath, C. P. Vinod, *Catal. Today* **2012**, *198*, 92-97.

[17]. P. Jiang, S. Porsgaard, F. Borondics, M. Kober, A. Caballero, H. Bluhm, F. Besenbacher, M. Salmeron, *J. Am. Chem. Soc.* **2010**, *132*, 2858-2859.

[18]. (a) B. Koslowski, H. G. Boyen, C. Wilderotter, G. Kastle, P. Ziemann, R. Wahrenberg, P. Oelhafen, *Surf. Sci.* **2001**, *475*, 1-10. (b) C. S. Gopinath, R. Muthukumaran, L. L. Welling, M. A. Bennett, P. T. Manoharan, *Chem. Phys. Lett.* **1998**, *296*, 566-570.

[19]. A.Krozer, M. Rodahl, *J. Vac.* Sci*. Technol., A* **1997**, *15*, 1704-1709.

[20]. J. J. Pireaux, M. Liehr, P. A. Thiry, J. P. Delrue, R. Caudano, *Surf. Sci.* **1984**, *141*, 221-232.

[21]. A. R. Aita, N. C. Tran, *J. Vac.* Sci*. Technol., A* **1991**, *9*, 1498-1500.

[22]. X. Bao, M. Muhler, T. Schedel-Niedrig, R. Schlögl, *Phys. Rev. B: Condens. Matter* **1996**, *54*, 2249-2262.

[23]. T. Schedel-Niedrig, X. Bao, M. Muhler, R. Schlogl, *Ber. Bunsen-Ges.* **1997**, *101*, 994-1006.

[24]. S. Tanuma, C. J. Powell, D. R. Penn, *Surf. Interface Anal.* **1993**, *20*, 77-89.

[25]. (a) M. Vijayaraj, C. S. Gopinath, *J. Catal.* **2006**, *241*, 83-95. (b) T. Mathew, N. R. Shiju, K. Sreekumar, B. S. Rao, C. S. Gopinath, *J. Catal.* **2002**, *210*, 405-417.

[26]. (a) C. S. Gopinath, *J. Chem.* Soc*., Faraday Trans.* **1996**, *92*, 3605-3610. (b) T. Mathew, B. S. Rao, C. S. Gopinath, *J. Catal.* **2004**, *222*, 107-116. (c) T. Mathew, S. Shylesh, B. M. Devassy, M. Vijayaraj, C. V. V. Satyanarayana, B. S. Rao, C. S. Gopinath, *Appl. Catal., A* **2004**, *273*, 35-45.

[27]. (a) J. Ghijsen, L. H. Tjeng, H. Eskes, G. A. Sawatzky, R. L. Johnson, *Phys. Rev. B: Condens. Matter* **1990**, *42*, 2268-2274. (b) J. Ghijsen, L. H. Tjeng, J. Van Elp, H. Eskes, J. Westerink, G. A. Sawatzky, M. T. Czyzyk, *Phys. Rev. B: Condens. Matter* **1988**, *38*, 11322-11330.

[28]. S. Poulston, P. M. Parlett, P. Stone, M. Bowker, *Surf. Interface Anal.* **1996**, *24*, 811-820.

[29]. (a) C. N. R. Rao, D. D. Sarma, M. S. Hegde, *Proc. R. Soc. London, Ser. A* **1980**, *370*, 269-280. (b) R. van Wijk, P. C. Görts, A. J. M. Mens, O. L. J. Gijzeman, F. H. P. M. Habraken, J. W. Geus, *Appl. Surf. Sci.* **1995**, *90*, 261-269. (c) J. P. Tobin, W. Hirschwald, J. Cunningham, *Appl. Surf. Sci.* **1983**, *16*, 441-452.

[30]. H. Bluhm, M. Hävecker, A. Knop-Gericke, E. Kleimenov, R. Schlögl, D. Teschner, V. I. Bukhtiyarov, D. F. Ogletree, M. Salmeron, *J. Phys. Chem. B* **2004**, *108*, 14340-14347.

[31]. C.-t. Au, J. Breza, M. W. Roberts, *Chemical Physics Letters* **1979**, *66*, 340-343.

[32]. V. I. Bukhtiyarov, V. V. Kaichev, E. A. Podgornov, I. P. Prosvirin, *Catal. Lett.* **1999**, *57*, 233-239.

[33]. J. J. Yeh, I. Lindau, *At. Data Nucl. Data Tables* **1985**, *32*, 1-155.

[34]. (a) A. S. Reddy, C. S. Gopinath, S. Chilukuri, *J. Catal.* **2006**, *243*, 278-291. (b) C. S. Gopinath, S. Subramanian, P. S. Prabhu, M. S. R. Rao, G. V. S. Rao, *Physica C* **1993**, *218*, 117-129.(c) S. Velu, K. Suzuki, C. S. Gopinath, H. Yoshida, T. Hattori, *Phys. Chem. Chem. Phys.* **2002**, *4*, 1990-1999.

Chapter 3

UV Photoelectron Spectroscopy at Near Ambient Pressures: Mapping Valence Band Electronic Structure Changes
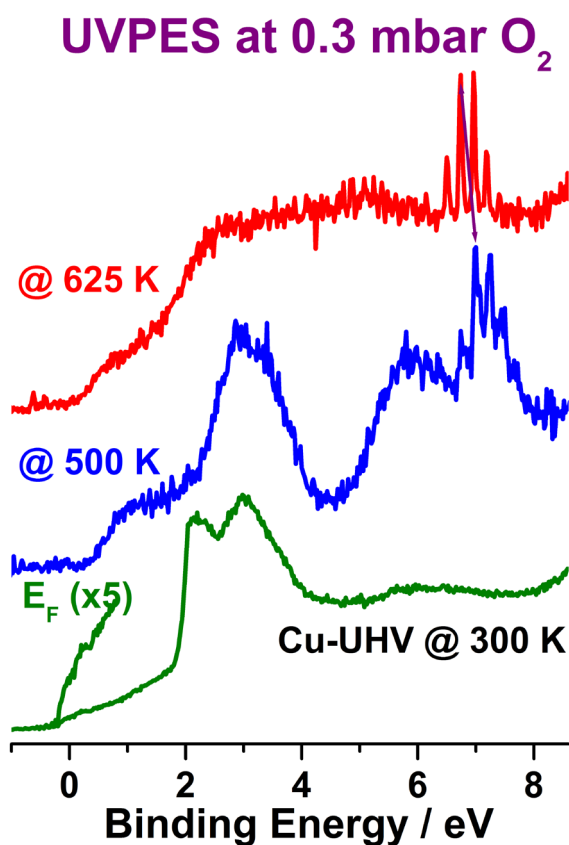
Part of the work presented in this chapter has been published, and the publication detail is :

Kanak Roy, Chinnakonda S. Gopinath, UV Photoelectron Spectroscopy at Near Ambient Pressures: Mapping Valence Band Electronic Structure Changes from Cu to CuO, *Anal. Chem.* **2014**, 86(8), 3683–3687.

Valence band (VB) changes and hence electronic structure evolution was directly observed with low kinetic energy (KE) electrons at near ambient pressure (NAP) conditions with He I photon source in a custom built Lab-APPES. Polycrystalline Cu surfaces were gradually oxidized in O_2 to Cu_2O, to a mixture of Cu_2O + CuO, and finally to CuO between 300 and 625 K and at NAP. Typical VB features for Cu, Cu_2O, and CuO were observed, and the results corroborate well with core level and Auger spectral changes. High mean free path associated with low KE electrons, very low or no inelastic scattering, and effective pumping and the design of electrostatic lens regime help to minimize the electron attenuation at NAP conditions. The present results extend the capabilities of the APPES tool to explore the in situ evolution of electronic structure of materials at NAP and high temperatures.

§ 3.1 Introduction

Photoelectron spectroscopy (PES) is the direct experimental technique available to explore the valence band (VB) electronic structure (VBES) of solids and molecules directly and without any assumptions. VBES analysis provides a wealth of information about the chemical bonding, hybridization and energy of different orbitals/bands, Fermi level (E_F) information, etc. However, conventional PES works under ultra-high vacuum ($\sim 10^{-10}$ mbar), and hence, the changes that occur under working conditions of materials (or closer to that), such as in catalysis and electrochemistry, cannot be explored by PES. Recent advances in the ambient pressure photoelectron spectroscopy (APPES) are of immense help to remove the above obstacle, and PES under near ambient pressures became possible [1]. In fact, there is a sudden surge in reports in this area, especially in the area of heterogeneous catalysis since it is fully relevant [2, 3]. Nonetheless, the extent of inelastic scattering of photoelectrons increases at near ambient pressure (NAP). Inelastic scattering depends on the inelastic mean free path (λ) and the kinetic energy (KE) of the electrons before it reaches a significant vacuum of $\leq 10^{-2}$ mbar in the electrostatic lens column. Under the above conditions, high KE electrons ($>$100 eV) can survive the near ambient pressures ($0.1 - 10$ mbar) due to $\lambda \approx$ few mm, and hence, PES is possible with $h\nu \geq 100$ eV [1]. Low KE electrons ($<$100 eV) were expected to attenuate even severely and, in fact, there are no reports on the VBES analysis of solid surfaces with low energy photons at NAP conditions.

In contrast to the above facts and expectations, we demonstrate here the VBES mapping with low photon energy, He I ($h\nu = 21.2$ eV), and hence low KE electrons ($5-16$ eV) at NAP, up to 0.3 mbar. To the best of our knowledge, there are no such reports available in the literature to demonstrate the VB analysis of solid surfaces at NAP ($\geq$0.01 mbar) conditions.

§ 3.2 Experimental Section

All the experiments were carried out in a custom built laboratory ambient pressure photoelectron spectrometer (Lab-APPES) unit installed recently in our laboratory at CSIR-NCL, Pune. Design and performance aspects of the above Lab-APPES unit, and oxidation of Cu, Ag, and Au surfaces with O_2 under 1

mbar and temperatures up to 773 K was demonstrated through Lab-APPES and is discussed in Chapter 2. In the following, we describe the VBES changes observed with polycrystalline Cu foil up to 0.3 mbar O_2 pressure and 625 K. VB spectra were recorded with conventional He I and Al Kα X-ray photon sources. VB changes observed due to oxidation are corroborated with core level changes in the oxidation state of Cu. It is to be noted that low energy photons offer the best possible resolution. Photoionization cross section (σ) of VB and core levels depends on the incident photon energy [4] and this is an extra handle to confirm the origin of different VB features.

§ 3.3 Results and Discussion

VB spectra of Cu surfaces were recorded as a function of O_2 partial pressure and temperature, and the critical results are shown in Figure 3.1. The clean Cu surface shows the typical 3d VB features between binding energy (BE) = 1.8 and 4.2 eV with distinct E_F [5]. An increase in O_2 pressure up to 0.01 mbar at 300 K did not show significant changes. The E_F feature with comparable intensity as that of Cu-UHV-300 K was observed. A further increase in O_2 pressure begins to broaden the VB features. O_2 vibrational features begin to be observed at ≥0.1 mbar O_2 pressure, and it was confirmed by control experiments with gas phase O_2 PES. At 0.3 mbar, a broad Cu 3d feature between 2 and 4 eV was observed with a low intensity, broad, and featureless peak between 4 and 7 eV, due to chemisorbed oxygen. Secondary electrons increase at BE ≥ 10 eV, and hence, background intensity also increases.

On increasing the temperature gradually to 725 K at 0.3 mbar O_2 pressure (see wine red trace in Figure 3.1 and Figure 3.2), a complete oxidation of Cu_2O was observed; indeed, Cu to Cu_2O oxidation is complete at 500 K. E_F features disappear completely, and a characteristic narrowing of Cu 3d band was observed at 600 K (Figure 3.1). A new feature at 1.3 eV develops, which is also very characteristic of Cu_2O [6]. O 2p features between 4 and 7 eV at 300 K changes into a fully developed feature at 6 eV at ≥373 K. The above observations were corroborated with changes in Cu 2p core level, X-ray excited Auger electron spectra (XAES), and VB spectra recorded with Al Kα (vide infra, Figure 3.3). Due to hybridization of O 2p with Cu 4s and 4p orbitals in Cu_2O, there is a large

energy gap between the fully filled Cu $3d^{10}$ (3 eV) and O 2p (6 eV) was observed as a valley.
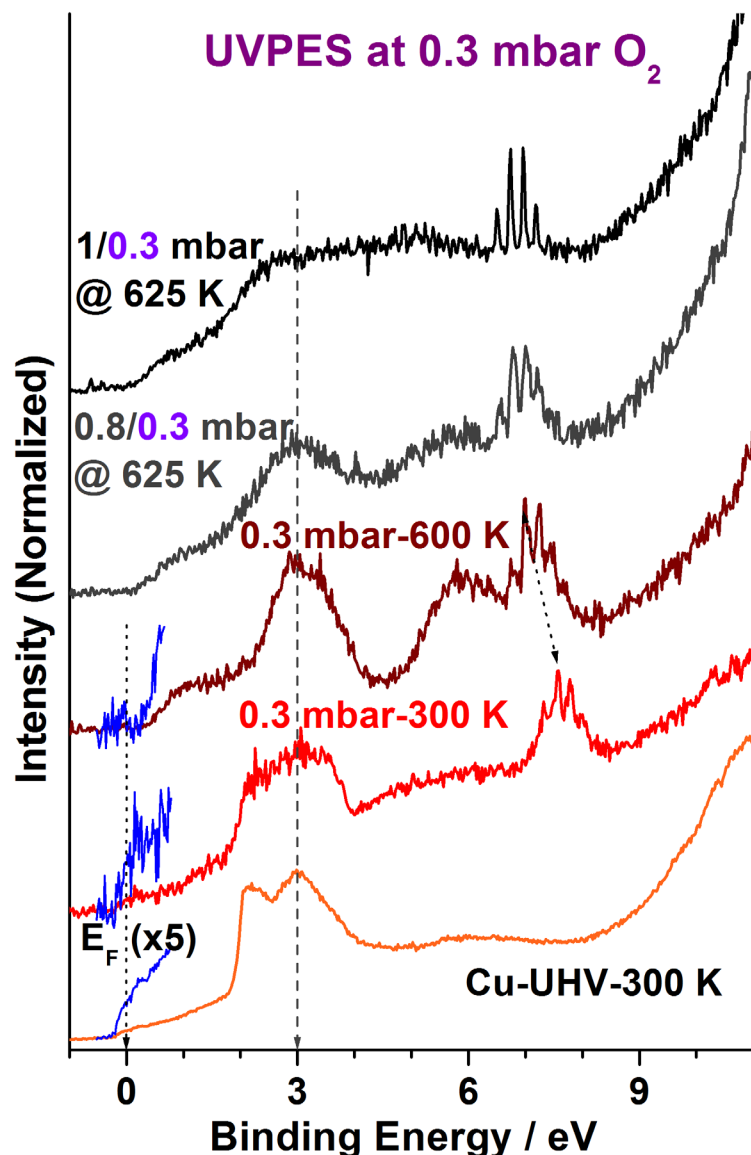
Figure 3.1 Valence band photoelectron spectra recorded with He I photons on Cu surface at different temperatures and up to 0.3 mbar O_2 pressure. All the spectra were normalized at BE = 3 eV (dashed line). Top two VB spectra, given in gray and black color, were recorded at 625 K and 0.3 mbar O_2 pressure but oxidized at 0.8 and 1 mbar O_2, respectively, prior to VB measurements.

Vibrational features of molecular O_2 overlap with the O 2p features at 6.7 − 8 eV. Further, BE of vibrational features of molecular O_2 shifts by 0.6 eV on Cu_2O compared to metallic Cu, and the shift is indicated by a dotted arrow; this shift is attributed to the change in work function of metallic Cu to Cu_2O semiconductor

[2a]. This also underscores that gas phase O_2 signatures are strongly influenced by the surface work function, and hence, it should be very close to the surface. This critical observation fully confirms the presence of O_2 at indicated pressures and the *in situ* nature of the experiments.
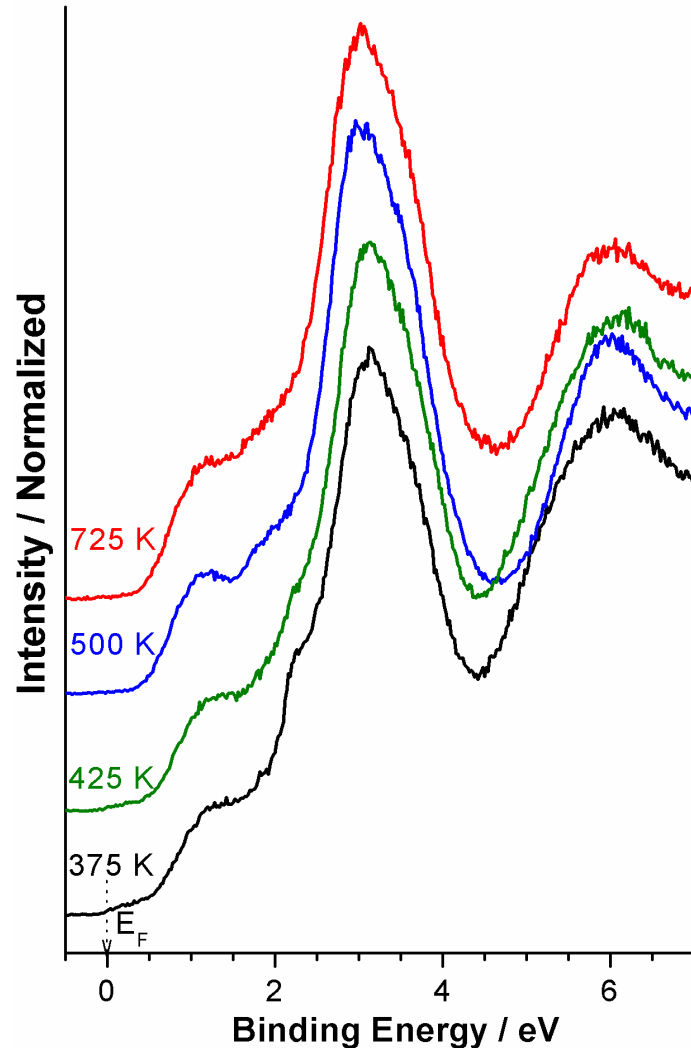
Figure 3.2: Valence band photoelectron spectra recorded with He I photons as excitation source on copper surface at different temperatures at 0.3 mbar O_2 pressure.VB spectrum recorded at 500 K and above under the above conditions resembles that of Cu_2O. E_F feature is indicated by dotted arrow. All the spectra were normalized at BE = 3 eV. Metallic Cu features, such as E_F and steep increase in intensity at 2 eV, were observed up to 425 K, hinting a gradual oxidation of Cu to Cu_2O below 500 K. E_F intensity decreases with increasing temperature and disappears at 500 K indicating a complete oxidation to Cu_2O. However, oxidation of Cu_2O to CuO was not observed just by heating up to 800 K at 0.3 mbar O_2 pressure.

Temperature dependent VB spectra recorded at 0.3 mbar O_2 demonstrates a gradual change in Cu-metal to Cu_2O (Figure 3.2). However, an increase in temperature up to 800 K at 0.3 mbar O_2 partial pressure does not oxidize Cu_2O further. Even when 800 K at 0.3 mbar O_2 pressure was maintained for about 1 h, no further oxidation of Cu_2O to CuO was observed. In fact, from our earlier report [see Section 2.3.3 or Ref 5], it is clear that Cu oxidation is possible at higher pressures. Hence, oxidation was carried out at 0.8 and 1 mbar O_2 pressure at 625 K, but the UVPES was recorded at 0.3 mbar pressure and at 625 K. Due to severe attenuation in photoelectron intensity ≥0.4 mbar, the above procedure was followed.

First, high pressure dosing of O_2 at 0.8 and 1 mbar at 625 K was carried out, followed by VB spectra recording at 0.3 mbar O_2 pressure and 625 K demonstrating further oxidation of Cu_2O to CuO. A broadening of Cu 3d along with a shift in O 2p to lower BE eliminates the valley between the above features, observed for Cu_2O. Strong hybridization between Cu 3d and O 2p bands leads to the above energy changes, and this is confirmed by changes in Cu 2p core level and X-ray excited Auger electron spectral (XAES) LMM KE. Fully resolved vibrational features of molecular O_2 were observed after complete oxidation to CuO. Vibrational features of O_2 shift by 0.15 and 0.1 eV with further oxidation due to 0.8 and 1 mbar treatment, respectively, underscoring the change in work function from Cu_2O to CuO. A simple comparison of the present result with that of pure Cu_2O and CuO at UHV by Ghijsen et al. [7] matches very well. It is also to be noted that earlier we reported on Cu oxidation to Cu_2O and CuO by APPES at 1 mbar O_2 pressure between 300 and 675 K; however, core level and VB changes were followed exclusively with XPS. It is evident from Figure 3.1 that Cu to Cu_2O occurs at 0.3 mbar O_2 pressure. Further oxidation of Cu_2O to CuO requires higher pressures up to 1 mbar. Hence, the high pressure (0.8 and 1 mbar) treatment was carried out, but the UVPES spectra were recorded at 0.3 mbar (Figure 3.1), due to signal attenuation, as noted above.

Relevance of these studies stems from the fact that the evolution of direct electronic structure was addressed, such as,

(a) overlap in energy levels of Cu 3d and O 2p bands in CuO which also underscores the strong hybridization between the two orbitals, however,

no energy overlap between Cu 3d and O 2p for Cu_2O, (b) changes in surface work function from metallic Cu to CuO through shift in vibrational features of molecular oxygen, and (c) changes in Fermi level features.
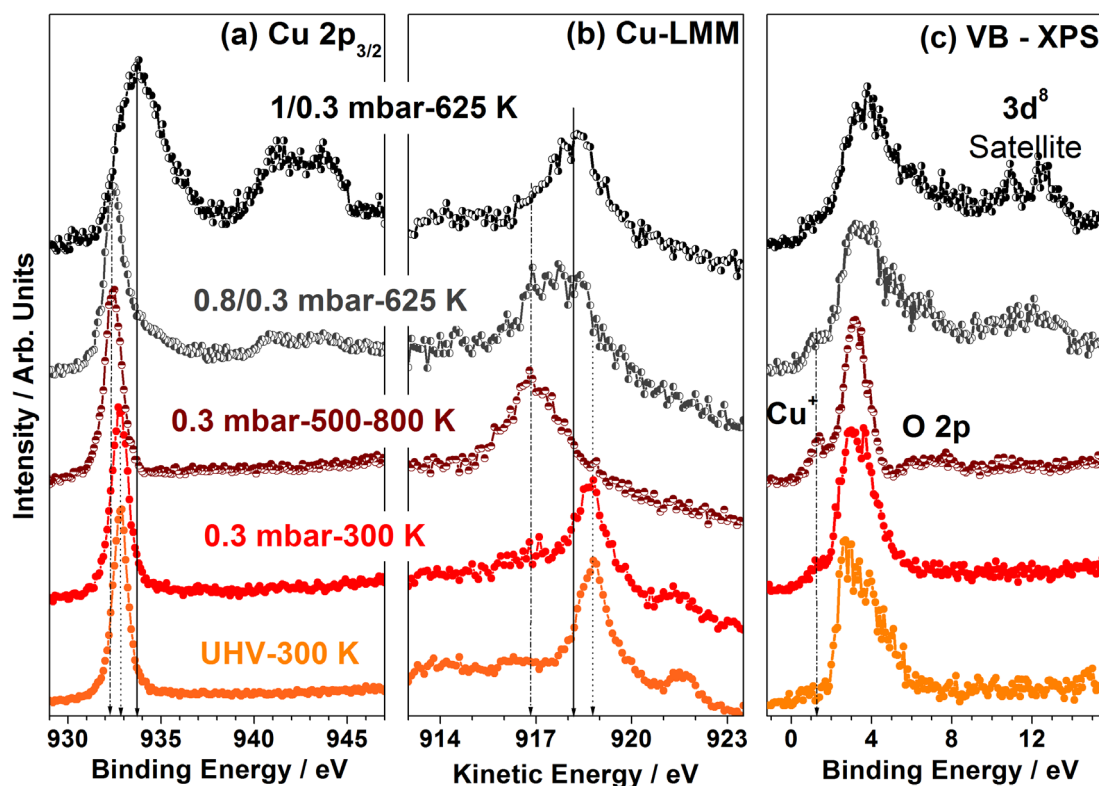
Figure 3. 3 (a) Cu $2p_{3/2}$ core level, (b) Cu LMM, and (c) VB spectra measured while Cu surface was exposed to O_2 at NAP and at various temperatures. Dotted, dash-dot, and solid lines indicate the position of Cu^0, Cu_2O, and CuO, respectively. The top two sets of spectra in all panels were recorded first at 1 mbar (black traces) or 0.8 mbar (gray traces) and subsequently at 0.3 mbar O_2 pressure, while maintaining the temperature at 625 K. Spectra recorded at 1 and 0.8 mbar pressures are similar to that of the results recorded later at 0.3 mbar. Characteristic narrowing of 3d bands for Cu_2O and $3d^8$ satellites for CuO were observed in the VB spectrum highlighting that the changes in electronic structure can be mapped as a function of measurement conditions. Results presented here are similar to our earlier work (*See* 2.3.3) on Cu oxidation at 1 mbar O_2 and different temperatures.

All the above information was possible due to the higher resolution with UVPES than that with XPS (420 meV). It is also to be noted that we could observe UVPES results with a conventional UV discharge lamp in a laboratory

APPES system and without any shielding. however, core level and VB changes were followed exclusively with XPS. VB spectra shown in Figure 3.1 are fully corroborated with the measurements made with Cu 2p core level, XAES of Cu-LMM level, and VB spectra recorded with Al Kα, and the results are shown in Figure 3.3. Our earlier report on Cu oxidation at 1 mbar and different temperatures (*see* 2.3.3) also gives similar results, but the results presented here are collected independently while collecting the data presented in Figure 3.1. It is to be noted that the top two sets of spectra (Figure 3.3a −c) were recorded first at 1 mbar (black traces) or 0.8 mbar (gray traces) and subsequently at 0.3 mbar O_2 pressure, while maintaining the temperature at 625 K; however, no significant difference was observed within a set of results. This set of experiments was carried out exclusively to simulate the conditions employed in UVPES (black and gray traces in Figure 3.1). BE and fwhm for Cu $2p_{3/2}$ core level from Cu (932.8 and 0.76 eV) and Cu_2O (932.4 and 0.95 eV) are not too different but can be differentiated with different XAES LMM KE values as they appear at 918.8 and 916.8 eV, respectively [5, 8, 9]. Cu_2O was partially oxidized to CuO at 0.8 mbar at 625 K (observed as shoulder at 933.8 eV), and typical Cu 2p satellite features (940 −945 eV) were observed along with a broad shoulder at 934 eV. The above broad shoulder develops into a complete feature at the cost of Cu_2O while O_2 dosing at 1 mbar. Satellite features too grow strongly and demonstrate the oxidation of Cu_2O to CuO, and it requires both high pressure (1 mbar) and temperature (625 K). Cu LMM also shows corresponding changes, and it shifts to 918.2 eV on CuO formation.

VB spectra recorded with Al Kα are shown in Figure 3.3c and correspond and complements well with the changes observed with UVPES results given in Figure 3.1. The broad Cu 3d feature of metallic Cu gradually narrows down with a distinct feature at 1.2 eV on Cu_2O formation at 0.3 mbar O_2 pressure between 500 and 800 K (wine red trace in Figure 3.3c). A major change occurs in the VB spectrum on increasing the temperature to 625 K and pressure up to 1 mbar. VB broadens between 1 and 13.5 eV, and the typical Cu_2O feature at 1.2 eV decreases in intensity. Further, a broad feature is observed between 9 and 12.5 eV. Indeed, this feature is very characteristic for CuO and attributed to a satellite due to $3d^8$ final state configuration [7−9]. Photoionization of $3d^9$ ground state configuration leads to the above satellite.

The main VB feature observed at 3.5 eV, due to Cu 3d bands, overlaps with the O 2p feature between 3.5 and 7.5 eV. The above energy overlap is attributed to the strong hybridization of Cu 3d and O 2p orbitals in CuO, which is typical for cuprates [7, 9].

Very different photoionization cross-section (σ) values for O 2p (0.00024 Mb) and Cu 3d (0.012 Mb) at $h\nu = 1486.6$ eV help to confirm the origin of VB features [4]. Indeed, Cu 3d spectral weight is primarily observed in the VB at $2-4$ eV for Cu, Cu_2O, and CuO, and it is fully supported by the larger σ of Cu 3d, by about 2 orders of magnitude than that of O 2p. In contrast, O 2p (0.16 Mb) exhibits significantly higher σ than that of Cu 3d (0.10 Mb) at $h\nu = 21.2$ eV. On Cu_2O and CuO formation, an almost equal intensity of Cu 3d and O 2p features was observed in Figure 3.1.

Results reported in Figures 3.1 and 3.3 are as expected and in agreement with literature results reported for Cu, Cu_2O, and CuO [7–9]; it suggests that there are no artifacts in the reported experiments and results. 1.2 mm distance was maintained between the sample and aperture making it 1.5 D (D = aperture diameter = 0.8 mm); constant O_2 pressure as well as in situ heating of O_2 to the measurement temperatures avoid any artifacts. Shifts in vibrational features of molecular O_2 due to changes in work function of Cu, Cu_2O, and CuO fully support the reliability of measurements at NAP. Possible reasons for the observation of low KE electrons are given below.

Calculations of inelastic mean free path, λ_m (m = monolayers, ML), within solids by the Seah and Dench [10] method were made. Figure 3.4 shows the 'universal curve' for electron inelastic scattering mean free path as a function of electron kinetic energy. For elements and inorganic compounds the scatter about the 'universal curve' was observed least when the pathlengths were expressed in monolayers, λ_m [10]. Analysis of the inter-element and inter-compound effects shows that λ_m, is related to atom size and the most accurate relations are:

$\lambda_m = 538$ $E^{-2} + 0.41(aE)^{1/2}$ for elements and $\lambda_m = 2170$ $E^{-2} + 0.72(aE)^{1/2}$ for inorganic compounds, where a is the monolayer thickness (nm) and E is the electron energy above the Fermi level in eV.

The λ_m showed very high value at lower (< 30 eV) kinetic energies, minimum

with in the energy range 30-100 eV and again a rise for further increase in energy. It shows λ_m = 3.9 ML (4.6 ML) with a KE of 13 eV (550 eV) for metallic Cu at BE = 3 eV in Figure 3.1 (BE = 933 eV in Figure 3.3a). Up on Cu_xO formation, λ_m increases to 14 ML (8.1 ML) for KE = 13 (550) eV. λ_m calculated for low KE electrons is comparable for metal and higher for oxides than that of 550 eV electrons; this indicates the possibility of survival of low KE electrons at high pressures better than its high KE counterparts. This is further testified by comparable S/N ratio observed in Figures 3.1 and 3.3. Due to low penetration depth of He I than Al K_α photons, the present VB analysis is exclusively limited to the top 1−2 surface atomic layers, and hence, the above λ_m values are sufficient to survive the NAP conditions for about 2 mm. It is to be noted that the density of a gas at 0.1 −1 mbar and 298 K is 6 −7 orders of magnitude smaller than for a condensed solid. This translates into $\lambda \approx$ mm for low KE electrons in gas pressures of 0.1 −1 mbar [1b]. However, when the distance increases >1.2 mm between aperture and sample surface, electron counts decrease drastically and at >1.5 mm no electron counts were observed, except for vibrational features of O_2.
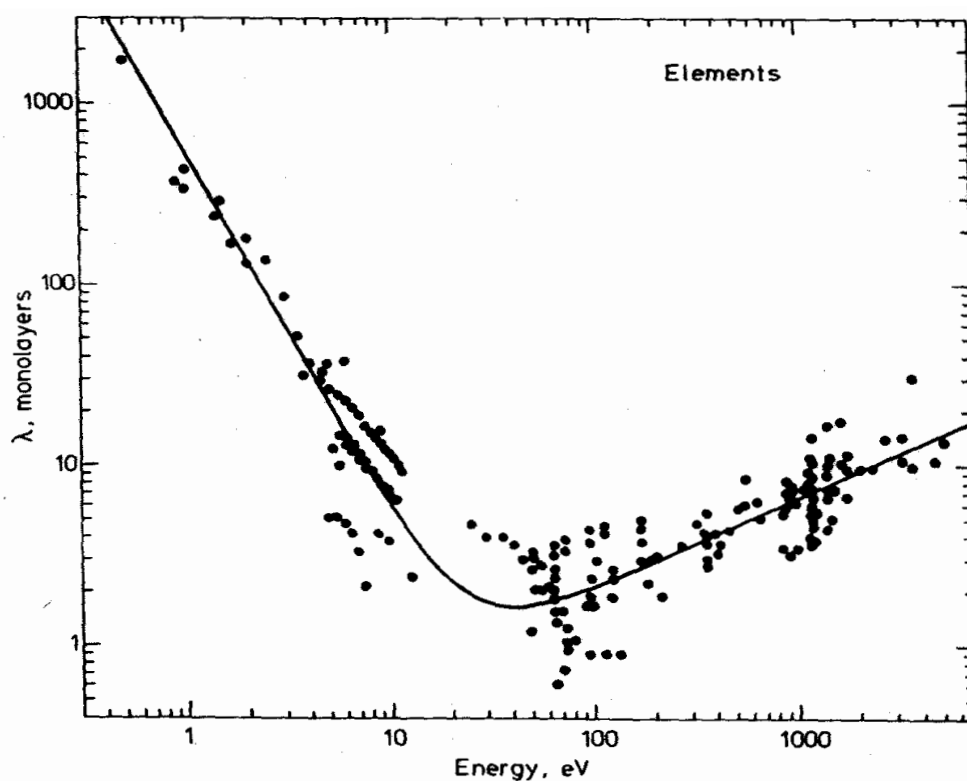
Figure 3.4 Universal curve for inealstic mean free path of electrons in solid (After Seah and Dench [10]). Reproduced with the permission from Ref [10].

No significant inelastic scattering occurs in the region of interest with KE = 7 −16 eV (BE = 9 −0 eV), which would otherwise attenuate the electrons severely. However, elastic scattering and rotational and vibrational cross section are expected to contribute significantly with low KE electrons. Elastic scattering would drift some electrons, and hence, they cannot be transmitted; hence, a decrease in some electron counts is expected. Rotational and vibrational cross section, at the best, could broaden peaks in VB spectrum due to energy loss of a few meV. Our observations and conclusions are in very good agreement with the theoretical calculations of predominant elastic and rotational cross sections for low energy electrons, with no significant contribution from inelastic scattering [11]. In spite of the large difference in KE of photo emitted electrons that originate due to UV or X-ray source, very low or no inelastic scattering characterizes the low KE electrons. It is also to be noted that the photon flux of He I is at least 10^{16} photons/s·sr and about 3 to 4 orders of magnitude higher than Al K_α and helps toward higher counts under comparable conditions (see Figures 3.1 and 3.2). Under the present NAP conditions, S/N ratio is decided by large electron attenuation with high KE electrons; however, in spite of low KE electrons, better S/N was managed due to high photon flux of He I with some elastic scattering and rotational cross section.

Double front cone design employed in ELR improves the vacuum from aperture, as it is pumped by both first and second differential pumps in the lens column (discussed in Chapter 2, see Fig. 2.2). Further, electron energy analyzer (R3000HP) is an aperture free lens column, which effectively increases the transmission and contributes to better quality results [5,12]. It is also to be noted that the open reactor design was employed in the present Lab-APPES unit and sample surface can be practically moved up to the aperture, as shown in the photograph (Figure 3.5). Capillary gas doser also can be moved up to the sample surface, and the pressure near the sample surface is measured through a CTR gauge (not shown in Figure 3.5). Pressure measured with the CTR gauge corresponds well with the pressure measured in other gauges, kept far away from sample surface. This arrangement fully ensures the reliability of NAP values.
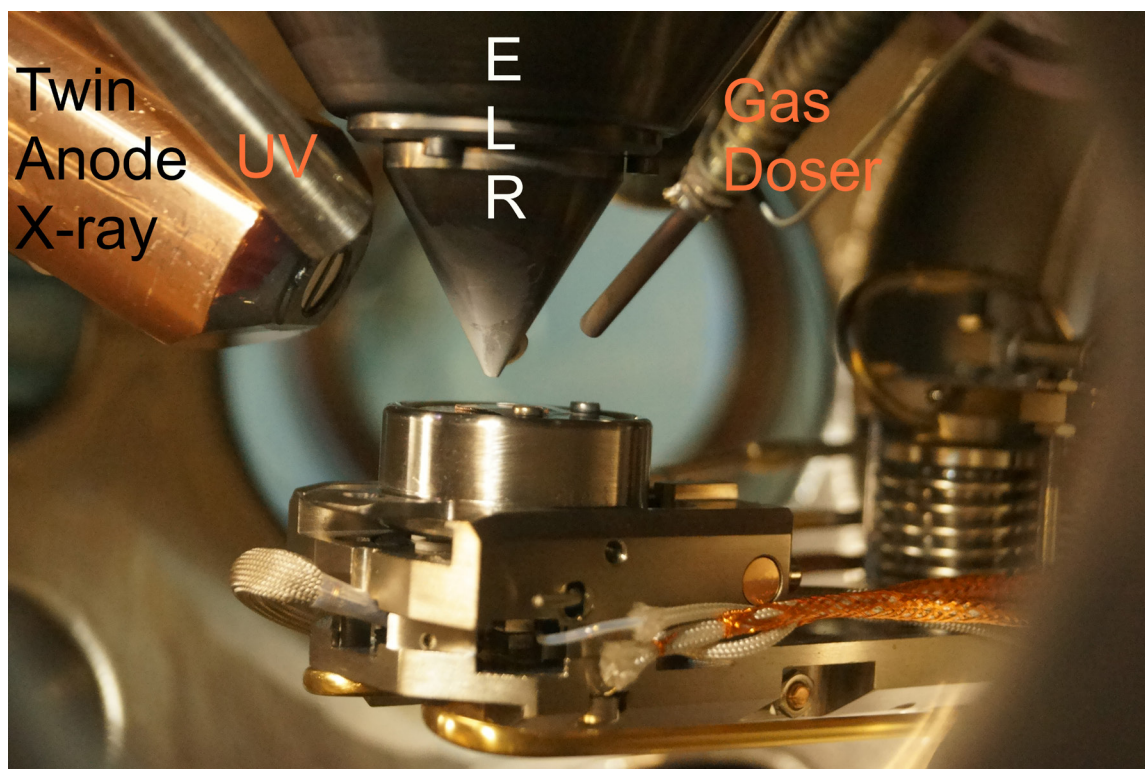
Figure 3.5. Photograph of the open-reactor design employed in Lap APPES unit. Sample holder can be moved up to the aperture of the front cone attached to the ELR. Gas doser can be heated to heat the input gas to minimize the temperature difference between spectral measurement and gas temperatures.

§ 3.4 Conclusions

Through observation of low KE electrons at NAP and at high temperatures, the possibility of following valence band electronic structure under near working conditions of catalysts and materials is established. Cu surface was systematically oxidized to Cu_2O, mixture of Cu_xO, and finally to CuO. Results observed in VB with low KE electrons are corroborated with that of results observed from high KE electrons, such Cu 2p core level. Insignificant inelastic scattering and high photon flux helps to observe low KE electrons and hence VBES. We believe a similar observation is possible with other Lab-APPES and APPES systems. Better quality results, than the present set of results, are possible with high brilliance photon sources, and it is worth exploring.

§ References

[1]. (a) M. Salmeron, R. Schlögl, *Surf. Sci. Rep.* **2008**, *63*, 169-199. (b) D. F. Ogletree, H. Bluhm, G. Lebedev, C. S. Fadley, Z. Hussain, M. Salmeron, *Rev. Sci. Instrum.* **2002**, *73*, 3872-3877.

[2]. (a) S. Porsgaard, P. Jiang, F. Borondics, S. Wendt, Z. Liu, H. Bluhm, F. Besenbacher, M. Salmeron, *Angewandte Chemie International Edition* **2011**, *50*, 2266-2269. (b) F. Tao, S. Dag, L.-W. Wang, Z. Liu, D. R. Butcher, H. Bluhm, M. Salmeron, G. A. Somorjai, *Science* **2010**, *327*, 850-853. (c) T. C. R. Rocha, A. Oestereich, D. V. Demidov, M. Haevecker, S. Zafeiratos, G. Weinberg, V. I. Bukhtiyarov, A. Knop-Gericke, R. Schloegl, *Phys. Chem. Chem. Phys.* **2012**, *14*, 4554-4564. (d) R. Toyoshima, M. Yoshida, Y. Monya, Y. Kousa, K. Suzuki, H. Abe, B. S. Mun, K. Mase, K. Amemiya, H. Kondoh, *J. Phys. Chem. C* **2012**, *116*, 18691-18697.

[3]. (a) A. Kolmakov, D. A. Dikin, L. J. Cote, J. Huang, M. K. Abyaneh, M. Amati, L. Gregoratti, S. Guenther, M. Kiskinova, *Nat. Nanotechnol.* **2011**, *6*, 651-657. (b) F. Tao, *Chem. Commun.* **2012**, *48*, 3812-3814. (c) J. Pantfoeder, S. Poelmann, J. F. Zhu, D. Borgmann, R. Denecke, H. P. Steinruek, *Rev. Sci. Instrum.* **2005**, *76*, 014102/014101-014102/014109.

[4]. J. J. Yeh, I. Lindau, *At. Data Nucl. Data Tables* **1985**, *32*, 1-155.

[5]. K. Roy, C. P. Vinod, C. S. Gopinath, *J. Phys. Chem. C* **2013**, *117*, 4717-4726.

[6]. S. Evans, E. L. Evans, D. E. Parry, M. J. Tricker, M. J. Walters, J. M. Thomas, *Faraday Discuss. Chem. Soc.* **1975**, *58*, 97-105.

[7]. (a) J. Ghijsen, L. H. Tjeng, H. Eskes, G. A. Sawatzky, R. L. Johnson, *Phys. Rev. B: Condens. Matter* **1990**, *42*, 2268-2274. (b) J. Ghijsen, L. H. Tjeng, J. Van Elp, H. Eskes, J. Westerink, G. A. Sawatzky, M. T. Czyzyk, *Phys. Rev. B: Condens. Matter* **1988**, *38*, 11322-11330.

[8]. S. Poulston, P. M. Parlett, P. Stone, M. Bowker, *Surf. Interface Anal.* **1996**, *24*, 811-820.

[9]. (a) T. Mathew, B. S. Rao, C. S. Gopinath, *J. Catal.* **2004**, *222*, 107-116. (b)

M. Vijayaraj, C. S. Gopinath, *J. Catal.* **2006**, *241*, 83-95. (c) S. Velu, K. Suzuki, M. Vijayaraj, S. Barman, C. S. Gopinath, *Appl. Catal., B* **2005**, *55*, 287-299.

[10]. M. P. Seah, W. A. Dench, *SIA, Surf. Interface Anal.* **1979**, *1*, 2-11.

[11]. A. Munoz, J. C. Oller, F. Blanco, J. D. Gorfinkiel, P. Limao-Vieira, G. Garcia, *Phys. Rev. A: At., Mol., Opt. Phys.* **2007**, *76*, 052707/052701-052707/052707.

[12]. F. Mangolini, J. Åhlund, G. E. Wabiszewski, V. P. Adiga, P. Egberts, F. Streller, K. Backlund, P. G. Karlsson, B. Wannberg, R. W. Carpick, *Rev Sci Instrum* **2012**, *83*, 093112.

Chapter 4

NO$_x$ Reduction at Near Ambient Temperatures and Under Lean-Burn Conditions on Modified Pd Surfaces

Catalytic conversion of NO in the presence of H_2 and O_2 has been studied on Pd(111) surfaces, by using a molecular beam instrument with mass spectrometry detection, as a function of temperature and reactants composition. N_2 and H_2O are the major products observed, along with NH_3 and N_2O minor products under all conditions studied. Particular attention has been paid to the influence of O_2 addition toward NO dissociation. Although O_2- rich compositions were found to inhibit the $deNO_x$ activity of the Pd catalyst, some enhancement in NO reduction to N_2 was also observed up to a certain O_2 content. The reason for this behavior was determined to be the effective consumption of the H_2 in the mixture by the added O_2 and O atoms from NO dissociation. NO was proven to compete favorably against O_2 for the consumption of H_2, especially ≤ 550 K, to produce N_2 and H_2O. Compared with other elementary reaction steps, a slow decay observed with the $2H + O \rightarrow H_2O$ step under SS beam oscillation conditions demonstrates its contribution to the rate-limiting nature of the overall reaction. Pd(111) surfaces modified with O atoms in the subsurface (SM-Pd(111)) induces steady-state NO reduction at near-ambient temperatures (325 K) and opens up a possibility to achieve room temperature emission control. A 50% increase in the reaction rates was observed at the reaction maximum on SM-Pd(111), as compared with virgin surfaces. Oxygen adsorption is severely limited below 400 K, and effective NO $+ H_2$ reaction occurs on SM-Pd(111) surfaces. Valence band photoemission with a UV light source (He I) under different oxygen pressures with APPES clearly identified the characteristics of the SM-Pd(111) surfaces and PdO. The electron-deficient or cationic nature of SM-Pd(111) surfaces enhances the NO dissociation and inhibits oxygen chemisorption ≤ 400 K under lean-burn conditions.

§ 4.1 Introduction

The selective catalytic reduction of NO_x to nitrogen (deNO_x) is a known method for removing this pollutant from stationary as well as mobile sources, such as a three-way catalyst (TWC) converter in automobiles. The aim of TWC used in automobiles is to convert pollutants (NO_x, CO, volatile organic compounds (VOCs)) to benign gases, such as N_2, H_2O (and CO_2). Currently employed internal combustion (IC) engines in automobiles work at higher fuel efficiency, that is, at a high air/fuel ratio, than that of their counterparts employed one to two decades ago. Hence, oxidation processes, such as CO oxidation to CO_2 and complete combustion of VOCs, become more favorable; however, in contrast, reduction of NO_x under net oxidizing conditions becomes a serious problem. A predominant challenge to both industrial and academic research is, therefore, the selective reduction of NO_x under predominantly oxidizing or lean-burn conditions. Many deNO_x techniques have been tried so far using different single or multiple reducing components, such as CO, NH_3, urea, hydrocarbons, or H_2. Recently, H_2-selective catalytic reduction (SCR) [1, 2] has become of interest for deNO_x. The fact is that H_2-SCR is a totally green method because it generates N_2 and H_2O as products. By adopting H_2-SCR, different tricky issues of NH_3-SCR, such as vanadia emission, NH_3 slippage, and air heater fouling, can be easily avoided. The NO_x reduction temperature by H_2 is comparatively lower, and H_2-SCR has technological potential, too, because H_2 is available in many post-combustion methods. H_2 can be generated in diesel engines by auto thermal reforming of diesel [3]. These facts encourage H_2-SCR for onboard deNO_x in IC engines.

The present study focuses on H_2-SCR by palladium under lean-burn conditions. Rh is well-known over Pd for NO reduction to N_2 in the first-generation TWC working at a stoichiometric air/fuel ratio (~14.6). Nonetheless, both Rh and Pt form irreversible oxides under net oxidizing conditions, whereas Pd shows more oxygen tolerance. This reason promotes shifting of TWCs from Rh-/Pt-based to Pd-based catalysts [4]. Therefore, the kinetics of the most representative reactions involved on TWCs, such as the NO + H_2 and NO + H_2 + O_2 reactions on Pd-based materials, have been the subject of a wide number of publications from surface science approaches, performed under ultrahigh vacuum (UHV), [5−9] to more realistic conditions at atmospheric pressures [10−22]. Direct dissociation probability of NO influences the rate of the NO + H_2 reaction below 373 K.

According to Hecker and Bell [21], and Burch and Watling [22], an alternative path of NO decomposition, called H_2-assisted NO decomposition, could lead to an increase in the reaction rate; however, the evaluation of single crystal data concludes that both reactions can be adequately explained by an initial direct dissociation of NO, followed by removal of the fragments by adsorbed reductant. Detailed kinetic and operando spectroscopy work carried out by Granger et al.[18] supports that in the absence of O_2, the dissociation of NO_{ads} species is assisted by chemisorbed H atoms on Pd/Al_2O_3; however, in the presence of a large excess of O_2, this decomposition is not favorable. In the presence of O_2, hydrogen is easily consumed by oxygen. Oxygen addition increases NO decomposition at relatively low temperatures on $Pd/LaCoO_3$. The $H_2 + O_2$ reaction pathway is faster than the $NO + O_2$ reaction pathway [10]; therefore, oxygen has a detrimental effect on the overall $NO + H_2 + O_2$ reaction. However, Wen [11] shows that an inhibiting effect of oxygen on NO reduction at 373 K is not significant; rather, it plays a positive role by decreasing the steady-state (SS) concentration of H_2 and, thus, providing more vacant sites for NO. Literature reports also suggest two different mechanistic channels for low- and high-temperature NO reduction processes. Over Pd/TiO_2 catalyst, there were two NO_x conversion maxima observed. IR results showed that the $Pd^{2+}-NO$, Pd^0-NO, Pd^+-NO, and a bent Pd nitrosyl species existed at 393 K, whereas at 513 K, these bands disappeared, and a new band due to NH_x species on the Lewis acid sites appeared [12]. This phenomenon indicated that the reaction paths were quite different at these two temperatures. From the above discussion, it is clear that the nature of the active intermediate species and, hence, the reaction mechanism depends on the chemical and electronic nature of the active sites, the support type, and the preparation conditions. We address the reaction kinetics of NO reduction by H_2 under net-oxidizing conditions on Pd(111) and a surface that are modified with O atoms in the subsurfaces, called modified Pd(111) (SM-Pd(111)) surfaces. The latter is mainly to simulate the calcination conditions carried out on supported Pd-based catalysts employed in the literature [10 −22]. Ultraviolet photoelectron spectroscopy (UVPES) and XPS measurements were carried out with ambient pressure photoelectron spectrometer (APPES) in the presence of O_2 at relevant conditions to explore the electronic structure changes under experimental conditions. The present set of results is part of our efforts in exploring the TWC reactions, such as CO oxidation and NO reduction with different reductants on Pd surfaces [9, 23 −32].

§ 4.2 Experimental Section

The isothermal kinetic measurements have been performed in a home-built molecular beam instrument (MBI) using an effusive molecular beam doser. The description of MBI is already discussed in Chapter 1 and also available in our earlier reports [23, 24]. The Pd(111) single crystal (Metal Oxide Ceramics, UK) was cleaned by the standard procedure of Ar^+ sputtering in an oxygen atmosphere (total pressure of 1.5×10^{-6} Torr) at 950 K and subsequent annealing at 1100 K. Temperature programmed desorption (TPD) spectra were recorded at a constant heating rate of 10 K/s. NO (SG Spectra Gases 99%), H_2 (Sigma-Aldrich), and O_2 (Inox Air Products Ltd., 99.999%) were used without any further purification. Controlled and systematic experiments were measured with a combination of labeled reactants (^{15}NO (99% isotopic purity with 1% ^{14}NO), $^{18}O_2$, (98% pure and 2% of $^{16}O_2$ and $^{18}O-^{16}O$), D_2 (99% isotopic purity and 1% H_2) to measure the contribution from different overlapping mass species, such as $^{15}NH_3$ ($^{15}ND_3$, ND_3, and NH_3) and H_2O (D_2O). Nevertheless, throughout the chapter, all the reactions are simply mentioned as NO + H_2 + O_2. Whenever a second labeled isotope component was employed, the first two experiments were not taken into account for any calculation or reporting purposes due to facile isotope exchange. The majority of isotope exchange decreases after the above flushing action, and results obtained thereafter are reported. A total flux (F) of reactants of 0.64 monolayer per second (ML/s) was used in all the experiments reported here unless otherwise specified. The diameter of a Pd(111) single crystal is 8 mm, and 10 mm is the diameter of the molecular beam; 45% of the molecular beam is intercepted at a distance of 5 mm between the molecular beam doser and Pd(111) surface under the experimental conditions reported [23]. Because of high flux conditions on the sample surface, readsorption of gas molecules from the gas phase (after adsorption from direct molecular beam) is small and well within the experimental error limit of 5%.

Isothermal molecular beam experiments were performed on clean Pd(111) and on SM-Pd(111) (O populated in the subsurface) between 325 and 700 K with $xNO + yH_2 + zO_2$ (x:y:z represents the composition of the respective individual components; x = 1, y = 1−4, and z = 0−3). The mass spectrometer signals are calibrated for reactants and products by leaking pure components individually.

The contribution from the background to the measurements of the reaction rates was estimated to be within $\pm 5\%$ of that from the direct beam by independent calibration experiments and was not considered for calculations of the SS rates and coverages [9, 23, 24]. Reaction rates reported are reproducible within 5% error for major products (N_2 and H_2O), and 20% error for minor products (N_2O and NH_3). For the details about the MBI experiments and measurement of different kinetic parameters one can also refer our earlier publications [9, 25, 27].

APPES [33] was used to show the changes in surface characteristics due to O_2 dosing on Pd surfaces. The Lab-APPES unit is equipped with VG Scienta's R3000HP electron energy analyzer (EEA), and it has several advantages that are listed in Chapter 2 and Ref 33. EEA is equipped with three differential pumping stages to maintain a high vacuum under high pressure experimental conditions. Two sets of differential pumping are available in the electrostatic lens regime (ELR), and the third one is available in the analyzer. The distance between the sample surface and the tip of the cone attached to ELR can be decreased up to 100 µm.

The X-ray monochromator (MX650 from VG Scienta) is isolated from the analysis chamber by a thin aluminum window (5 µm). A UV discharge lamp source (UVS40A2, Prevac) with photon flux of 10^{16} photons/s.sr was employed for measuring the valence band (VB). The distance between the sample surface and aperture (of the cone, D = 1.2 mm) attached to the ELR was maintained at 1.4 mm for the experiments reported herewith. Further, a special design of a double front cone pumping arrangement [33] is available in the ELR. The main advantage with this design is a fast decrease in pressure with a steep pressure gradient from the aperture to the EEA.

§ 4.3 Results and Discussions

4.3.1 General Considerations

Kinetic runs were carried out for NO + H_2 + O_2/Pd(111) between 400 and 700 K and for NO + H_2 + O_2/Md-Pd(111) between 325 and 700 K. There is no hysteresis observed between temperature ramping from low to higher temperatures or vice versa. Steady state results reported were reproduced many times within the experimental error limit. Although $^{15}NO_2$ (amu = 47) was also recorded, no

measurable intensity was observed, suggesting that there is no NO_2 production under the present experimental conditions. Indeed, no NO_2 was observed in a similar work on Rh(111) and Pd(111) surfaces [30−36]. Many reference experiments were measured with a combination of different isotopes, such as ^{15}NO, $^{18}O_2$, and D_2, to measure the contribution from different overlapping mass numbers, such as $^{15}NH_3$ ($^{15}ND_3$) and H_2O (D_2O). As an example of the results obtained, Figure 4.1 shows the experimental data for the 1:1:1 beam composition reaction on Pd(111) surface.
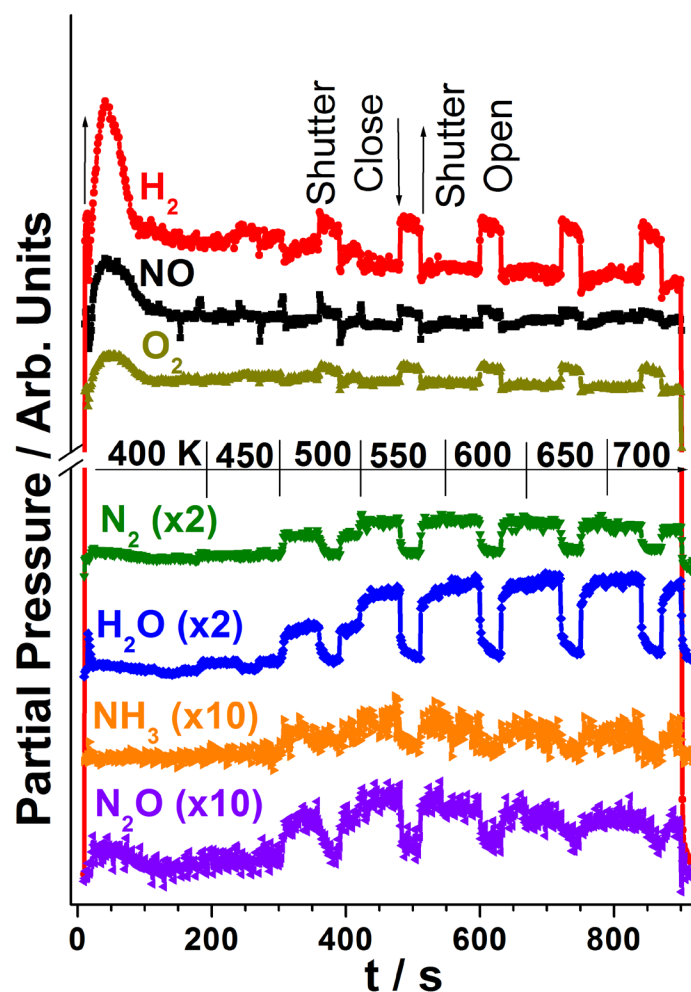
Figure 4.1 An effusive collimated $NO + H_2 + O_2$ molecular beam (of 1:1:1 NO $+ H_2 + O_2$ composition in this example) is directed onto a clean Pd(111) surface as the temperature is swept in 50 K steps between 400 and 700 K, and the partial pressures of both reactants (NO, H_2, and O_2) and products (N_2, H_2O, NH_3, and N_2O) are followed as a function of time. The beam is deliberately blocked and unblocked to measure the steady-state rates of different species directly, as they are proportional to the drop (increase) in partial pressure of the products (reactants) from their steady-state values.

Different steps followed in the experiments can be elaborated with reference to Figure 4.1: (1) The temperature of the crystal is set at 400 K (in the present case). At t = 10 s, the molecular beam of the mixed reactants was turned on, keeping the shutter in a blocked position. The beam cannot react directly to Pd(111) surface. (2) The shutter was unblocked at t = 15 s. The beam can now directly react with Pd(111) kept at 400 K. The system is allowed to evolve until a SS is reached, which generally occurs within 60 s. The time from the unblocking of the beam to the SS reached is termed the transient state (TS). An increase in the reactants' partial pressure at the beginning of reaction was due to a flushing effect of reactants from the inner walls of the UHV chamber, which decreases with time and does not indicate a change in the flux (F) on Pd(111) [24, 25, 37, 38]. (3) In the SS, the rate of the reaction was measured by blocking the shutter for 30 s between t = 480 and 510 s at 550 K. An increase (decrease) in the partial pressure of all reactants (products) was observed while blocking the beam in the SS. The above observation and other results presented in this chapter highlight that the net adsorption is significantly influenced by the reaction conditions. The measured changes in the partial pressure of products allow direct determination of the SS reaction rates, indeed, after calibration with pure components. (4) After the rate measurement through the shutter operation at the first temperature was made, the crystal was heated to measure the SS rate for the next temperature. This procedure was followed to measure the rate at several temperatures up to 700 K in the example shown in Figure 1. (5) Finally, the molecular beam was turned off at t = 920 s (Figure 4.1). TPD was recorded at a heating rate of 10 K/s after the system again reached UHV.

A systematic study of the $NO + H_2 + O_2$ reaction kinetics on Pd(111) surfaces was carried out by following the above procedure as a function of temperature and $NO/H_2/O_2$ composition. A detailed analysis of the kinetic data from NH_3 and N_2O was difficult because of a poor S/N ratio associated with the data. However, at the time of shutter opening or closing, a good change in the partial pressure of all the products (including N_2O and NH_3) demonstrated that a major contribution is due to molecular beam. To understand the NO reduction under net oxidizing conditions, a wide range of temperatures and beam compositions were studied, and the results are described in the following sections.

4.3.2 Temperature Dependence.

Figure 4.2 displays the kinetic data for time evolution of all products, N_2, H_2O, NH_3, and N_2O, due to reaction of $NO + H_2 + O_2$ (1:2:1) composition on a Pd(111) surface while ramping the temperature in a stepwise manner between 400 and 700 K, as explained in Figure 4.1. No significant N_2 production could be observed up to 450 K, but a small but sustainable SS H_2O production occurs from 400 K. At temperatures >450 K, the SS production of N_2 and H_2O increases rapidly with temperature, until reaching a reaction maximum located between 550 and 600 K. It should be noted that NO decomposition and the onset of NO + CO reaction on clean Pd(111) occurs between 400 and 450 K [24, 25], which is in good agreement with the present results; addition of H_2 and O_2 do not seem to alter the onset of the NO-decomposition temperature. Especially, introduction of oxygen does not significantly change the threshold temperature of NO reduction.

The kinetics observed in the SS for beam oscillation (immediately after shutter closing or opening) for H_2O is quite different from that for N-containing products (Figure 4.2 inset). Fast changes were observed in the partial pressure of N containing products on blocking and unblocking the beam, whereas the H_2O pressure changes slowly. A slow change in the partial pressure of water is shown in the shaded area, which is the difference between experimentally observed kinetic decay and if the decay occurs without any delay (or rectangular decay). The main conclusion from this observation is that the diffusion-controlled nature of recombination of H and O atoms to molecular H_2O is likely to be the major rate-determining step (RDS) for the whole process under the conditions of those experiments.

It should be noted that N_2 formation is the RDS with NO +CO + O_2 on Pd(111) [24,30], and the change in reductant from CO to H_2 changed the RDS to water formation. Further, for all N-containing products, the rate decreases at ≥600 K, whereas the water formation rate remains almost the same between 500 and 700 K. This suggests that the decomposition of NO is predominant up to 550 K, and the oxygen supply for water formation is dominated by the NO dissociation. At 550 K and above, molecular oxygen dissociation competes strongly and starts supplying oxygen atoms predominantly for water formation.

It is also to be underscored that water formation remains the RDS at low as well as high temperatures (Figure 4.2, inset). A simple comparison between the kinetic data shown in Figures 4.1 and 4.2, indicating an increase in NH_3 production,

occurs with an increase in the H_2 content in the reactant composition. Very similar to the results in Figure 4.1, a 1:2:1 composition also shows a marginally increasing rate of H_2 and O_2 adsorption at temperatures higher than 550 K, whereas the rate of NO adsorption decreases gradually with increasing temperature. This supports the above conclusion of oxygen supply channel changes from predominantly NO dissociation at ≤550 K to O_2 dissociation at ≥550 K. N_2O formation was observed between 450 and 600 K, and it remains a minor product. Very less N_2O formation, suggesting the extent of NO dissociation into N + O, is much higher on Pd(111) surfaces than the interaction of molecular NO with N atoms.
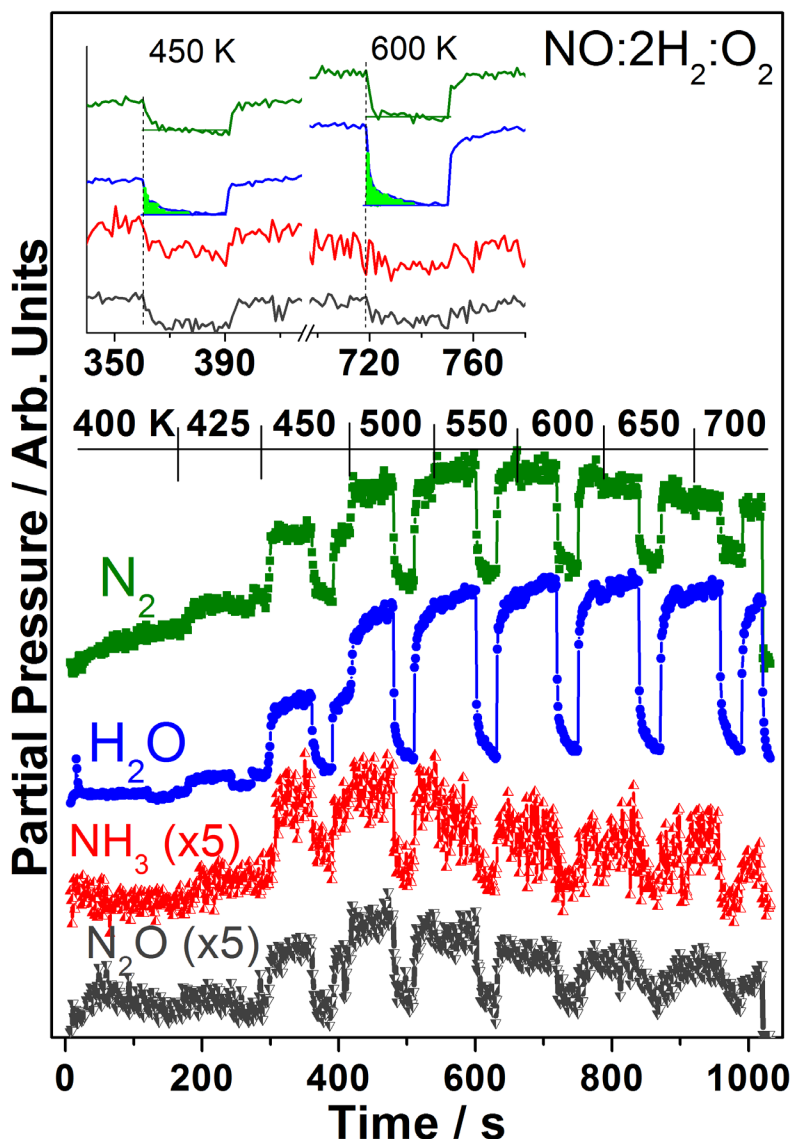
Figure 4.2 Temperature dependence of the SS rates for the formation of all the products (N_2, H_2O, NH_3, and N_2O) during the conversion of 1:2:1 $NO/H_2/O_2$ mixtures on Pd(111). Inset shows the decay kinetics of all products and new steady state reached slowly in the case of water formation at 450 and 600 K, suggesting its predominant role in controlling the overall kinetics.

4.3.3 Beam Composition Dependence.

To understand the NO dissociation aspects with increasing O_2 or H_2 content, the NO + H_2 + O_2 reaction was carried out as a function of the reactants' compositions. NO dissociation kinetics was measured by varying one of the reactant concentrations in the beam by fixing the other two as constant. Figure 4.3 displays the kinetic data of products formation for (a) N_2, (b) H_2O, (c) NH_3, and (d) N_2O on Pd(111) for different beam compositions and in the temperature range of 400 −700 K. The NO + H_2 reaction was also measured as a reference, as well as to understand the extent of atomic oxygen contribution to water formation through NO dissociation.
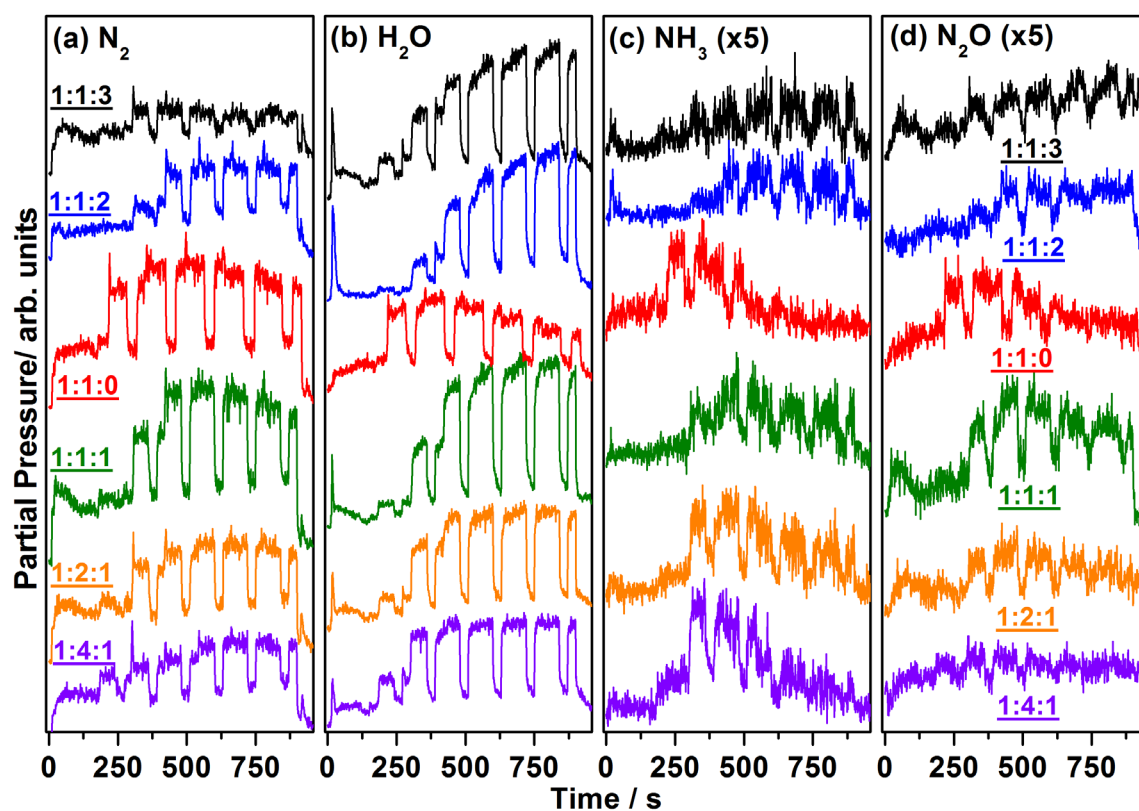
Figure 4.3 Time evolution of the partial pressure of the products (a) N_2, (b) H_2O, (c) NH_3, and (d) N_2O from the kinetic experiments, such as that described in Figure 4.1 as a function of temperature and O_2 and H_2 content dependence. ^{15}NO and D_2 were employed, and an initial rise in the partial pressure of amu 30, at the point of turning on the molecular beam, is due to 1% unlabeled NO. The changes in partial pressure of amu 30 under steady state conditions are exclusively due to $^{15}N_2$.

There are a few important observations worth highlighting:

(a) The extent of water formation is the lowest, with 1:1:0 composition, and it decreases at >550 K. Oxygen addition to the NO + H_2 mixture increases the rate of H_2O formation and its sustainability at a gradually increasing rate from 550 to 700 K. (b) A large amount of water formation in the TS at 400 K was observed with the oxygen-containing compositions, but it is not sustained in the SS, suggesting the role of adsorption of oxygen atoms derived from molecular oxygen for water formation is limited exclusively to the TS at low temperatures, whereas the NO + H_2 beam does not show any water formation in the TS. (c) A similar rate of N_2 production is evident from the reaction kinetics for 1:1:0 and 1:1:1 compositions, despite a decrease in F_{NO} from 50 to 33.3%. This highlights that a stoichiometric amount of oxygen addition is, indeed, beneficial to NO decomposition. Nonetheless, NO decomposition decreases with an increase in the O_2 content. However, H_2 addition makes the NO decomposition sustainable, even at 700 K, as observed with 1:2:1 and 1:4:1 compositions. (d) N_2 formation (and NO decomposition) is increasingly suppressed at the expense of water formation with high oxygen content at ≥550 K. (e) Ammonia formation shows a gradual increase with an increase in the amount of H_2 in the mixture of reactants. However, any oxygen addition to the NO + H_2 reactants mixture decreases the ammonia formation, suggesting the predominant H-consumption by O atoms is to form water; this oxygen cleanup facilitates NO dissociation, followed by N + N recombination to form N_2, especially below 550 K. It is also to be noted that, to the best of our knowledge, N_2O adsorption/dissociation on Pd single crystal surfaces has not been reported to date. Our efforts in the past have demonstrated the sticking coefficient of N_2O on Pd(111) is immeasurably small. This aspect, along with other observations, specifically supports the nitrogen forms through N + N recombination rather than through a N_2O intermediate; however, further *in situ* IR studies are suggested. (f) Although N_2O is a minor product, O_2 addition to a NO + H_2 mixture broadens the N_2O formation regime at high temperatures. Generally, N_2 production was observed from 500 K and above, with the rate maxima observed around 550 K for all of the beam compositions. Notably, H_2 addition enhances N_2 production at higher temperatures and, hence, makes NO dissociation sustainable.

4.3.4. Effect of Oxygen Addition on NO Dissociation.

The steady-state rates measured for various products due to $NO + H_2 + zO_2$ (z $= 0 -3$) reaction on Pd(111) surfaces between 400 and 700 K are shown in Figure 4.4. Compositions 1:1:0 and 1:1:1 show similar rate values and a similar trend for N_2 formation. In fact, a marginal increase in rate values with z = 1 indicates the addition of oxygen helps toward more NO decomposition. It is to be noted that F_{NO} decreases from 1:1:0 to 1:1:1 and this fact highlights an effective increase in NO dissociation and, hence, more N_2 production. Simultaneously, the rate of H_2 oxidation to H_2O occurs at a much higher rate with a 1:1:1 composition than with a 1:1:0 compositions. For the latter composition, the oxygen supply is exclusively due to NO dissociation, whereas in the case of 1:1:z (z ≥ 1), O_2 is an additional and main reactant source for the supply of atomic oxygen.

A higher rate of H_2O formation with all O_2-containing compositions than for that of the 1:1:0 composition, especially at ≥550 K, was observed. This result highlights the oxygen cleanup effect by H atoms, which leads to increasingly O-free surfaces with decreasing O_2 content in the reactants' composition. Indeed, this is the reason for the higher rate of N_2 formation with the 1:1:1 composition than that of 1:1:0. However, more O_2 has a detrimental effect on the overall NO dissociation reaction, especially to N_2 production. This can be explained in terms of competitive adsorption of NO and O_2. Despite the availability of oxygen in the 1:1:1 composition, the rate of water (and N_2) formation is the same with both 1:1:1 and 1:1:0 at ≤500 K. This observation confirms the dominance of NO through strong chemisorption, followed by dissociation [24] over O_2. Nonetheless, an increase (decrease) in the rate of water (N_2) formation at ≥550 K suggests a competitive adsorption by O_2 at the expense of NO and dictates a change in the reaction trend toward more oxidation. Because of the above, surface oxygen coverage (θ_O) increases, and it hinders the NO adsorption as well as decomposition. Addition of O_2 to the 1:1:0 composition initially increases (z = 1) the rate of formation of the minor products; however, with more O_2 (z = 2 or 3), a definite decrease in NH_3 and N_2O was observed. Because of a poor S/N ratio associated with the minor products, as shown in Figure 4.3, a more meaningful discussion cannot be presented. In conclusion, Pd(111) surfaces show ~75% selectivity to N_2 and 25% to the total of the other two N containing products.
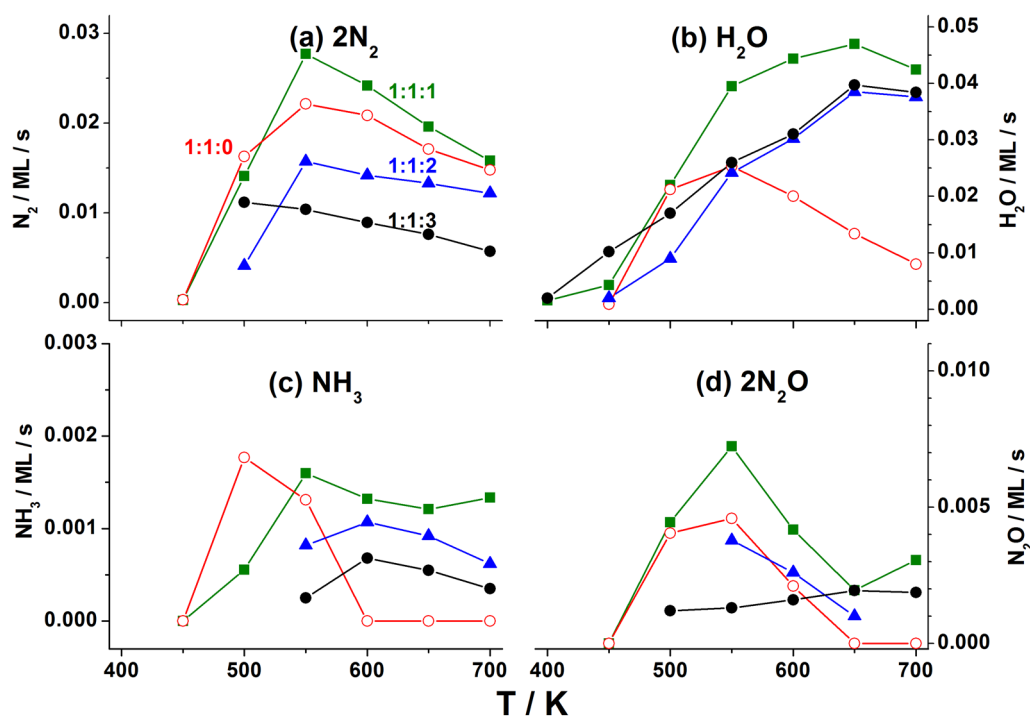
Figure 4.4 The SS rate measured for all the products from NO + H_2 + O_2 (1:1:z) reaction on Pd(111) surfaces are shown as a function of reaction temperature and O_2 content. (a) $2N_2$, (b) H_2O, (c) NH_3, and (d) $2N_2O$. The rates measured for N_2 and N_2O were multiplied two times because of the consumption of two NO molecules for the production of one molecule of the above products.

From the results shown in Figures 4.3 and 4.4, a qualitative trend for the NO and O_2 dominance of the overall NO + H_2 + O_2 reaction is shown below and above 500 K, respectively. Figure 4.5 shows the quantitative analysis of the rate values of oxygen and NO decomposition by adding 1 mol of oxygen to the 1:1:0 composition. The rate of H_2O formation (R_{H_2O}) values are directly borrowed from Figure 4.4. The rate of NO decomposition (R_{NO}) was measured from the raw kinetic data as well as calculated from Figure 4.4 through the following equation (eq 4.1):

$$R_{NO} = 2R_{N_2} + 2R_{N_2O} + 2R_{NH_3} \qquad (4.1)$$

It is a fact that the formation of one N_2 molecule requires two N atoms derived from dissociation of two NO molecules. Similarly, formation of one N_2O molecule requires one N atom as well as one NO molecule, which effectively translates into

the conversion of two NO molecules. R_{NO} dissociation calculated through the above equation and directly from the experimental results matches within a 10% error limit, and for brevity, the results obtained through the above equation are shown in Figure 4.5. Further, direct measurement of NO dissociation was not possible below 500 K because of high coverage of different species and, hence, a sluggish rate. The rate of O_2 consumption (R_{O_2}) shown in Figure 4.5 was calculated by the difference in R_{H_2O} formation between 1:1:1 and 1:1:0 compositions. There are two important points to be highlighted: (a) A clear demarcation in the results exists between 500 and 550 K, above which R_{O_2} increases with temperature and contributes predominantly toward H_2O formation. Simultaneously, R_{NO} decreases linearly with increasing temperature. However, below 550 K, the overall reaction was dominated by R_{NO}. (b) Despite oxygen addition to the 1:1:0 composition, R_{NO} shows ~30% higher values at ≥550 K with the 1:1:1 composition than with the former and reiterates that some amount of oxygen helps toward increasing R_{NO}. Indeed, hydrogen helps to remove oxygen atoms through water formation [10].

There are two precautions to be remembered while interpreting the data shown in Figure 4.5: (a) Because N_2O formation requires consumption of equal amounts of NO molecules and N atoms, the R_{NO} is higher than that of R_{H2O} for 1:1:0 composition. The amount of molecular NO consumed for N_2O formation does not contribute to water formation, and hence, R_{NO} is higher than R_{H_2O}. (b) R_{H_2O} is expected to be equal to the sum of $R_{NO} + R_{O_2}$ for the 1:1:1 composition; however, R_{H_2O} is lower than the above sum, especially when the temperature is ≥550 K. This is mainly attributed to the disappearance of some of the O atoms through diffusion into the subsurfaces and possibly into the bulk of the Pd(111) surfaces; this phenomenon is well reported in the literature [27, 39]. Indeed, the difference between $R_{NO} + R_{O_2}$ and R_{H_2O} increases at higher temperatures, suggesting the rate of oxygen diffusion into the subsurfaces increases at higher temperatures.

Under practical driving conditions of automobiles, the temperature of the exhaust gases varies widely and influences the performance of TWCC. This would lead to the above such oxygen diffusion into the subsurface and bulk of Pd particles on supported catalysts. In fact, a simple calcination of supported Pd catalysts in air above 550 K would lead to oxygen diffusion and possible partial oxidation of Pd. Many deNO$_x$ researchers adopted such calcination as a pretreatment before NOx decomposition activity and reported results considerably different from that of the pre-reduced catalysts[10 −12, 16, 18]. To understand this effect, we

embarked on modifying the surface deliberately by exposing the Pd(111) surfaces to high temperatures under an oxygen atmosphere and reevaluated the NO + H_2 + O_2 reactions on the modified surfaces. The results obtained are discussed in the following section.
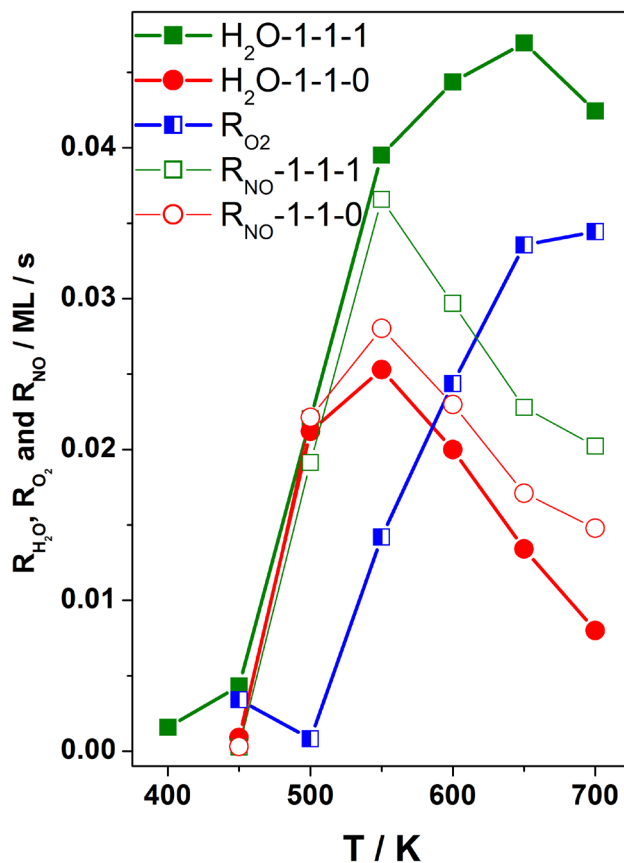
Figure 4.5 The rate of water formation and NO and O_2 consumption by Pd(111) surfaces is given at different temperatures for the 1:1:0 and 1:1:1 compositions. The rate of NO dissociation matches that of the sum of N-containing products (eq 4.1) within an error limit of 10%.

4.3.5. Preparation of Modified Pd(111) (SM-Pd(111)) Surfaces .

Oxygen diffusion into Pd is a well-known phenomenon [26,27]. There are a significant number of reports available that suggest the formation of different oxide phases (oxide on surface, subsurface; metastable oxides and bulk oxides) due to the interaction of oxygen with Pd at a wide temperature and pressure range [39 −51]. The variations in the catalytic activity of Pd in the reactions associated with oxygen have been attributed to the different activities of the different kinds of oxygen species. The role of other moieties, such as C or H, in

the Pd subsurface is also worth mentioning [52]. Earlier studies from Gopinath et al. have shown kinetic evidence of the influence of subsurface oxygen on the CO oxidation reaction at high temperatures (600 −900 K) [26, 27]. The effect of subsurface oxygen is remarkable because it changes the electronic nature of the surface as a result of its proximity to the surface, and hence, changes in fundamental adsorption characteristics could occur. A simple vacuum annealing at 1200 K desorbs the subsurface oxygen and brings back the original virgin surface.

We carried out the $NO + H_2 + O_2$ reaction on Pd(111) with subsurface populated O, and this surface will be represented as modified Pd(111) (SM-Pd(111)). The subsurface oxygen was populated by dosing oxygen at 900 K because it shows maximum subsurface oxygen coverage [27]. CO titration was carried out for each cycle to eliminate the possibility of the presence of any chemisorbed oxygen on the surface. Figure 4.6 shows the experimental data for $^{18}O_2$ dosing at 900 K, followed by CO titration at 525 K and then reaction of CO $+ ^{16}O_2$ (3:1) at 500 K. There is a clear uptake of $^{18}O_2$ at 900 K (shaded in pink). After the above oxygen dosage, no CO_2 was observed during CO titration, which rules out the possibility of the presence of any chemisorbed oxygen. During CO $+ ^{16}O_2$ reaction on the SM-Pd(111) surface, ample oxygen adsorption (shaded in yellow) and product 44 amu (CO_2) formation was observed, whereas the 46 amu ($CO^{18}O$) or 48 amu ($C^{18}O_2$) signal shows no change at all from the beginning of the reaction. This demonstrates that the subsurface oxygen does not diffuse out during the reaction, at least not below 900 K, and its direct participation in the reaction is ruled out; however, during the TPD experiment, subsurface oxygen desorbs between 1050 and 1200 K. Below 1000 K, subsurface oxygen stays within the subsurface and changes the electronic nature of the surface, but without taking part in the reaction. It is to be underscored that under practical driving conditions, the temperature of exhaust gases fluctuates between 473 and 873 K, and it hardly spikes momentarily to 1000 K; hence, the results presented here have direct relevance to TWC performance.
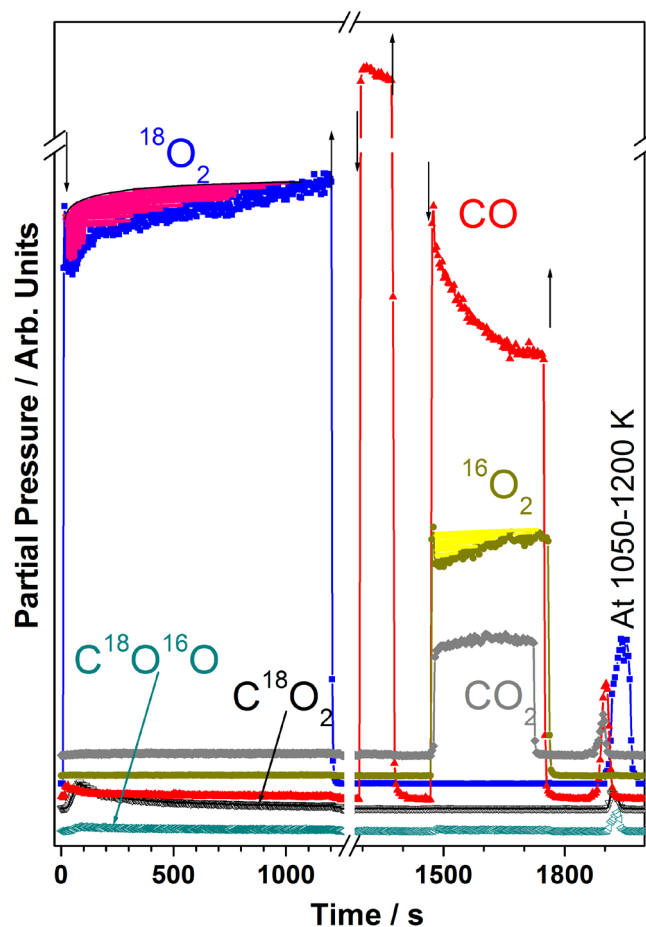
Figure 4.6 Time evolution of different mass signals (amu's 16, 18, 28, 32, 36, 44, 46, and 48) while dosing $^{18}O_2$ on Pd(111) at 900 K for 20 min, followed by CO titration at 525 K and then CO + $^{16}O_2$ (3:1 ratio) reaction at 500 K. TPD was performed at a heating rate of 10 K/s, after completing the reaction. Remarkably, no increase in 44 ($C^{16}O_2$), 46 ($C^{16}O^{18}O$), and 48 ($C^{18}O_2$) amu during CO titration indicated that the surface does not contain any chemisorbed oxygen. Again, during the CO + $^{16}O_2$ reaction, only the 44 amu signal is evolved without $C^{16}O^{18}O$ or $C^{18}O_2$. This demonstrates that oxygen in the subsurface (^{18}O) does not take part in the reaction. During TPD, subsurface oxygen desorbs between 1050 and 1200 K via molecular O_2 ($^{18}O_2$) and CO_x species with the ^{18}O isotope.

4.3.6. NO + H₂ + O₂ Reactions on SM-Pd(111) Surfaces.

The kinetic measurements were made with different NO + H_2 + zO_2 beam compositions (z = 1 −3) from 325 to 700 K on SM-Pd(111) surfaces, described in section 4.3.5. Our earlier studies on oxygen diffusion into the subsurfaces of Pd(111) modified the surface characteristics significantly [9, 26, 27]. This led to an altered catalytic activity toward CO oxidation, and the modified surfaces show

CO oxidation activity even at 900 K, whereas virgin Pd(111) shows no significant activity at ≥700 K.
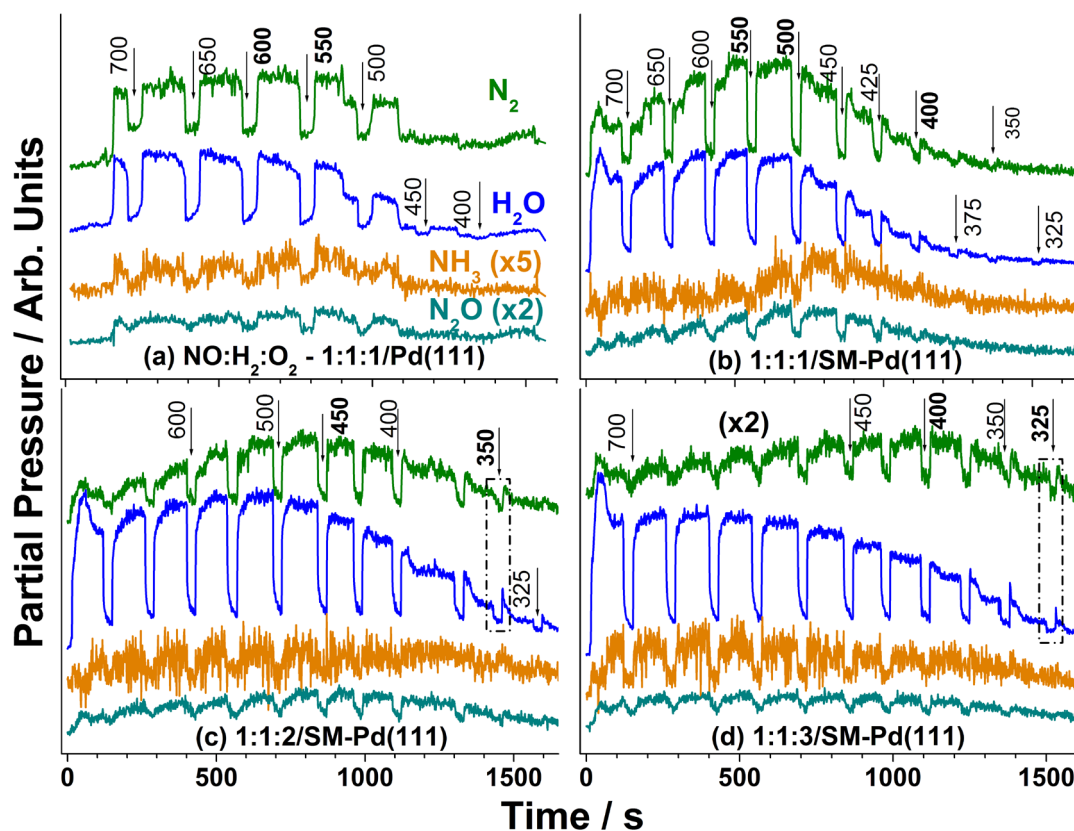
Figure 4.7. A comparison of NO $+H_2+O_2$ reactions performed on a) virgin Pd(111) and b–d) surface-modified Pd(111) between 700 and 325 K. Surface modification was performed by the first part of the oxygen-dosing experiment shown in Figure 1b, which induces low-temperature activity closer to ambient temperatures. Reactions were preformed from low to high temperature and vice versa, and no significant difference or hysteresis was observed between them. Indeed, the results shown in panel a were obtained by performing the modification from low to high temperature, but the plot is reversed for comparison. The y axis is the same in all panels.

We explored a similar aspect toward NO reduction with a NO + H_2 + O_2 mixture as a function of temperature and composition. These measurements were carried out on SM-Pd(111) surfaces (Figure 4.7), and the results obtained on virgin Pd(111) surfaces are compared with the above results.

The following points summarize the important findings of the results obtained

on SM-Pd(111) surfaces: 1) virgin Pd(111) surfaces show a NO decomposition onset at 450 K (as shown in Figure 1a) and N_2 and N-containing product formation activity at and above 500 K. A small amount of water production was observed under steady-state conditions above 400 K (Figure 4.7a). 2) A 1:1:1 ratio on SM-Pd(111) surfaces shows an extended activity with a characteristic change in the product pattern and enhanced activity. N_2 and N_2O were observed under steadystate conditions at and above 400 K. Only a marginal amount of NH_3 was observed. A small amount of water formation was observed under steady-state conditions up to 325 K. The enhancement in the overall rate of reaction is evident from the formation of a large quantity of products. However, the reaction maximum has shifted to 500–550 K (Figure 4.7b) from $550 - 600$ K on virgin Pd(111) surfaces (Figure 4.7a). 3) The 1:1:2 and 1:1:3 ratios on SM-Pd(111) surfaces show the maximum N_2 formation at 450 and 375–425 K, respectively. Further N_2 and H_2O production is extended up to 325 K in the latter case. In spite of a decreasing flux of NO (F_{NO}) from 33.3 (1:1:1) to 20% (1:1:3) with a concurrent increase in F_{O_2} to 60% at a 1:1:3 composition, a sustainable NO reduction observed close to ambient temperatures is appealing. We suggest this aspect may be carefully evaluated with supported Pd catalysts. In fact, Ueda et al.[10] and Lambert et al.[12] reported NO conversion between 10 and 50% at 323 to 373 K, respectively, on Pd/TiO_2 pre-calcined in air at 773 K, and it compares well with the present results. A concurrent increase in the partial pressure of H_2O and N_2 well above the steady-state pressure values at the point of shutter opening at 350 and 325 K (shown in the dashed box) demonstrates sustainable NO dissociation. Notably, the high-temperature activity at 700 K is reduced significantly in both cases compared to virgin Pd(111) surfaces (Figure 4.7a). In spite of the decreasing F_{NO}, N_2O formation was observed, but NH_3 production remains at marginal levels. In general, the selectivity of N_2, N_2O, and NH_3 is 76±5, 16±5, and 5±5%, respectively, at the reaction maximum. N_2 was produced exclusively 375 K on SM-Pd(111) with an O_2 - rich mixture. These catalytic runs were repeated at least fifty times to demonstrate the true influence of the modified Pd surface for NO decomposition at ambient temperatures. These observations also support our conclusions that subsurface oxygen does not participate in the reaction directly, which would otherwise make the lowtemperature activity disappear.

Figure 4.8 provides a quantitative measure of $NO + H_2 + O_2$ reaction on SM-Pd(111) surfaces through steady-state rates of all the products H_2O, N_2, NH_3

and N_2O and compared with that of the virgin Pd(111) surfaces. Even a glance at the results in Figure 4.8 demonstrates a clear broadening of catalytic activity toward ambient temperatures after surface modification. Important points to be highlighted are listed the following: (a) The steady-state NO reduction activity begins at 450 K on virgin Pd(111) surfaces; however, SM-Pd(111) surfaces exhibit rate values at 450 K that are closer to the rate maximum values. (b) No NO-reduction activity was observed at ≤450 K on Pd(111) virgin surfaces, whereas the rate measurements demonstrate a sustainable NO reduction activity at ≥325 K on SM-Pd(111) with all of the beam compositions, including O_2- rich compositions. (c) The rate of water formation increases linearly for any beam composition from 325 to 600 K on virgin and SM-Pd(111) surfaces. There is a marginal decrease in water production at 650 and 700 K, but they are comparable to the rate observed at 600 K. (d) Essentially, the steady-state rate values observed for N_2 and H_2O with the O_2- rich beam compositions at 325 K is relevant toward cold start deNO$_x$. Even though a large amount of gas phase oxygen is available, the above observation underscores that there may be much less or no O_2 adsorption occurring at low temperature conditions. (e) Although the SS rate of N_2 production decreases gradually at lower temperatures, an increasingly selective N_2 formation is observed on SM-Pd(111) surfaces. The above observation validates NO dissociation closer to room temperatures, without any NH_3 formation and in the presence of excess oxygen (z = 3). NO molecules compete strongly with oxygen for adsorption sites, and the surface may be dominated by an exclusive NO + H_2 reaction. (f) Although the rate maximum lies between 550 and 650 K for H_2O formation on SM-Pd(111) surfaces, the same for N_2 gradually shifts from 550 K toward 400 K with an increasing O_2 content. Selectivity of NH_3, N_2O, and N_2 products is 5 ± 5%, 16 ± 5%, and 76 ± 5%, respectively, at the optimum reaction temperature. Exclusively N_2 was produced at ≤375 K on SM-Pd(111) with O_2-rich composition. Although absolute activity has increased after surface modification, the product selectivity remains largely unchanged. (g) NH_3 production shows a complex trend. A 1:1:3 (1:1:2) composition shows the maximum (minimum) NH_3 production at temperatures > 425 K; a 1:1:1 composition shows a similar trend on Pd(111) and M-Pd(111), except for a shift to low temperatures with the latter. (h) N_2O production shows a similar trend as that of N_2.

It is to be noted that there are significant differences as well as similarities observed between the steady-state rates reported in Figure 4.8 and that of supported Pd-based deNO$_x$ catalysts [10 −13, 18].
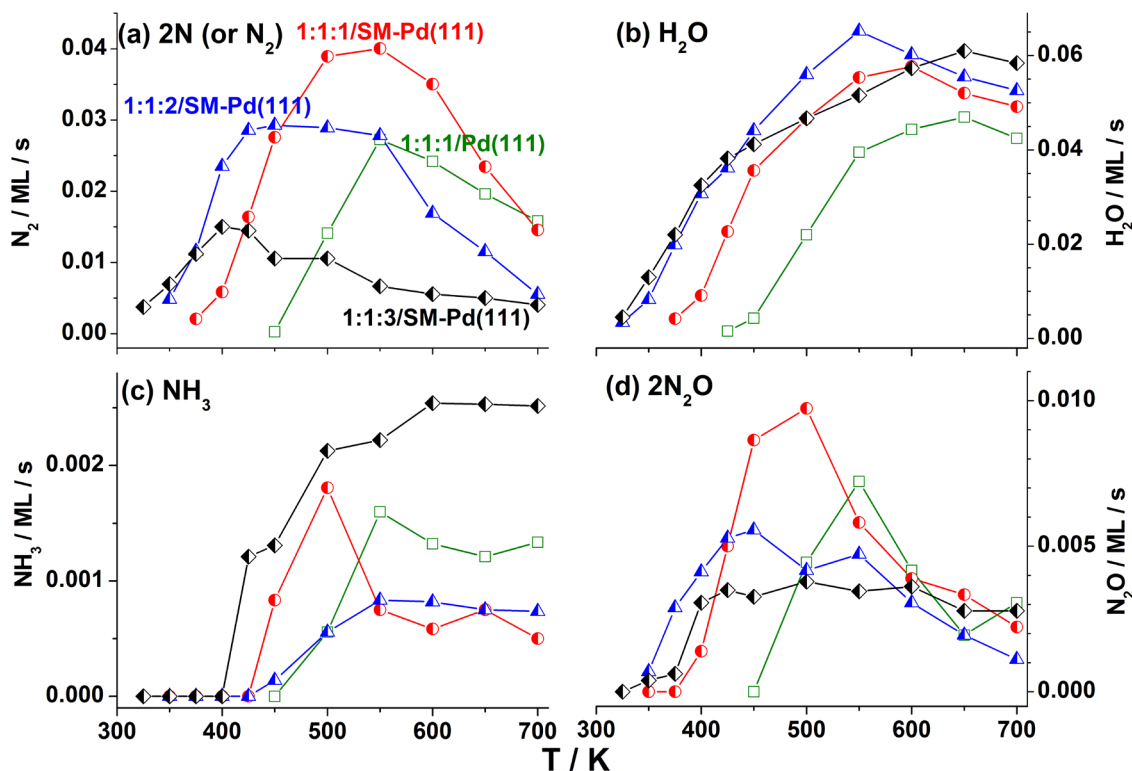
Figure 4.8. Steady-state rate obtained for (a) H$_2$O (b) N$_2$ (c) NH$_3$ (d) N$_2$O from NO + H$_2$ + O$_2$ reaction on SM-Pd(111) surfaces carried out with 1:1:z (z= 1 −3) compositions between 325 and 700 K. The steady-state rate measured on a virgin Pd(111) surface with a 1:1:1 composition is given for reference. Rate values higher (lower) than 0.005 ML/s were reproduced within a 5% (20%) error limit.

The low-temperature deNO$_x$ onset observed around 325 K is similar in the case of supported catalysts that were precalcined in air [10 −13] and the SM-Pd(111) single crystal system. Unlike the two reaction maxima that were observed on supported Pd catalysts [10 −13], only one reaction maximum was observed in our results on Pd(111). This underscores that the role of the support is significant at relatively high temperatures (≥450 K) and likely insignificant at low temperatures.

A careful analysis of the reactants adsorption under the steady state

conditions was made, and a representative result is shown in Figure 4.9.
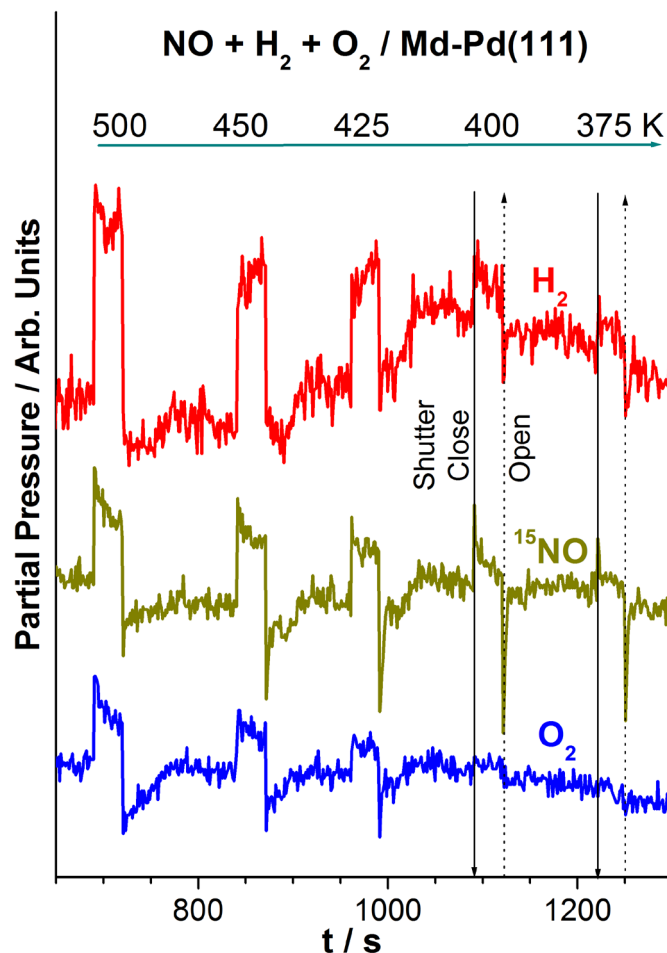
Figure 4.9. NO, H_2, and O_2 adsorption under steady-state reaction conditions observed for Figure 4.7a with a 1:1:1 composition between 500 and 375 K. Shutter close and open operations are shown by solid and dotted lines. Although sustainable NO and H_2 adsorption are observed at lower temperatures, simultaneous O_2 adsorption was not observed, suggesting the retardation of oxygen adsorption.

It shows the adsorption of reactants between 500 and 375 K for the results reported in Figure 4.7b with a 1:1:1 composition. The adsorption of all reactants could be observed between 425 and 500 K through beam oscillation measurements. Nonetheless, below 425 K, no O_2 adsorption could be observed, even though there was O_2 available in the molecular beam; whereas a sustainable NO and H_2

adsorption was observed at temperatures ≤425 K. Indeed, this demonstrates a change in the nature of SM-Pd(111) surfaces, which seems to hinder O_2 adsorption at low temperatures. One-to-one comparison of the reactants uptake at reaction maximum (500 K) and ≤400 K demonstrates a manifestation of exclusive NO + H_2 reaction in the latter (Figure 4.9).

Indeed, the above results explain in part why the contradicting results are observed for NO + H_2 + O_2 reaction on Pd on different supports, especially between 400 and 300 K [10 −12, 18]. A small amount of active Pd on any support material should exhibit surface defect sites, and oxygen diffusion into the subsurfaces is a good possibility, which will modify the surface. When reactions were measured on modified surfaces, it was expected that they would show significantly different activity from virgin catalysts.

4.3.7 Electronic Structure of SM-Pd(111) Surfaces.

To explore the nature of surface modification described in the earlier section, APPES measurements were made on exposing Pd surfaces to molecular oxygen at relevant pressures and temperature conditions. Figure 4.10 shows the representative APPES results recorded on clean Pd(111) surfaces at UHV (black trace) after surface modification and in the presence of oxygen at 10^{-5} mbar and 900 −750 K (red trace) and after evacuation to UHV at different temperatures (blue and green traces). APPES results were also shown at 0.07 mbar O_2 pressure and 675 K (violet trace). It is to be noted that the results presented in Figure 4.10 are from valence band (VB) photoemission with He I excitation radiation (hν = 21.2 eV). Our earlier studies with UVPES of systematic Cu oxidation to CuO through Cu_2O with the observation of associated changes in electronic structure at a pressure of 0.3 mbar O_2 at different temperatures presented in Chapter 3 is worth mentioning; it demonstrates the capability of Lab-APPES. More details about the Lab-APPES system are available Chapter 1 and in our earlier publications [33].

A clean Pd(111) surface at UHV shows a typical 4d doublet features with a strong Fermi level (E_F) intensity in the VB by UVPES. On introduction of O_2 and modification of Pd(111) surfaces at 1×10^{-5} mbar between 750 and 900 K a new broad feature at 6 eV is shown. An increase in the intensity of the first feature compared with the second feature in Pd 4d VB is also to be noted. In addition, a small but definite broadening of the VB feature occurs under the above conditions

(red trace in Figure 4.10), highlighting that a considerable change in VB occurs in the presence of oxygen. Even if the surface was exposed to oxygen at 10^{-5} mbar for a longer duration, no significant changes were observed in the VB. After recording the above spectra, oxygen was evacuated, and the VB spectrum was recorded at different temperatures; the results show that the broad feature at 6 eV remains there, but the VB features revert back to that of a clean Pd(111) surface.

The oxygen pressure was increased to 0.07 mbar, and the UVPES was recorded at a temperature of 675 K. There are significantly different changes occurring at high pressures. First and foremost is the observation of a sharp O 2p feature at 6.8 eV. What was observed as a broad feature at 10^{-5} mbar O_2 develops into the above feature, suggesting the precursor nature of the broad feature at 6 eV to the above oxide feature. This also demonstrates the broad feature is oxygen-related, and we attribute this to the oxygen in the immediate subsurfaces, which modify the surface, as shown in Figure 4.6. The second observation is a significant decrease in the E_F intensity, along with VB's shifting to higher BE (violet trace in Figure 4.10). The first VB feature at 1.2 eV merged significantly with the second feature. A significant amount of electron density decreases at E_F as well as with the first VB feature and a simultaneous increase in the O 2p feature at 6.8 eV highlights the surface oxide formation under the experimental conditions of 0.07 mbar O_2 and 675 K. Nonetheless, the E_F feature underscores that the oxide formation is restricted to the surface alone.

APPES results recorded with the Pd $3d_{5/2}$ core level at 0.07 mbar O_2 and 675 K is shown in the inset of Figure 4.10. A distinct Pd $3d_{5/2}$ peak was observed at 336.5 eV and is attributed to PdO. PdO is accompanied by metallic Pd and another feature at 335.0 and 335.7 eV, respectively. The latter feature is attributed to Pd_xO_y or Pd with oxygen in the immediate subsurfaces. In fact, the 2:1 intensity ratio observed between the 336.5 and 335.7 eV features is attributed to Pd with oxygen in the immediate subsurfaces [9, 43, 50]. It should be noted that UVPES is more surface-sensitive than XPS because of low and high probing depths, respectively, and hence, the buried subsurface feature is easily observed in XPS, even after PdO formation at 0.07 mbar O_2 at 675 K. Upon evacuation to UHV, the VB spectra revert back to the spectra shown for UHV at 600 K.

The above results highlight the presence of O atoms that are diffused into the subsurface layers as Pd_xO_y in the presence of oxygen and after evacuation to UHV.
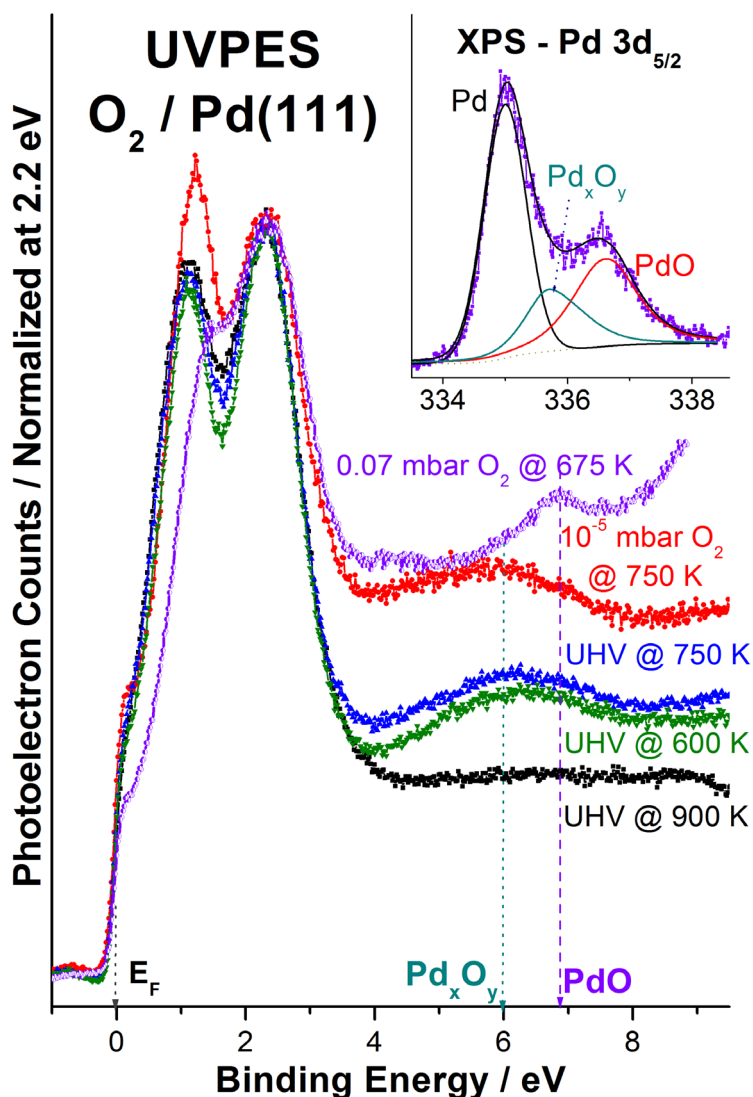
Figure 4.10. UVPES VB spectra recorded on a Pd(111) surface at different experimental conditions, mentioned on the spectral traces. All the spectra are normalized to the feature at BE = 2.3 eV. Broad and sharp peaks observed at 6 and 6.8 eV are attributed to Pd_xO_y and PdO features, respectively. The inset shows the XPS results recorded at 0.07 mbar O_2 pressure and 673 K for the Pd $3d_{5/2}$ core level, and the contribution from different states are deconvoluted.

Only a high temperature treatment above 1000 K, removes the subsurface oxygen, as shown in Figure 4.6. We speculate that this particular species is responsible for near-ambient temperature $deNO_x$ activity. Surface PdO formation

occurs exclusively in the presence of oxygen, at least under the conditions studied, and it decomposes on O_2 evacuation. APPES results reported at pressures higher than 0.1 mbar make the PdO layers relatively thick [9, 50, 51]. Nonetheless, that the presence of a reductant, such as H_2, reduces PdO to metallic Pd by consuming oxygen from PdO was aptly demonstrated by exposing the pre-oxidized Pd-based catalyst (by air calcination at 773 K) and then carrying out NO reduction with $NO + H_2 + O_2$ at 373 K [11]. Hence, even if PdO layers form as a result of O_2-rich real-world conditions, such as a high partial pressure of oxygen and high temperatures, the same can be reverted back to metallic Pd with oxygen in the subsurfaces when it is exposed to a reductant within the mixture of reactants. In fact, this is the specialty of Pd to withstand the oxygen-rich conditions and survive under lean burn conditions. However, oxygens in the subsurfaces are intact, unless they are exposed to temperatures higher than 1000 K.

The above observation and discussion demonstrates the applicability of surface modification to shift the catalysis regime toward ambient temperatures. In the above case, Pd surfaces are mildly oxidized as a result of the presence of oxygen in the subsurfaces or in the form of Pd_xO_y. Effectively, this makes the net surface nature cationic ($Pd^{\delta+}$). Elementary processes that occur on the SM-Pd(111) surfaces are shown in a drawing in Figure 4.11. The cationic character retards any process that requires electron donation from the surface; instead, it accelerates electron acceptance from chemisorption. Chemisorption and dissociation of molecular oxygen requires electron donation from the surface, which is retarded at lower temperatures on $Pd^{\delta+}$. In addition, the high electronegativity of oxygen hinders any oxygen dissociation. However, because of the polar nature of NO, chemisorption followed by dissociation occurs readily on $Pd^{\delta+}$. It also should be remembered that molecular NO adsorption occurs below 400 K on clean Pd(111) surfaces [24] as a result of the back-donation of electrons from the surface. On cationic surfaces, the back donation is likely to be absent, which leads to dissociation of NO molecules and, hence, low-temperature activity. We believe that surface modification with electronegative [26, 27] (such as oxygen) or electropositive (such as carbon, hydrogen) atoms [28, 52] in the subsurfaces could influence many other reactions, and it is worth exploring.
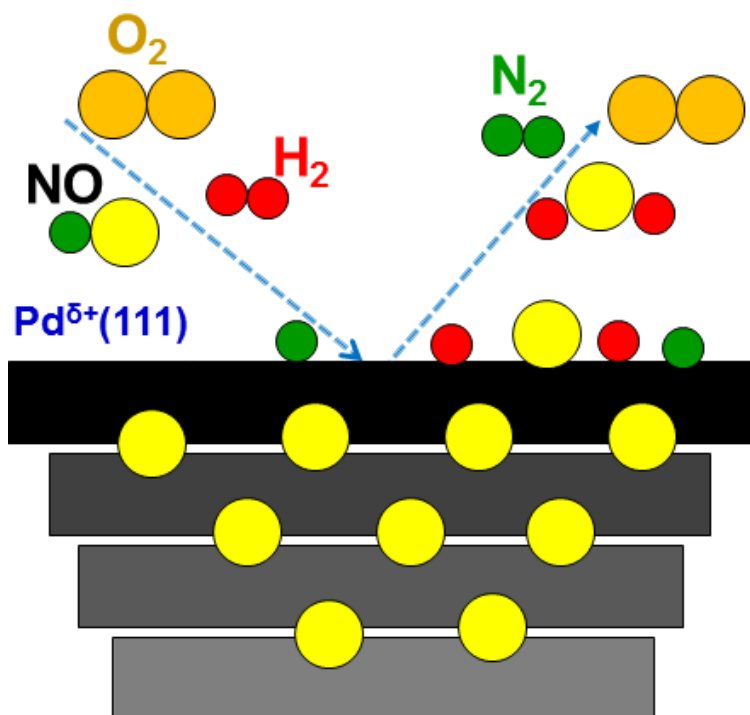
Figure 4.11. Surface modification is indicated by graded black to gray color with oxygen (yellow circles) in the subsurfaces. Particularly O_2 chemisorption and dissociation (orange solid circle) is hindered or at least minimized, which enhances NO dissociation and deNO$_x$ activity around ambient temperatures.

§ 4.4 Conclusions

A possibility of shifting the catalysis regime toward ambient temperatures is demonstrated through surface modification for NO reduction on Pd(111) surfaces. Virgin and modified Pd(111) surfaces were evaluated for NO reduction with technically relevant temperatures and NO + H_2 + O_2 compositions. Compared with virgin surfaces, modified Pd(111) demonstrates not only a 50% increase in deNO$_x$ activity, but also shifts the deNO$_x$ regime toward ambient temperatures. Even though a large amount of oxygen is present in the gas phase, effectively, the NO + H_2 reaction occurs on the modified surfaces, demonstrating the retardation of molecular oxygen adsorption below 400 K. A careful analysis of NO + H_2 and NO + H_2 + O_2 reveals the adsorption and utilization of oxygen from molecular oxygen toward oxidation of hydrogen is very low at temperatures below 500 K. We believe that the cationic character of modified Pd surfaces hinders oxygen

adsorption because of a significantly low electron donation capability, which may be probed by other relevant analytical techniques.

An important aspect of the present work to be underscored is the permanence of oxygen atoms diffused into the subsurfaces and, hence, Pd_xO_y. As long as the temperature does not increase above 1000 K, the above feature is stable and exhibits its influence in demonstrating near-ambient temperature $deNO_x$ catalytic activity. Further, surface oxide that forms under oxygen-rich conditions either decomposes or the oxygen in the surface oxide is consumed under fuel-rich or reductive conditions. This exposes the modified surfaces, and hence, the low-temperature activity reverts. In fact, it is highly desirable to explore the modified surfaces for different reduction and oxidation reactions.

§ 4.4 References

[1]. P. G. Savva, C. N. Costa, *Catal. Rev. - Sci. Eng.* **2011**, *53*, 91-151.

[2]. Z. Liu, J. Li, S. I. Woo, *Energy Environ. Sci.* **2012**, *5*, 8799-8814.

[3]. G. A. Deluga, J. R. Salge, L. D. Schmidt, X. E. Verykios, *Science* **2004**, *303*, 993-997.

[4]. S. Tagliaferri, R. A. Koppel, A. Baiker, *Stud. Surf. Sci. Catal.* **1998**, *116*, 61-71.

[5]. A. Obuchi, S. Naito, T. Onishi, K. Tamaru, *Surf. Sci.* **1982**, *122*, 235-255.

[6]. Y. Ma, T. Matsushima, *J. Phys. Chem. B* **2005**, *109*, 1256-1261.

[7]. C. A. de Wolf, B. E. Nieuwenhuys, *Surf. Sci.* **2000**, *469*, 196-203.

[8]. H. Conrad, G. Ertl, J. Kueppers, E. E. Latta, *Surf. Sci.* **1977**, *65*, 245-260.

[9]. K. Roy, C. S. Gopinath, *ChemCatChem* **2014**, *6*, 531-537.

[10]. A. Ueda, T. Nakao, M. Azuma, T. Kobayashi, *Catal. Today* **1998**, *45*, 135-138.

[11]. B. Wen, *Fuel* **2002**, *81*, 1841-1846.

[12]. N. Macleod, R. Cropley, R. M. Lambert, *Catal. Lett.* **2003**, *86*, 69-75.

[13]. N. Macleod, R. M. Lambert, *Catal. Lett.* **2003**, *90*, 111-115.

[14]. Y.-W. Lee, E. Gulari, *Catal. Commun.* **2004**, *5*, 499-503.

[15]. N. Macleod, R. Cropley, J. M. Keel, R. M. Lambert, *J. Catal.* **2004**, *221*, 20-31.

[16]. J.-B. Yang, O.-Z. Fu, D.-Y. Wu, S.-D. Wang, *Appl. Catal., B* **2004**, *49*, 61-65.

[17]. G. L. Chiarello, D. Ferri, J.-D. Grunwaldt, L. Forni, A. Baiker, *J. Catal.* **2007**, *252*, 137-147.

[18]. (a) F. Dhainaut, S. Pietrzyk, P. Granger, *Top. Catal.* **2007**, *42/43*, 135-141. (b) Y. Reneme, F. Dhainaut, P. Granger, *Appl. Catal., B* **2012**, *111-112*, 424-432. (c) C. Dujardin, I. Twagirashema, P. Granger, *J. Phys. Chem. C* **2008**, *112*, 17183-17192.

[19]. E. M. Holmgreen, M. M. Yung, U. S. Ozkan, *J. Mol. Catal. A: Chem.* **2007**, *270*, 101-111.

[20]. M. Leicht, F. J. P. Schott, M. Bruns, S. Kureti, *Appl. Catal., B* **2012**, *117-118*, 275-282.

[21]. W. C. Hecker, A. T. Bell, *J. Catal.* **1985**, *92*, 247-259.

[22]. R. Burch, T. C. Watling, *Catal. Lett.* **1996**, *37*, 51-55.

[23]. K. Thirunavukkarasu, C. S. Gopinath, *Catal. Lett.* **2007**, *119*, 50-58.

[24]. K. Thirunavukkarasu, K. Thirumoorthy, J. Libuda, C. S. Gopinath, *J. Phys. Chem. B* **2005**, *109*, 13283-13290.

[25]. K. Thirunavukkarasu, K. Thirumoorthy, J. Libuda, C. S. Gopinath, *J. Phys. Chem. B* **2005**, *109*, 13272-13282.

[26]. C. S. Gopinath, K. Thirunavukkarasu, S. Nagarajan, *Chem. - Asian J.* **2009**, *4*, 74-80.

[27]. S. Nagarajan, K. Thirunavukkarasu, C. S. Gopinath, *J. Phys. Chem. C* **2009**, *113*, 7385-7397.

[28]. S. Nagarajan, K. Thirunavukkarasu, C. S. Gopinath, J. Counsell, L. Gilbert, M. Bowker, *J. Phys. Chem. C* **2009**, *113*, 9814-9819.

[29]. S. Nagarajan, C. S. Gopinath, *J. Indian Inst. Sci.* **2010**, *90*, 245-260.

[30]. S. Nagarajan, K. Thirunavukkarasu, C. S. Gopinath, *J. Phys. Chem. C* **2011**, *115*, 21299-21310.

[31]. S. Nagarajan, K. Thirunavukkarasu, C. S. Gopinath, S. D. Prasad, *J. Phys. Chem. C* **2011**, *115*, 15487-15495.

[32]. M. Bowker, J. Counsell, K. El-Abiary, L. Gilbert, C. Morgan, S. Nagarajan, C. S. Gopinath, *J. Phys. Chem. C* **2010**, *114*, 5060-5067.

[33]. (a) K. Roy, C. P. Vinod, C. S. Gopinath, *J. Phys. Chem. C* **2013**, *117*, 4717-4726. (b) K. Roy, C. S. Gopinath, *Anal. Chem.* **2014**, *86*, 3683-3687.

[34]. (a) V. Bustos, C. S. Gopinath, R. Unac, F. Zaera, G. Zgrablich, *J. Chem. Phys.* **2001**, *114*, 10927-10931. (b) F. Zaera, C. S. Gopinath, *J. Mol. Catal. A: Chem.* **2001**, *167*, 23-31.

[35]. F. Zaera, S. Wehner, C. S. Gopinath, J. L. Sales, V. Gargiulo, G. Zgrablich, *J. Phys. Chem. B* **2001**, *105*, 7771-7774.

[36]. (a) C. S. Gopinath, F. Zaera, *J. Catal.* **2001**, *200*, 270-287. (b) F. Zaera, C. S. Gopinath, *J. Chem. Phys.* **2002**, *116*, 1128-1136.

[37]. C. S. Gopinath, F. Zaera, *J. Phys. Chem. B* **2000**, *104*, 3194-3203.

[38]. V. Johanek, S. Schauermann, M. Laurin, C. S. Gopinath, J. Libuda, H. J. Freund, *J. Phys. Chem. B* **2004**, *108*, 14244-14254.

[39]. B. Klotzer, K. Hayek, C. Konvicka, E. Lundgren, P. Varga, *Surf. Sci.* **2001**, *482-485*, 237-242.

[40]. A. F. Lee, J. N. Naughton, Z. Liu, K. Wilson, *ACS Catal.* **2012**, *2*, 2235-2241.

[41]. D. Zemlyanov, B. Kloetzer, H. Gabasch, A. Smeltz, F. H. Ribeiro, S. Zafeiratos, D. Teschner, P. Schnoerch, E. Vass, M. Haevecker, A. Knop-Gericke, R. Schloegl, *Top. Catal.* **2013**, *56*, 885-895.

[42]. H. Gabasch, A. Knop-Gericke, R. Schlögl, M. Borasio, C. Weilach, G. Rupprechter, S. Penner, B. Jenewein, K. Hayek, B. Kloetzer, *Phys. Chem. Chem. Phys.* **2007**, *9*, 533-540.

[43]. H. Gabasch, W. Unterberger, K. Hayek, B. Kloetzer, E. Kleimenov, D. Teschner, S. Zafeiratos, M. Haevecker, A. Knop-Gericke, R. Schloegl, J. Han, F. H. Ribeiro, B. Aszalos-Kiss, T. Curtin, D. Zemlyanov, *Surf. Sci.* **2006**, *600*, 2980-2989.

[44]. F. P. Leisenberger, G. Koller, M. Sock, S. Surnev, M. G. Ramsey, F. P.

Netzer, B. Klotzer, K. Hayek, *Surf. Sci.* **2000**, *445*, 380-393.

[45]. M. K. Rose, A. Borg, J. C. Dunphy, T. Mitsui, D. F. Ogletree, M. Salmeron, *Surf. Sci.* **2004**, *561*, 69-78.

[46]. A. I. Titkov, A. N. Salanov, S. V. Koscheev, A. I. Boronin, *React. Kinet. Catal. Lett.* **2005**, *86*, 371-379.

[47]. J. Han, D. Y. Zemlyanov, F. H. Ribeiro, *Surf. Sci.* **2006**, *600*, 2752-2761.

[48]. J. Han, D. Y. Zemlyanov, F. H. Ribeiro, *Surf. Sci.* **2006**, *600*, 2730-2744.

[49]. H. H. Kan, R. B. Shumbera, J. F. Weaver, *Surf. Sci.* **2008**, *602*, 1337-1346.

[50]. G. Ketteler, D. F. Ogletree, H. Bluhm, H. Liu, E. L. D. Hebenstreit, M. Salmeron, *J. Am. Chem. Soc.* **2005**, *127*, 18269-18273.

[51]. D. Teschner, A. Pestryakov, E. Kleimenov, M. Haevecker, H. Bluhm, H. Sauer, A. Knop-Gericke, R. Schloegl, *J. Catal.* **2005**, *230*, 186-194.

[52]. M. Armbruester, M. Behrens, F. Cinquini, K. Foettinger, Y. Grin, A. Haghofer, B. Kloetzer, A. Knop-Gericke, H. Lorenz, A. Ota, S. Penner, J. Prinz, C. Rameshan, Z. Revay, D. Rosenthal, G. Rupprechter, P. Sautet, R. Schloegl, L. Shao, L. Szentmiklosi, D. Teschner, D. Torres, R. Wagner, R. Widmer, G. Wowsnick, *ChemCatChem* **2012**, *4*, 1048-1063.

Chapter 5

CO Oxidation at Near Ambient Temperatures on Modified Palladium Surfaces
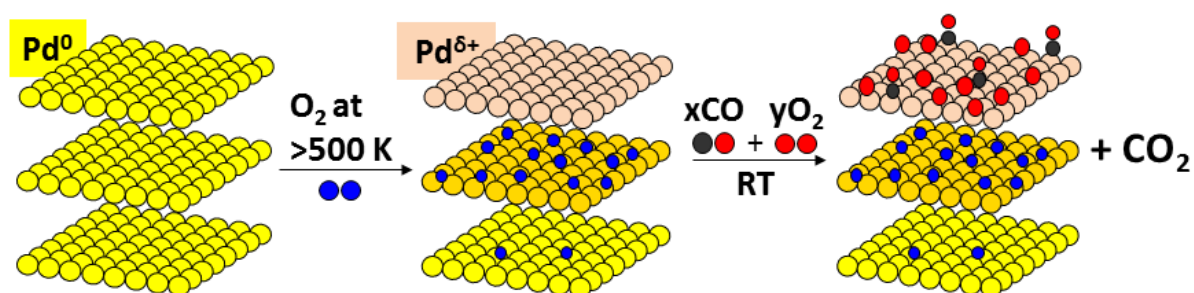
Part of the work presented in Chapter 5 has been published, and the publication detail is:

An attempt has been made to shift the temperature regime of oxidation catalysis towards ambient temperatures by employing surface modification (SM) as a handle. A systematic SM of Pd(111) was carried out by O-atom diffusion into the subsurfaces. Virgin and modified Pd(111) catalyst was evaluated for CO oxidation. Typical CO poisoning observed on virgin surfaces was partially lifted and ambient CO oxidation observed on modified surfaces. CO oxidation was followed by molecular beam method, and near-ambient pressure (NAP) photoelectron spectroscopy at different pressure regimes. UV valence band spectral analysis of SM and $CO+O_2$ reaction on modified Pd(111) surfaces under NAP conditions demonstrates the changes in electronic structure of surfaces with a change in surface potential by 0.35 eV and directly probes the CO_2 formation under reaction conditions. Supported metal catalysts may be subjected to SM and evaluated for shift in catalysis regime for many different reactions.

§ 5.1 Introduction

Why any heterogeneous catalyst should work only within a set of boundary conditions? Why not the boundary conditions can be altered? Catalytic activity depends on the nature of ligands surrounding the central metal ion in homogeneous catalysis; however, there is no such handle in heterogeneous catalysts. However, there are many different catalysts available for any given reactions, and they work under considerably different conditions. Given the above fact, why not a suitable surface modification (SM) of a heterogeneous catalyst can provide a handle to influence the catalysis regime. In fact, the elementary steps involved in catalysis, such as adsorption, dissociation, desorption, involves bond-making or bond-breaking and they depend on the electronic character of the catalyst surfaces. If the electronic character of a solid catalyst can be altered through SM, we believe that catalysis regime can also be changed. Present manuscript tried to attempt to shift the catalysis regime of a well-studied CO oxidation on a well-known catalyst (Pd) surfaces, before and after SM.

Carbon monoxide (CO) oxidation is a very important reaction from the environmental point of view, and well-studied too. However, robust and sustainable CO oxidation catalysts are needed for many ambient temperature applications, such as to improve the quality of life. One of the most widely employed CO oxidation catalysts is Pd supported on oxide employed in automotive TWC converters. However, like other noble metals, Pd is also not effective for CO oxidation below 400 K. CO chemisorbs very strongly and poisons the noble metal surfaces, including Pd. Although gold nanoparticles show promise for ambient and sub-ambient temperature CO oxidation activity [1], it is not sustainable, and particularly it is not suitable for the applications those work under varied temperatures, such as TWC. Another common issue with Pd (and many other metals) is its high dissoluting nature to some common atomic species like C, H and O [2-4]. In the reactive environment the inevitable dissolution of some of the abundant moieties, such as oxygen, plays some role in Pd catalyzed reactions, which is not explored yet. On one hand, this is a problematic issue, but on the other hand an opportunistic window exists to tune the catalytic activity of Pd. Can we make use of soluble nature of some of the reactant species, such as oxygen, to modify the surface electronically and induce the catalytic activity at relatively low temperatures? Indeed atomic O diffusion into Pd subsurfaces has

been observed at and above 500 K by many groups, and the extent of O diffusion increases linearly up to 900 K, though surface O_2 desorption maximum is $\backsim$750 K for Pd(111) surfaces [5-11].

Herein, we report the ambient oxidation of CO using oxygen on the surface modified Pd(111) (SM-Pd). The role of subsurface O in CO oxidation with oxygen on Pd(111) catalyst has been probed by the molecular beam instrument (MBI) and the ambient pressure photoelectron spectroscopy (APPES). We demonstrate that the presence of O atoms present in the subsurface of Pd(111) modifies the electronic structure of the surface of Pd(111), and enhances the catalytic activity of the Pd(111) towards low temperature CO oxidation. Further subsurface oxygen was not consumed in the CO oxidation; it only alters the electronic nature of the surface. In addition to the typical catalytic activity above 400 K, we show the sustainable CO oxidation between 300 and 400 K on SM-Pd at moderate vacuum in MBI and NAP conditions in APPES.

§ 5.2 Experimental Section

The details about the MBI, APPES set up has been given. Maximum SM could be observed with oxygen dosing on Pd(111) at 900 K with oxygen flux (F_{O2}) =0.5 ML/s. Subsurface oxygen coverage ($\theta_{O\text{-sub}}$) increases linearly, and between 50 and 60 minute of O_2 pre-dosing the $\theta_{O\text{-sub}}$ reached the maximum value around 0.45–0.5 ML, and no further increase in $\theta_{O\text{-sub}}$ could be observed. SM is fully reversible and O_2 desorption occurs by simple heating to 1100-1200 K from the subsurface layers of $\backsim$2 nm [5-11]. All reaction results reported are after SM with oxygen dosing for 50 min, unless stated. Blank experiments (such as O_2 and CO adsorption at different temperatures while following all relevant mass species) were measured to confirm that there is no background contribution, such as production of CO_2 or H_2O. Though the chamber flushing effect and hence changes in partial pressure of reactants has been observed in some experiments; however, it does not alter the results reported here, since the total flux of reactants on the surface remains unaffected.

O$_2$ interaction and CO + O_2 reaction was systematically measured with Pd(111) surfaces in the APPES set up. The maximum pressure limit for XPS in this system is 1 or 0.5 mbar with the analyzer cone aperture of 0.8 or 1.2 mm, respectively. The UVPES experiments can be performed up to 0.3 mbar with

1.2 mm aperture cone [19]. The sample is kept at a distance of 1.5 mm, which is higher than the cone aperture; all APPES experiments reported herewith were carried out with the cone aperture of 1.2 mm and at a distance of 1.5 mm.

§ 5.3 Results and Discussion

5.3.1 Molecular Beam Studies

First we present the results obtained from MBI. Figure 5.1 shows the CO_2 production between 300 and 525 K with $CO:O_2$ (1:4) ratio on virgin and SM-Pd surfaces. In the steady state (SS) the $CO + O_2$ beam was deliberately blocked and unblocked several times by closing and opening the shutter, respectively, to measure the SS rate of the reaction at different temperatures. During beam blocking a decrease (increase) in CO_2 (reactants) partial pressure observed was due to the stopping of reaction, which directly gives the reaction rate. On clean Pd(111) surface the CO_2 formation activity begins at 375 K; except CO_2 production in the transient state (TS) on clean Pd(111) at 300 K, no sustainable catalytic activity was observed below 375 K, and it is in good agreement with the earlier results [11-15]. The maximum CO_2 production was observed around 425 K. In contrast, SM-Pd exhibits CO oxidation activity from 300 K and above (Fig. 5.1b).

Few important points from Figure 5.1 are worth highlighting here:

(a) After SM the oxidation catalytic activity broadened towards lower temperatures, to at least, around 300 K; measurement at 273 K, shows no CO_2 production on SM-Pd. Oxidation activity around 500 K is similar on both surfaces. (b) Although CO uptake in the TS is similar on virgin and SM-Pd, sustainable CO_2 formation is fully supported by CO consumption under SS on the latter. A marked increase in CO partial pressure for beam oscillation in SS at 300 K demonstrates this on SM-Pd. Due to high oxygen content and noise level, oxygen uptake is not discernible. (c) A detectable CO desorption was observed when the temperature was ramped from 325 to 350, 350 to 375, and 375 to 400 K on virgin Pd(111) surfaces (indicated by rectangular boxes in Fig. 5.1a). However, the extent of similar CO desorption was at average noise level on SM-Pd when the temperature was raised from 300 to 325 K and 325 to 350 K; nonetheless, temperature ramping is accompanied with CO_2 desorption, well above the SS level (indicated by rectangular boxes in Fig. 5.1b), indeed highlights the ambient

temperature catalytic activity on SM-Pd. This particular observation hints the CO-poisoning is, at least, partially lifted on SM-Pd.
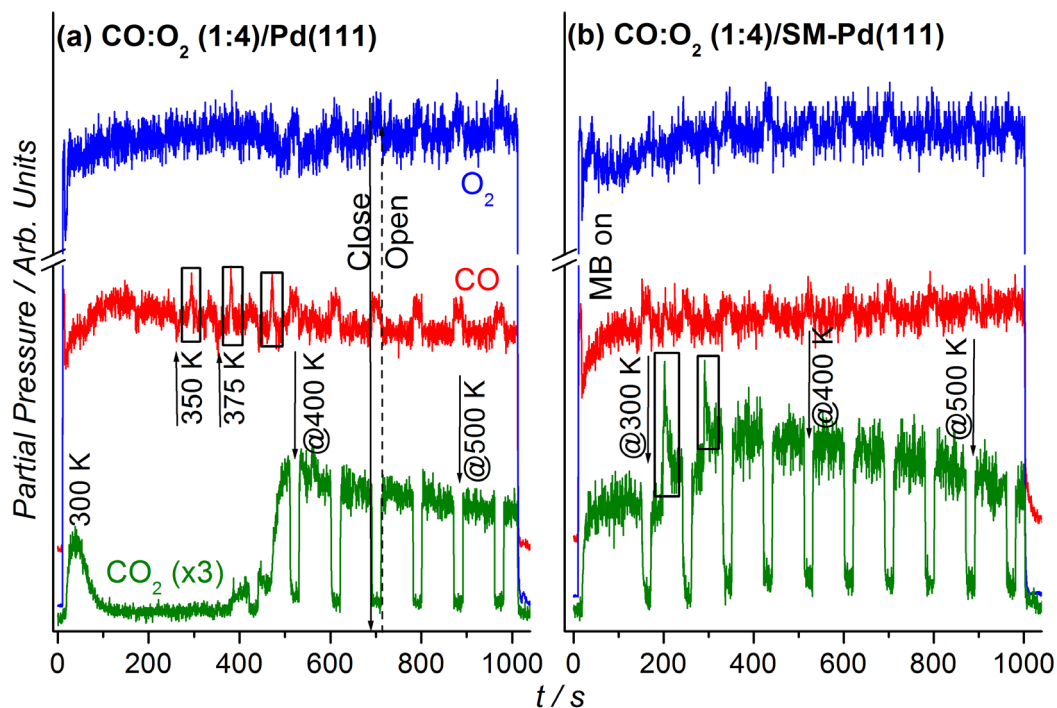
Figure 5.1 The time evolution of reactants and product partial pressure on (a) virgin Pd(111), and (b) SM-Pd between 300 and 525 K with $CO:O_2$ (1:4) ratio. CO oxidation started at 300 K, continued up to 525 K and each time the temperature ramped up by 25 K. Steady state (SS) rate was measured by beam oscillation in the SS. Rectangular boxes in panels a and b indicating the desorption of CO and CO_2, respectively.

Figure 5.2 shows the SS rate of CO oxidation reactions described in Figure 5.1 for the $CO:O_2$ ratios between 7:1 to 1:7 on virgin and SM-Pd surfaces. This set of results demonstrates the catalytic oxidation activity at ambient temperatures and above. Oxidation activity barely starts at 375 K on virgin surfaces; whereas, it starts at 300 K after SM with any ratio of $CO:O_2$. The maximum CO oxidation was observed at increasingly higher temperature with CO-rich $CO:O_2$ compositions; whereas this regime broadened and shifted to lower temperatures by about 75-150 K after SM. The rate maximum (R_{max}) generally observed between 450 and 525 K on the clean Pd(111) shifts to the lower temperatures after SM for a given beam composition. For eg. R_{max} of 4:1 (1:4) $CO:O_2$ composition shifts from 525 K (475 K) on the clean Pd(111) to 400 K (375 K) after 50 min of O_2 pre-dosing. This highlights the effectiveness of the SM towards O_2-lean as well as O_2-rich $CO:O_2$ ratios. As expected the low flux component decides the overall rate [16].

Results presented above are after optimum SM , and smaller extent of SM linearly increases the R_{max} and shifts the catalysis regime. For example, Pd(111) pre-dosed with oxygen for lesser than 50 min. shows the R_{max} higher than reported in Fig. 5.2b, but lower than that of virgin surfaces.
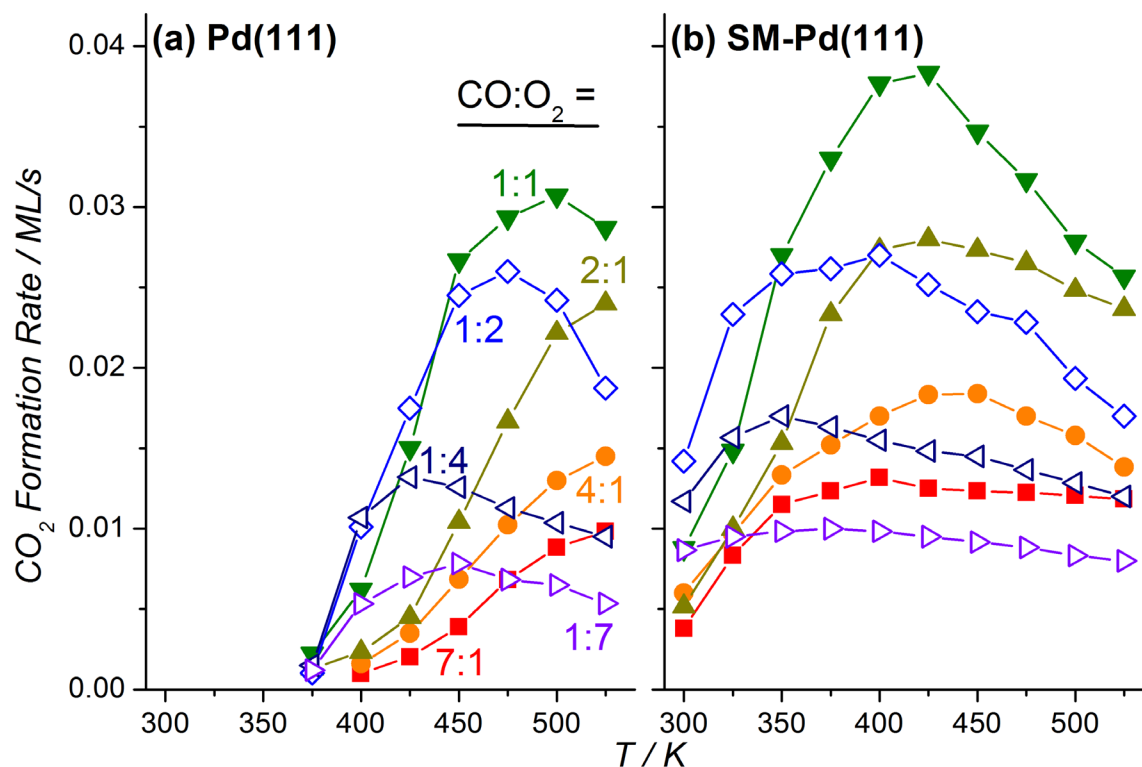
Figure 5.2 The steady state rate measured for the reactions described in Figure 5.1 for various $CO:O_2$ ratios between 7:1 and 1:7 measured on (a) virgin Pd(111) and (b) SM-Pd(111) surfaces. Note a significant increase in oxidation capacity at low temperatures with all the $CO:O_2$ ratios on the SM-Pd(111) compared to the clean Pd(111) surfaces. Comparable rates are observed at high temperatures on virgin and SM-Pd surfaces.

Our experiments show that oxidation catalytic activity is not only extended to lower temperature, but also sustainable. Selected measurement at 325 K has been carried out for 1 h, and Figure 5.3 shows the time evolution of CO_2 at 325 K with $CO:O_2$ (1:7) on SM-Pd. The reaction was continued for 1 h to demonstrate the sustainability of the reaction as well as the non-consumption of oxygen from sub-surfaces on the SM-Pd. An unambiguous CO adsorption was observed throughout the reaction time period. Although a clear O_2 adsorption cannot be seen, due to high intensity of O_2-flux, minor changes can be observed for the beam oscillations. The $CO+O_2$ beam was deliberately blocked 1 min for every 5 min. to show the

sustainability as well as to measure the rate of the reaction, which is nearly the same within the experimental error limit of 5 %. It is to be noted that the subsurface oxygen only influences the surface electronic properties and in turn the catalytic activity of the SM-Pd, and is not consumed by the CO oxidation. Indeed the reaction could not have been sustained even for two minutes if the subsurface O atoms were to be consumed for the CO-oxidation. The sustainability of CO_2 production is shown is Figure 5.4. No diffusion of atomic O into subsurfaces occur <500 K rules out the exchange of O between the surface and the subsurface <500 K [6,7,10,11].
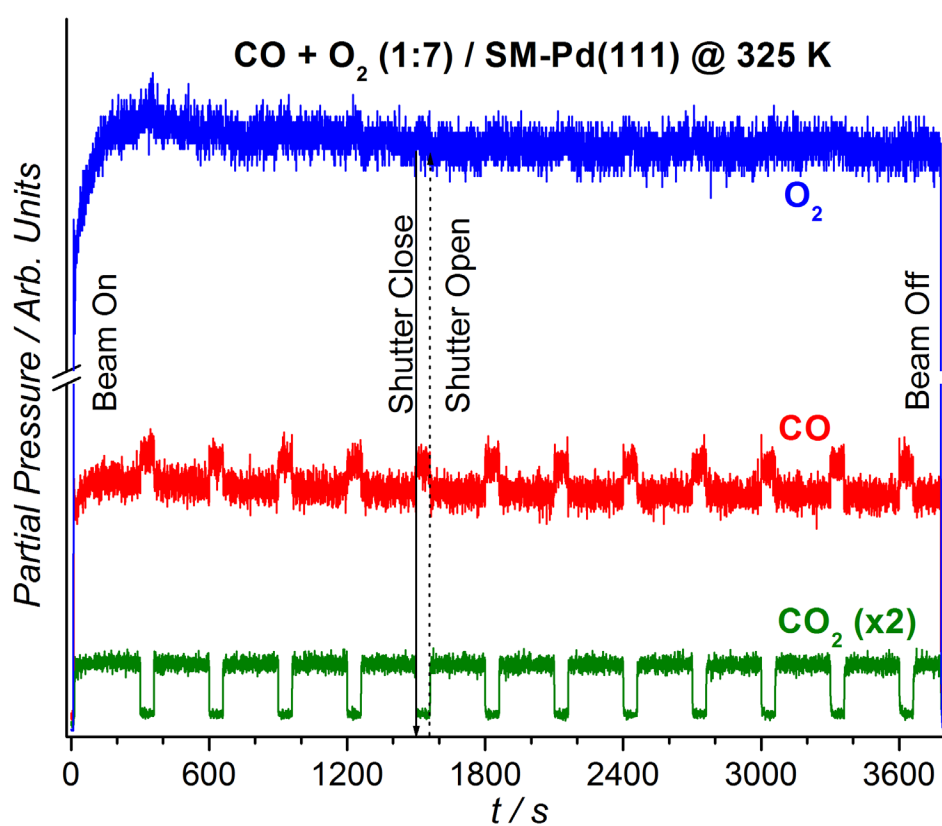
Figure 5.3 CO oxidation measured with oxygen rich $CO+O_2$ (1:7) composition on SM-Pd(111)-surface at 325 K for 1 h to demonstrates the sustainability of the reaction as well as non-consumption of subsurface oxygen for reaction.
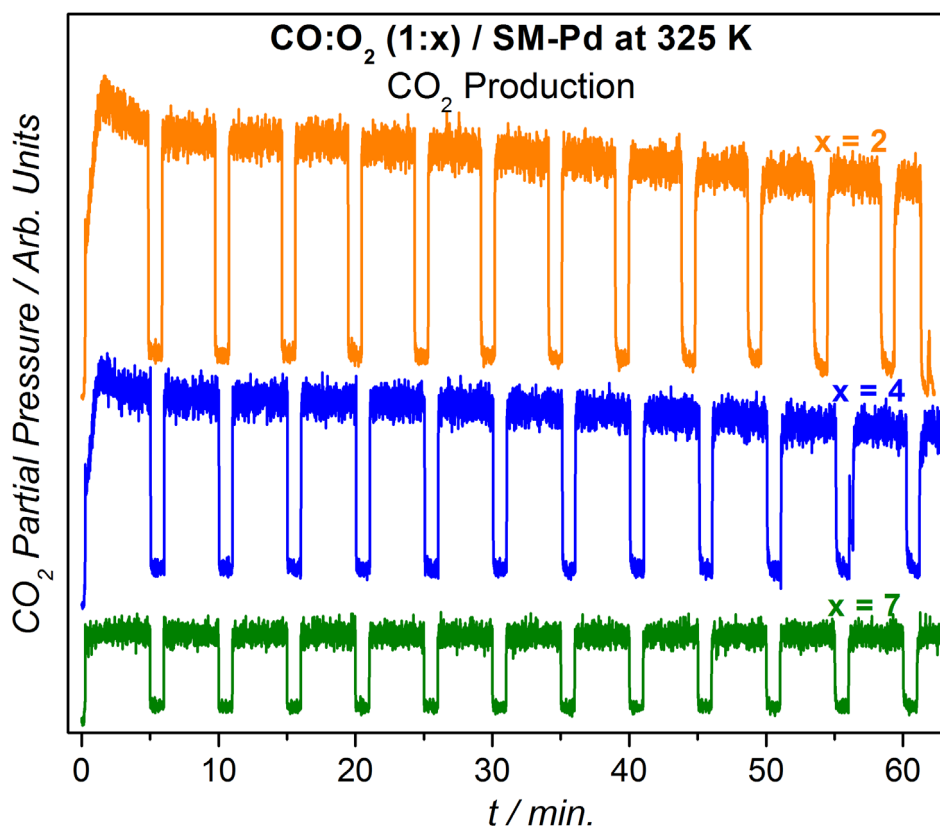
Figure 5.4 Time evolution of CO_2 at 325 K with different $CO:O_2$ (1:x) ratios on SM-Pd. Reaction continued for 1 h to demonstrate the sustainability of the reaction as well as the non-consumption of oxygen from sub-surfaces on the SM Pd(111) with increasingly O_2-rich compositions. The rate of reaction for a given reactants composition is nearly the same within the experimental error limit of 5%.

While analysing the adsorption trend of reactants on the SM-Pd under the SS conditions, genesis of the above activity was uncovered. It is evident that there is sustainable CO adsorption under SS at 300 K, irrespective of the $CO:O_2$ compositions (Figure 5.5). For beam oscillations under the SS conditions, there is a good change in CO, O_2 and CO_2 partial pressure demonstrate that the activity is due to intrinsic nature of the SM-Pd. Indeed it is surprising to note the oxidation activity on SM-Pd at 300 K even with CO-rich compositions (Figure 5.5), which is in direct contrast to that of the virgin Pd(111) surfaces [11,14-16].
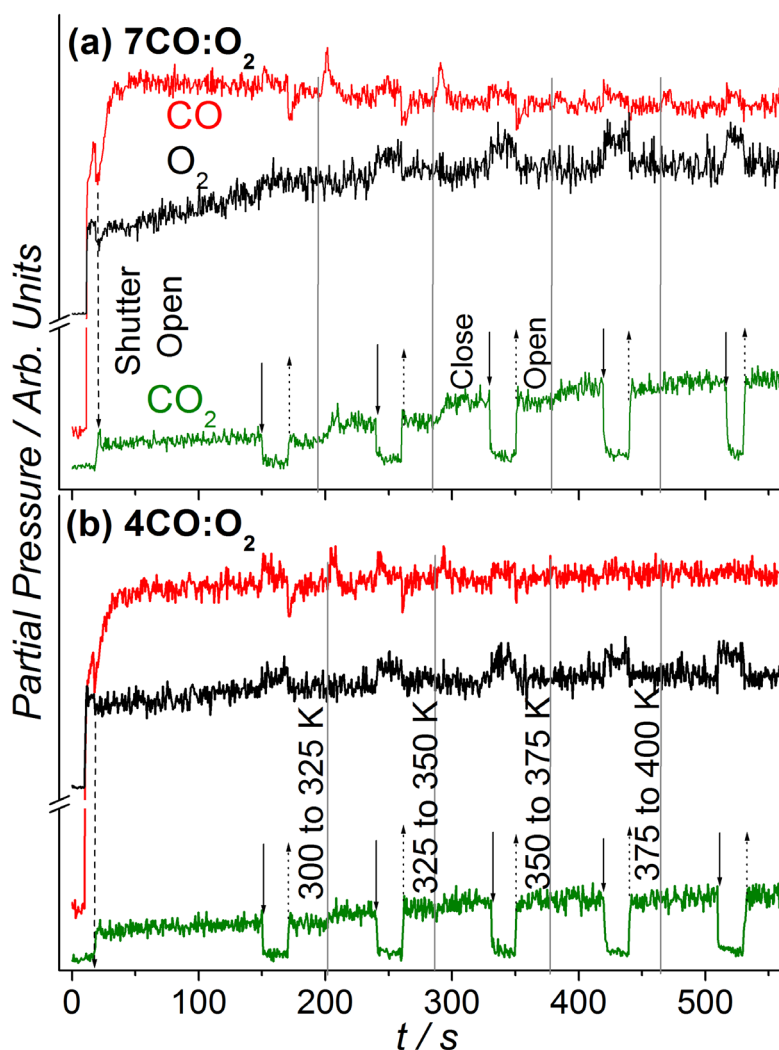
Figure 5.5 Time evolution of reactants and product partial pressure between 300 and 400 K with different $CO:O_2$ ratios (a) 7:1, and (b) 4:1on SM-Pd. A clear CO uptake observed in SS for beam oscillations, under the above conditions, highlights the reactive CO adsorption, irrespective of the $CO:O_2$ ratio and temperature. On ramping the temperature from 300 to 325 K and 325 to 350 K (vertical lines) exhibits CO desorption as well as high rate of CO_2 production indicating the surface was partially poisoned with CO.

Significant CO adsorption observed in the SS with the O_2-rich compositions (Fig. 5.1a) also highlights that the reactivity of the SM-Pd has changed dramatically. A careful analysis of the experimental data in Fig. 5.5 reveals that there is some CO desorption, while ramping between 300 to 325 K and 325 to 350 K. Indeed an increase in partial pressure of CO, well above the SS partial pressure, underscores the CO desorption from the SM-Pd surfaces. However, no such changes were observed above 350 K. An increase in CO_2 partial pressure

(well above the SS value), while increasing the temperature between 300 and 350 K (Fig. 5.1b) with 1:4 $CO:O_2$ composition hints CO poisoning on the SM-Pd is at least partially lifted. A decrease of 75-150 K for R_{max} and the activity broadening to lower temperature up to 300 K indicates a decrease in the activation energy by 20-30 KJ/mole. Based on the above experimental observations, we suggest the following: (1) the O-diffusion into the subsurfaces modifies the electronic nature of surfaces to be oxidized ($Pd^{\delta+}$ in PdO_x and $x \backsim 0.1$) in nature and the extent of δ should increase with θ_{O-sub}. This induces an electronic decoupling of the few Pd-layers with O-atoms from the rest of the bulk metallic Pd. (2) CO_{ads} on $Pd^{\delta+}$ is more reactive (rather than poisoning) due to the possibility of poor back donation of electrons from $Pd^{\delta+}$ and hence weakening of the CO bond strength [17]. This might be a possible reason for lifting of the CO poisoning at low temperatures on $Pd^{\delta+}$. (3) The mobility of CO is still high at ambient temperatures after the SM. Many catalytic reactions, such as CO oxidation, under practical conditions, are controlled by the coverage of one reactant. CO poisoning on noble metal surfaces is a well-known phenomenon below 400 K. However, CO adsorption and CO_2 production observed in the SS at 300 K, even with CO-rich compositions, fully demonstrates the SM lifted the inherent CO-poisoning problem to broaden the activity by allowing the oxygen adsorption on this surface. This highlights the importance of SM towards the altered activity by altering the adsorption science.

5.3.2 Near-Ambient Pressure Photoelectron Spectroscopy Studies

In situ spectroscopic investigations were carried out at NAP conditions using a lab-based APPES facility to verify the role of SM in enhancing the low temperature CO oxidation activity on Pd. In the APPES unit XPS and ultraviolet photoelectron spectra (UVPES) can be recorded up to 1 and 0.3 mbar pressure, respectively [18-19]. Before we go into the $CO+O_2$ reaction details on clean and SM-Pd surfaces, it is essential to understand the behavior of CO, O_2 and CO_2 independently in gas phase as well as on Pd-surfaces. Reference gas-phase spectra of CO, O_2 or CO_2 recorded at 0.1 mbar are shown in Fig. 5.6a; CO and CO_2 spectra recorded on Pd(111) and SM-Pd are also shown in Fig. 5.6b and 5.6c, respectively. Characteristic vibrational features of free or physisorbed gas molecules are observed [19-21].
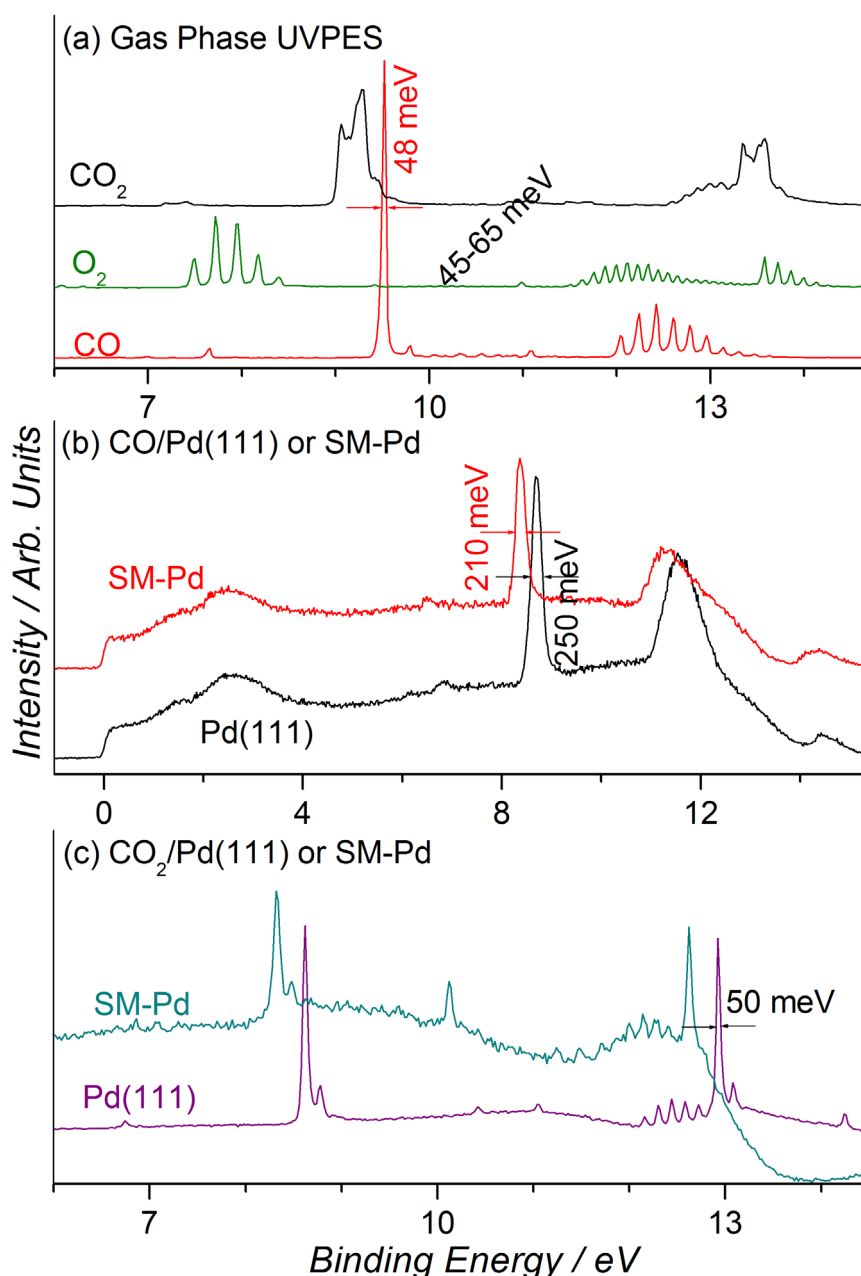
Figure 5.6: a) Gas phase UVPES features of CO, O_2, and CO_2 recorded at 0.1 mbar gas pressure. b) UVPES spectra of 0.1 mbar CO at 350 K on the clean Pd(111) and SM-Pd surfaces. c) UVPES spectra of 0.1 mbar CO_2 at 350 K on clean Pd(111) and on SM-Pd.

Importantly, vibrational features of all molecules shift to lower BE by 0.8-0.9 eV in the presence of clean Pd(111), compared to gas-phase, demonstrating the influence of surface potential in the binding energy (BE) values. Gas phase CO and O_2 (Fig. 5.6a), and CO_2 on Pd-surfaces (Fig. 5.6c) exhibits narrow vibrational features with a FWHM between 45 and 65 meV. It is surprising that gas-phase

CO_2 shows broad vibrational features (Fig. 5.6a), likely due to energy overlap of few vibrations. CO and CO_2 on SM-Pd shows the vibration feature at about same BE (8.35 eV). However, additional CO_2 vibration features are also observed distinctly at 12.6 eV, while CO shows a broad feature 11.3 eV; former CO_2 vibration features were employed to ascertain the CO_2 production, under reaction conditions.

Careful analysis of the vibration features of CO and CO_2 shows a shift in BE toward lower values on catalyst surfaces, compared to gas-phase. Among Pd-surfaces, SM-Pd exhibits lower BE than clean Pd(111) indicating the change in surface potential of 0.35 eV. Since there is no adsorbed CO_2, its features are sharp when it is close to catalyst surfaces; although many features are well resolved on catalyst surfaces, intensity also varied significantly. However, CO exhibits broad feature on catalyst surfaces, compared to gas-phase, indicating the presence of multiple sites in addition to gas-phase feature. Nonetheless, narrow width of 210 meV observed on SM-Pd at lower BE indicating the destabilisation of adsorbed CO molecules, due to surface modification.

O_2 interaction and $CO+O_2$ reaction was systematically measured with Pd(111) surfaces and the results are shown in Figure 5.7. Figure 5.7a shows the He I UVPES spectra of O_2/Pd(111) at various pressures and temperatures; due to low photon energy (hv = 21.2 eV), photoelectron escape depth is about 4-5 Å, and UVPES results truly reflects the surface changes. Typical high intensity Fermi level (E_F) and 4d doublet features of Pd was observed under all conditions [20]. At 10^{-5} mbar O_2 pressure and 650-900 K a new feature appears around 5.7 eV (dashed line), which broadens with increasing pressure. On O_2 introduction, in general, Pd 4d features broaden and begin to overlap; higher the oxygen pressure, more the overlap with a reduction in E_F intensity. This is mainly attributed to the donation of electron density from Pd to the oxygen present in the sub-surface layers to form Pd_xO_y layers. In addition, at 0.07 mbar the feature at 5.7 eV broadens to such an extent that a second feature is clearly visible at 6.5 eV (dotted line). Prolonged exposure time (150 min.) at 0.07 mbar pressure or increasing the pressure up to 0.3 mbar shows a single sharp peak at 6.5 eV, at the cost of the above broad features and E_F feature with reduced intensity. We assign the 6.5 eV peak to the growth of layers of surface PdO-like species, which is further confirmed by a distinct peak observed for PdO in Pd 3d core level XPS at 336.5 eV (see Fig.

5.8) [20]. When gas-phase oxygen is evacuated the above features (6.5 eV feature in Fig. 5.7a and 336.5 eV feature in Fig. 5.8) disappeared, while the peak at 5.8 eV reappeared. Apparently there is an equilibrium between PdO-like species and subsurface Pd_xO_y, and the latter is the precursor to the former [8,9] The feature at 5.7 eV does not disappear, even after CO titration at 550 K (after high pressure O_2 dosing); retainment of this feature rules out any possibility of surface oxide on the Pd(111) surfaces. The peak at 5.7 eV is stable up to 900 K and above which it decomposes due to oxygen desorption from subsurfaces [6,9,11]. We assign this peak at 5.7 eV to the O 2p features from subsurface Pd_xO_y. It is also fairly clear that PdO-like species decomposes, when the oxygen is removed indicating its metastable nature [6-11]. As UVPES is more surface sensitive due to low UV light penetration as well as very low kinetic energy electrons ($\leq$15 eV), the changes occurring in the top few atomic layers could be observed better.

CO oxidation reaction was carried out on SM-Pd. Figure 5.7b shows the He I UVPES spectra measured in situ with 2:1 $CO:O_2$ composition at 350 K (total pressure 0.1 mbar) on clean Pd(111) and on SM-Pd. The vibrational features of gas phase O_2 and CO appears at 6.4-7.4 eV and 8.35 eV, respectively, on SM-Pd (Figs. 5.6a and 5.7b). Critically, the gas phase CO_2 features were observed distinctly at 12.4-12.9 eV during the $CO+O_2$ reaction on SM-Pd (Fig. 5.7b). Reference gas-phase spectra of CO_2 shown in Fig. 5.6c very well corroborates the production of CO_2 during the reaction on the SM-Pd. Core level C 1s spectra recorded under same NAP reaction conditions exhibits the gas-phase CO_2 at 291 eV and adsorbed CO at 286 eV (Fig. 5.7b, inset); this observation fully confirms CO_2 production at 350 K and corroborates with UVPES results. Above APPES results demonstrates the CO oxidation on SM-Pd and in resonance with MBI results.
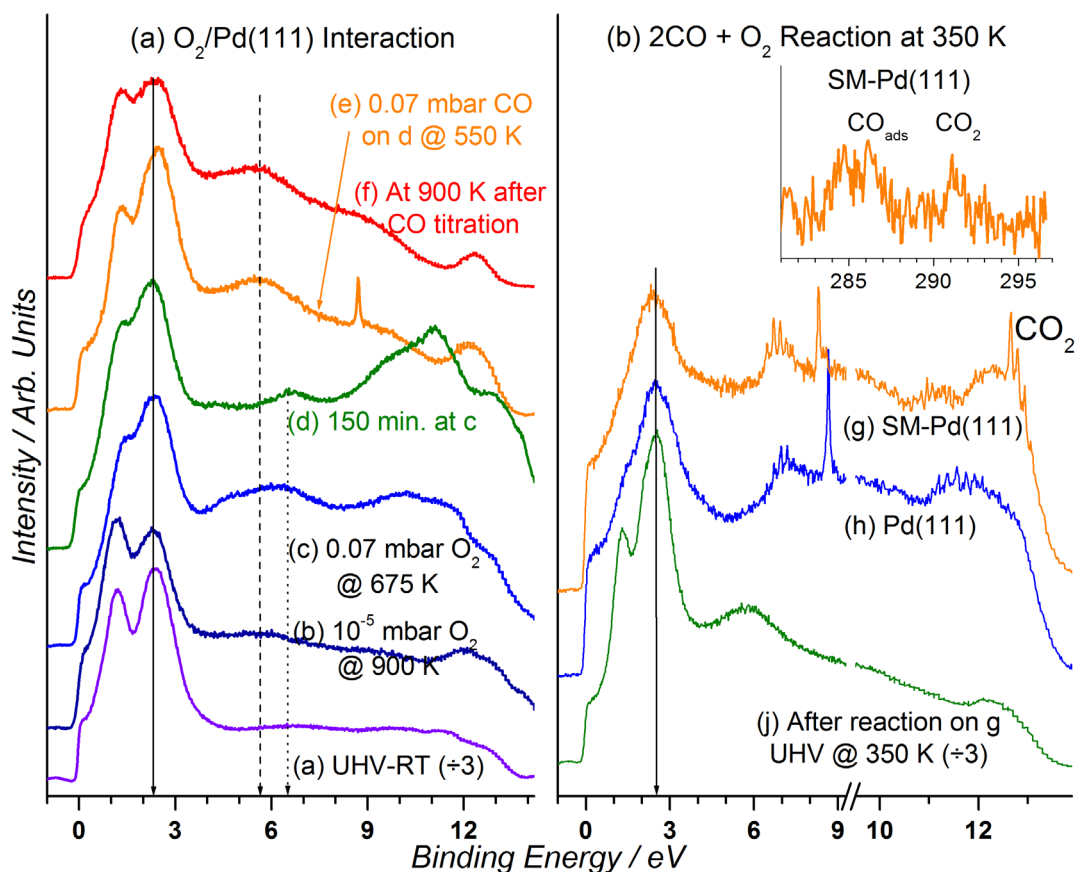
Figure 5.7 UVPES spectra recorded for (i) oxygen interaction with Pd(111) under different conditions and (ii) $CO+O_2$ reaction on clean and SM-Pd surfaces. (a) Clean Pd(111) at UHV and RT; (b) 10^{-5} mbar O_2 at 900 K; (c) At 0.07 mbar O_2 at 675 K; (d) After 150 min. at (c); (e) CO titration on d at 550 K and 0.07 mbar CO; (f) At 900 K after CO titration in e. (ii) CO + O_2 (2:1) reaction at 350 K on (g) SM-Pd, and on (h) clean Pd(111). (j) UVPES recorded at UHV and 350 K after the reaction shown in g and evacuation. *In situ* C 1s core level spectra is shown as inset; Gas phase CO_2 observed along with two CO_{ads} species.

Critically, the pressure under NAP conditions is about five - six orders of magnitude higher in APPES than MBI. Observation of CO_2 features directly in APPES under NAP reaction conditions also demonstrates an increase in turn over numbers by five orders of magnitude and it is the rate of supply of reactants that limits the reaction in the pressure regime studied. However, no CO_2 feature was observed on virgin Pd(111) surfaces under similar reaction conditions.
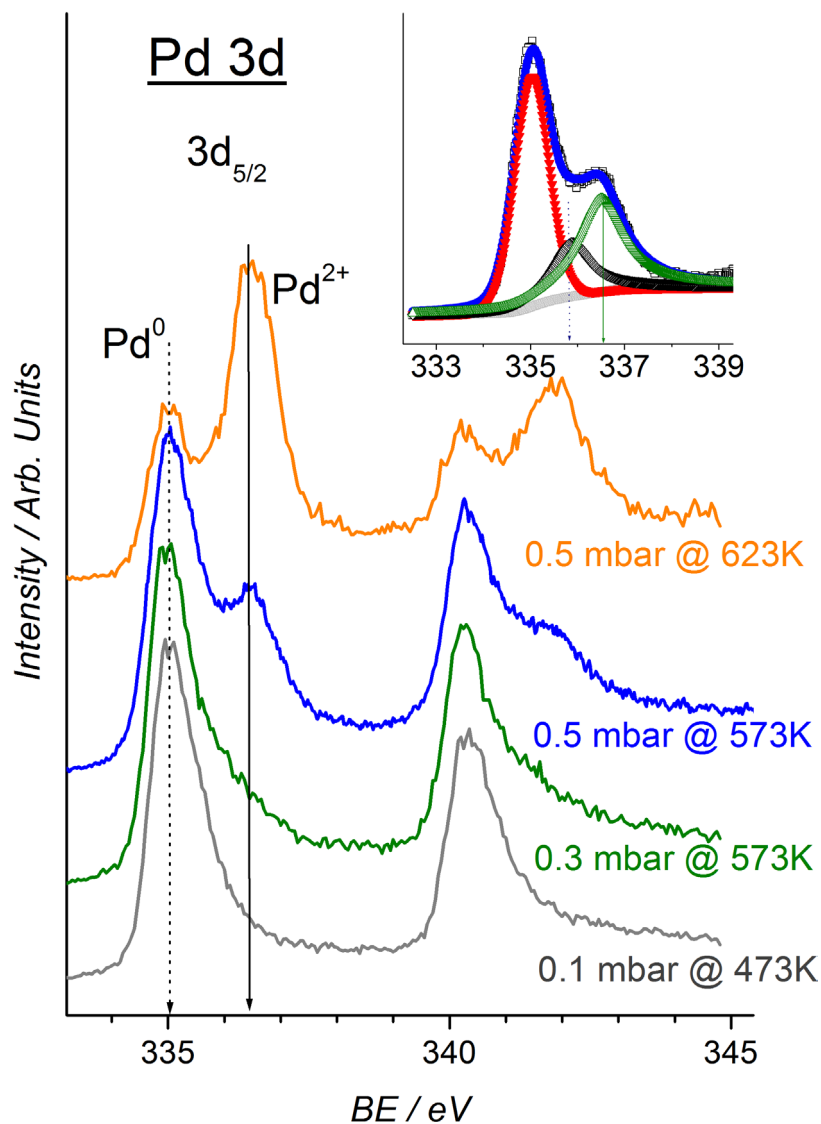
Figure 5.8. Representative Pd 3d core level spectra recorded at different temperatures and oxygen partial pressures. Asymmetrical broadening observed at higer BE side of Pd 3d core level features is due to diffusion of oxygen into subsurfaces followed by growth of PdO at 0.5 mbar and $\geq$573 K. When the oxygen supply was stopped, PdO feature diminishes rapidly; however the high BE asymmetric broadening is retained. This is in accordance with UVPES results. Deconvolution of Pd $3d_{5/2}$ spectrum recorded at 0.5 mbar at 573 K shows the presence of Pd^0 (red color) Pd^{2+} (green color) alongwith Pd_xO_y (black) species.

A careful comparison of the SM-Pd and clean Pd(111) spectra under NAP reaction conditions reveal the shift in BE of vibration features of CO and O_2 by 0.35 eV on the former, compared to the latter. This is attributed to the change in surface work function by 0.35 eV due to SM. Instead of typical Pd 4d doublet

bands, a single but broad VB feature was observed under reaction conditions is to be noted, which is attributed to the adsorbed CO (Fig. 5.7b). After evacuation of reactants, UVPES was recorded at UHV, and the results shows returning to the features of SM-Pd underscoring the non-consumption of oxygen in the subsurfaces. Fine vibrational features observed >11 eV in the gas-phase UVPES spectra of CO and O_2 could not be observed in the presence of Pd-surfaces (Figs. 5.6a and 5.7b); partially it could be the broadening due to the overlap of vibrational features from adsorbed and gas-phase species. However, CO_2 vibrational features were observed under the reaction conditions highlighting the non-interactive nature of CO_2 and Pd-surfaces.

§ 5.4 Conclusions

We do not want to generalize at this stage that the SM of Pd could broaden the reaction temperature regime for all catalytic reactions. However, we have demonstrated a method with high potential for many important reactions/ situations in catalysis. Indeed, Pd is known for C and H diffusion into sub-surfaces and forming carbides and hydrides, respectively [9, 11, 22]. O and H being opposite in nature/activity, such as oxidation and reduction, respectively, their presence in the subsurface of Pd (or any other noble metal, like Ru, Pt) would likely to broaden, or at least change, the reactivity. Common 'running in' approach employed in industrial catalysis, in which the catalyst is cycled through the reaction conditions several times before shifting the catalyst to the big plants for actual production, are due to stabilize the catalyst activity, may be partially due to the effect identified in this article [23]. Hence it is important to explore the above effect in a systematic manner under a variety of conditions and by different methods.

In fact, there are few reports indicating the surface palladium oxide being responsible for oxidation activity rather than the metallic Pd [24-27], whereas, Goodman et al claims the metallic Pd is active even under high pressure conditions [28]. Further, a small amount of Pd (typically ≤1 wt %) used in the automotive catalytic converters tend to be nanoparticles, enriched with defects, and hence O-diffusion into subsurfaces and surface oxidation of Pd is inevitable with net oxidizing exhaust composition in the present generation fuel-lean automobiles.

Hence there is no wonder why Pd is popular among noble metals for catalytic converters and increasingly employed by auto manufacturers. Further, there is no special preparation methods might be required to induce the surface modification on real world automotive catalysts, as they are inevitably subjected to oxygen rich and high temperature conditions, and fuel-rich and cold temperature conditions. Present work in combination with earlier reports [10,11,20,21] highlight that the modified Pd-surfaces holds promise for oxidation and reduction activity from ambient to 900 K. Nonetheless more work, especially measurements at atmospheric pressure, is required to fully understand the phenomenon so that Pd could be used suitably for many reactions after SM. By diffusing O, C or H atoms into the sub-surfaces (or a combination of two different atoms in the subsurfaces), complimentary reactions can be explored on different metal surfaces, especially noble metals. This opens up a new area of research in catalysis applications.

§ 5.5 References

[1]. M. Haruta, N. Yamada, T. Kobayashi, S. Iijima, *J. Catal.* **1989**, *115*, 301-309.

[2]. (a) A. Bottcher, H. Niehus, S. Schwegmann, H. Over, G. Ertl, *J. Phys. Chem. B* **1997**, *101*, 11185-11191. (b) M. Bowker, J. Counsell, K. El-Abiary, L. Gilbert, C. Morgan, S. Nagarajan, C. S. Gopinath, *J. Phys. Chem. C* **2010**, *114*, 5060-5067.

[3]. (a) D. Teschner, J. Borsodi, A. Wootsch, Z. Revay, M. Hävecker, A. Knop-Gericke, S. D. Jackson, R. Schlögl, *Science* **2008**, *320*, 86-89. (b) D. Teschner, Z. Révay, J. Borsodi, M. Hävecker, A. Knop-Gericke, R. Schlögl, D. Milroy, S.D. Jackson, D. Torres, P. Sautet, *Angew. Chem. Int. Ed.* **2008**, *47*, 9274-9277. (c) F. Viñes, C. Loschen, F. Illas, K. M. Neyman, *J. Catal.* **2009**, *266*, 59-63. (d) R. J. Behm, V. Penka, M. G. Cattania, K. Christmann, G. Ertl, *J. Chem. Phys.* **1983**, *78*, 7486-7490.

[4]. M. Armbrüster, M. Behrens, F. Cinquini, K. Fcttinger, Y. Grin, A. Haghofer, B. Klötzer, A. Knop-Gericke, H. Lorenz, A. Ota, S. Penner, J. Prinz, C. Rameshan, Z. Révay, D. Rosenthal, G. Rupprechter, P. Sautet, R. Schlögl, L. Shao, L. Szentmiklósi, D. Teschner, D. Torres, R. Wagner, R. Widmer,

G. Wowsnick, *ChemCatChem* **2012**, *4*, 1048-1063; and references therein.

[5]. G. Ketteler, D. F. Ogletree, H. Bluhm, H. Liu, E. L. D. Hebenstreit, M. Salmeron, *J. Am. Chem. Soc.* **2005**, *127*, 18269-18273.

[6]. (a) A. von Örtzen, A. S. Mikhailov, H. H. Rotermund, G. Ertl, *J. Phys. Chem. B* **1998**, *102*, 4966-4981. (b) F. P. Leisenberger, G. Koller, M. Sock, S. Surnev, M. G. Ramsey, F. P. Netzer, B. Klötzer, K. Hayek, *Surf. Sci.* **2000**, *445*, 380-393.

[7]. (a) D. Teschner, A. Pestryakov, E. Kleimenov, M. Haevecker, H. Bluhm, H. Sauer, A. Knop-Gericke, R. Schlögl, *J. Catal.* **2005**, *230*, 186-194. (b) T. Schalow, B. Brandt, D. E. Starr, M. Laurin, S. K. Shaikutdinov, S. Schauermann, J. Libuda, J-J. Freund, *Angew. Chem. Int. Ed.* **2006**, *45*, 3693-3697. (c) Y. N. Sun, Z. H. Qin, M. Lewandowski, S. Kaya, S. Shaikutdinov, H-J. Freund, *Catal. Lett.* **2008**, *126*, 31-35. (d) Y. N. Sun, Z. H. Qin, M. Lewandowski, E. Carrasco, M. Sterrer, S. Shaikutdinov, H-J. Freund, *J. Catal.* **2009**, *266*, 359-368.

[8]. E. Lundgren et al. *Phys. Rev. Lett.* **2004**, *92*, 046101.

[9]. H. H. Kan, R. B. Shumbera, J. F. Weaver, *Surf. Sci.* **2008**, *602*, 1337–1346.

[10]. (a) M. Chen, X. V. Wang, L. Zhang, Z. Tang, H. Wan, *Langmuir* **2010**, *26*, 18113-18118. (b) A. Markovits, C. Minot, *Chem. Phys. Lett.*, 2008, *458*, 92-95. (c) S. Nagarajan, C. S. Gopinath, *J. Indian Inst. Sci.* **2010**, *90*, 245-260.

[11]. (a) C. S. Gopinath, K. Thirunavukkarasu, S. Nagarajan, *Chem. Asian J.* **2009**, *4*, 74-80. (b) S. Nagarajan, K. Thirunavukkarasu, C. S. Gopinath, *J. Phys. Chem. C* **2009**, *113*, 7385-7397.

[12]. (a) K. Thirunavukkarasu, K. Thirumoorthy, J. Libuda, C. S. Gopinath, *J. Phys. Chem. B* **2005**, *109*, 13283-13290. (b) S. Nagarajan, K. Thirunavukkarasu, C. S. Gopinath, *J. Phys. Chem. C* **2011**, *115*, 21299-21310.

[13]. (a) K. Thirunavukkarasu, C. S. Gopinath, *Catal. Lett.* **2007**, *119*, 50-58. (b) S. Nagarajan, K. Thirunavukkarasu, C. S. Gopinath, J. Counsell, L. Gilbert, M. Bowker, *J. Phys. Chem. C* **2009**, *113*, 9814-9819.

[14]. T. Engel, G. Ertl, *J. Chem. Phys.* **1978**, *69*, 1267-1281.

[15]. I. Z. Jones, R. A. Bennett, M. Bowker, *Surf. Sci.* **1999**, *439*, 235-248.

[16]. R. Imbihl, G. Ertl, *Chem. Rev.* **1995**, *95*, 697-733.

[17]. V. V. Kaichev, V. I. Bukhtiyarov, G. Rupprechter, H. J. Freund, *Kinet. Catal.* **2005**, *46*, 269-281.

[18]. K. Roy, C. P. Vinod, C. S. Gopinath, *J. Phys. Chem. C* **2013**, *117*, 4717-4726.

[19]. K. Roy, C. S. Gopinath, *Anal. Chem.* **2014**, *86*, 3683-3687.

[20]. (a) K. Roy, C. S. Gopinath, *ChemCatChem* **2014**, *6*, 531-537. (b) K. Roy, R. Jain, C. S. Gopinath, *ACS Catal.* **2014**, *4*, 1801-1811.

[21]. F. Viñes, A. Borodin, O. Hfft, V. Kempter, F. Illas, , *Phys. Chem. Chem. Phys.* **2005**, *7*, 3866-3873.

[22]. Y. F. Han, D. Kumar, C. Sivadinarayana, A. Clearfield, D. W. Goodman, *Catal. Lett.* **2004**, *9*, 131-134.

[23]. G. Ertl, *Angew. Chem. Int. Ed.* **2008**, *47*, 3524-3535.

[24]. G. Corro, O. Vázquez-Cuchillo, F. Banuelos, J. L. G. Fierro, M. Azomoza, *Catal. Commun.* **2007**, *8*, 1977-1980.

[25]. R. Burch, F. J. Urbano, *Appl. Catal., A: Gen.* **1995**, *124*, 121-138.

[26]. (a) S. Roy, M. S. Hegde, N. Ravishankar, G. Madras, *J. Phys. Chem. C* **2007**, *111*, 8153-8160. (b) E. M. C. Alayon, J. Singh, M. Nachtegaal, M. Harfouche, J. A. van Bokhoven, *J. Catal.* **2009**, *263*, 228-238.

[27]. R. v. Rijn, O. Balmes, R. Felici, J. Gustafson, D. Wermeille, R. Westerstrm, E. Lundgren, J. W. M. Frenken, *J. Phys. Chem. C* **2010**, *114*, 6875-6876.

[28]. F. Gao, Y. Wang, Y. Cai, D. W. Goodman, *J. Phys. Chem. C* **2009**, *113*, 174-181.

Conclusions and Future Outlook

Conclusions

In this dissertation, the operando studies on gas-solid interactions have been emphasized. Compared to interactions in homogeneous liquid phase reactions, the heterogeneous gas-solid reactions are more complex in nature. The interrelation between the reactivity and the structure of a solid catalyst is not straightforward, and many parameters in different length scales and time scales may contribute to the overall activity. Therefore, the study of heterogeneous gas-solid catalytic reactions has always been difficult, and many surface science techniques have contributed for the same. Here, two very important surface science techniques, namely MBI and APPES have been employed to investigate heterogeneous catalytic reactions (H_2-SCR, CO oxidation) on palladium. MBI is a well-known technique for understanding kinetics of the elementary processes in gas-solid interactions. It gives wealth of quantitative information too. However, MBI bridges the pressure gap between conventional surface science conditions and practical catalysis to an intermediate level. Generally, it works in the pressure range of 10^{-4} to 10^{-6} mbar. APPES is comparatively new and a rapidly developing cutting-edge technique.

This technique can be operated successfully in elevated pressures, and requires very sophisticated electron analyzer and differential pumping in the detector side, as well as high brilliance of photons in a focused spot in the source side. Last decade has seen commissioning of many APPES systems in the synchrotron beamlines all over the world. In fact, the availability of new generation synchrotron sources has helped in APPES research and development. Not only to the synchrotron, has the APPES also been established in few research laboratories with conventional photon sources, such as monochromatic X-ray source, twin-anode X-ray souce, and helium discharge lamp sources [1-3].

The design and critical features of a laboratory based custom-built APPES system has been described here (*see* Chapter 2). It can successfully analyze XPS at 1 mbar pressure on the sample surface with a 0.8 mm aperture cone. The double front cone pumping and aperture free lens regime in the ELR increases the collection of photoelectrons, and thus a good intensity with a good S/N ratio can be achieved. A set of results showing the various stages of oxidation of coinage metals (Au, Ag, and Cu) in presence of 1 mbar oxygen and in different temperatures, has been described to demonstrate the capabilities and performance of the spectrometer.

The lab-APPES, also, successfully performs valence band photoemission up

THESIS KANAK

to 0.3 mbar. This is the first report of UVPES at such high pressure. The design of the source helps in its performance and analyzer design facilitates detection of photoelectrons in high pressure. The key performance of the lab-APPES is photoelectron detection both in low KE energy regimes as well as high KE energy regimes. A set of convincing results showing the detailed valence band changes in complete oxidation of Cu to CuO has been described in Chapter 3 to demonstrate the capability of this technique to understand surface electronic changes of a material surface during a reaction. Through observation of low KE electrons at NAP and at high temperatures, the possibility of following valence band electronic structure under near working conditions of catalysts and materials is established.

In Chapter 4 and 5, a possible way has been suggested to tune the catalytic activity of palladium without much modification in its chemical properties. Palladium is a very important active particle in hydrogenation reactions, and TWC reactions. The dissoluting nature of palladium often leads to the formation of surface, subsurface, and bulk oxide /carbide/ hydride, however depending on the reaction temperature and pressure. We have shown that the presence of subsurface O in palladium changes its catalytic activity in $NO + H_2 + O_2$ and CO oxidation reactions. The reaction temperature shifts to the lower regime significantly. An important aspect of the present work to be underscored is the permanence of oxygen atoms diffused into the subsurfaces. As long as the temperature does not increase above 1000 K, the above feature is stable and exhibits its influence in demonstrating near-ambient temperature $deNO_x$ and CO oxidation catalytic activity. Further, surface oxide that forms under oxygen-rich conditions either decomposes or the oxygen in the surface oxide is consumed under fuel-rich or reductive conditions. This exposes the modified surfaces, and hence, the low temperature activity reverts.

Future Outlook

We do not generalize the influence of subsurface oxygen on palladium for all reactions on palladium. Other imporant oxidation and reduction reactions on modified Pd should be studied further. This aspect could also be explored for other metals, like Ru, Pt, Re. Not only the surface science studies, the activity of subsurface modified Pd should be tested under real world practical conditions and on supported powder catalysts.

Another aspect toward which the work can be extended is the study of Pd based supported catalysts. The real world catalysts are active metal particles supported and distributed on oxidic support. By studying reactions on

polycrystalline Pd foils and on single crystals, we may understand the role of active metals. But a more realistic study will be to understand both the active particles and metal-support interactions. However, studying more complex materials would require careful consideration. Obtaining good intensity and good S/N ratio for dispersed and diluted samples may become an obstacle for their investigation by Lab-APPES. However, more research is required on improving the design features of APPES to work with powder based catalysts or with dilute active metal based catalytic materials.

References

[1.]^ D. E. Starr, H. Bluhm, Z. Liu, A. Knöp-Gericke, M. Hävecker, *John Wiley & Sons, Inc.* **2013**, pp. 315-343, and references therein.

[2.]^ A. Shavorskiy, H. Bluhm, *Wiley-VCH Verlag GmbH & Co. KGaA* **2014**, pp. 437-468, and references therein.

[3.]^ S. K. Eriksson, M. Hahlin, J. M. Kahk, I. J. Villar-Garcia, M. J. Webb, H. Grennberg, R. Yakimova, H. Rensmo, K. Edström, A. Hagfeldt, H. Siegbahn, M. O. M. Edwards, P. G. Karlsson, K. Backlund, J. Åhlund, D. J. Payne, *Rev. Sci. Instrum.* **2014**, 85, 075119/075111-075119/075111, and references therein.

Appendix

About the Author

Kanak, son of Late Hitendra Nath Roy and Smt. Rekha Roy, was born at Dakshin Paniyalguri, Alipurduar, West Bengal in 1985. His schooling was in Dakshin Paniyalguri Primary School, Union Academy Kalchini, and then Ramakrishna Mission Vidyamandir, Belurmath. He received a B.Sc. in Chemistry honours from Ramakrishna Mission Residential College, Narendrapur (affiliated to University of Calcutta) and a M.Sc.in Chemistry from Indian Institute of Technology Kharagpur. He joined CSIR – National Chemical Laboratory, Pune as a Junior Research Fellow (CSIR) in July, 2009 to pursue his Doctoral studies under the guidance of Dr. Chinnakonda S. Gopinath. He received NCL Research Foundation Keerti Sangoram Award for "Best Research Scholar" in catalysis for the year 2014.